MONITORING THE INTERNAL STRAINS IN CFRP LAMINATES FROM PROCESSING TO MACHINING AND TEMPERATURE CYCLING

by

BASO NASRULLAH

A thesis submitted in fulfillment of the requirements
for the degree of
Doctor of Engineering
in Graduate School of Science and Engineering
Ehime University

December 2020

SUMMARY

This study aims at investigating the internal strain of Carbon Fiber Reinforced (CFRP) laminate from processing to machining and the thermal expansion coefficient of fiber metal laminate FML) during temperature cycling. CFRP and CFRP-Metal laminate are widely used in aerospace, automotive, wind energy, and machinery construction application due to their high stiffness and high strength to weight ratio. For example, using CFRP instead of metals in automobile vehicles is reported to bring a weight reduction factor, significantly improving fuel efficiency, maneuverability, and payload capacity of the vehicles. Compared with traditional materials (e.g., metals), carbon fibers have greater fatigue resistance, better long-term stability, lower thermal expansion, and excellent corrosion resistance. Such advantages make CFRP a potential candidate for a wide range of applications in various and extreme environmental conditions.

Nonetheless, in any fabrication method of composite, unexpected deformation such as geometrical distortion due to residual stress/strain must be minimized to assure the dimensional accuracy and structural integrity of the component. Generally, the internal stresses or strains in composite materials were driven by composite intrinsic properties, processing, and environmental condition. The presence of internal residual stress/strain due to processing and machining may cause difficulties in assembly or degradation of in-service of composite component or structure. It has been reported that a lot of factors such as chemical (cure) shrinkage, thermal shrinkage, and viscoelastic properties affect the residual stress/strain level during and after a cure process. In the machining-process, the transient and permanent residual strain appear due to cutting force, temperature, and machining-induced damage. Therefore, it is essential to clarify the internal strain state after fabrication (processing and machining) to assure their dimensional stability and structural integrity.

Recently, various methods have been developed to measure the residual strain and thermal strains in composite materials. The strain measurement methods are generally classified into two categories: (i) point-by-point measurement and (ii) full-filed measurement. The electric resistance strain gauge measurement is the most common among the first category. The strain gauge can not only be bonded to the surface of the specimen but also embedded in the specimen. Another point-by-point method is Raman microspectroscopy, by which the stress or strain is estimated from the peak shift of Raman scattering (Raman shift) with the change in the vibration energy of molecules. The next method in this category is measurement using fiber optic sensors such as extrinsic Fabry-Perrot interferometry (EFPI) sensors and Fiber Bragg Grating (FBG) sensors. EFPI sensors are immune to ambient temperature conditions. A disadvantage of EFPI is the relatively large diameter that leads to perturbation of the strain around the embedded sensors. In contrast, FBG sensors with smaller diameters are more appropriate for embedding in composite laminate, although they need

temperature compensation when subjected to thermal load. Moiré interferometry, digital image correlation (DIC), and speckle interferometry are classified into the full-field measurement category. The above three methods have the advantage of non-contact full-field measurement, generally coupled with image processing. However, it is difficult to precisely obtain small thermal strains of a laminate heated in a thermostatic chamber or an autoclave because the light does not directly reach the target to be measured. Furthermore, thermomechanical analysis (TMA) is commonly used to measure the CTE of a composite. Careful sample preparation is crucial for accurate TMA measurement of near-zero CTE with an absolute value less than 1x10-6/°C. For the above reasons, the FBG sensors are the most suitable for the measurement of internal strain particularly small thermal strains, as long as the appropriate temperature compensation is performed.

The material used is a carbon/epoxy prepreg (T700S/2592) to produce cross-ply and quasi-isotropic laminate utilizing an autoclave. FBG sensors were embedded in the laminate to monitor the entire curing process and machining. The strain at the gel point when the laminate starts to vitrify was defined as zero strain in both processing and drilling. Then, the residual strain was calculated from the wavelength shift recorded by the optical sensing interrogator and the temperature change. By using the same specimen and sensor (FBG and Thermocouple), hole machining was conducted near the FBG sensors and thermocouple. The temperature and peak wavelength shift recorded by the data logger and optical interrogator used to calculate the internal strain and strain change during drilling. Various machining conditions were applied to create a specific damage/delamination size. The reflection spectrum is also considered to assure the reliability of strain measurement data. The exact location of the FBG sensor and the size of delamination caused by drilling was then quantitatively measured using soft X-ray radiography. Finally, the specimen was cut in the cross-section to observe the sensor condition after drilling.

In addition, a pitch-based CFRP and Stainless Steel (SST) laminate is employed to develop Fiber Metal Laminate (FML) with a near-zero coefficient of thermal expansion. Base on the lamination theory, Young's modulus and CTE of the FML were obtained to confirm the quasi-isotropy of the elastic modulus and thermal expansion. The thickness ratio between SST and CFRP was determined to achieve an exact zero-CTE at room temperature (25°C). The density of the zero-CTE FML was also calculated with the aid of the rule of mixture. The thermal strain of the UD-CFRP, QI-CFRP, and FML was measured using an embedded Fiber Grating (FBG) sensor during a heating or cooling cycle. Then, the CTEs of the CFRPs and FML were obtained to investigate the temperature dependence of the CTEs of the materials and verify the zero-CTE of the FML in the vicinity of room temperature. The last, Finite Element Analysis (FEA) was conducted taking the temperature dependence of the CTEs and elastic moduli of the CFRP into account to compare the CTE of the FML between the experimental lamination theory and FEA result.

The absolute internal strain was consistently monitored through processing (curing) to machining (drilling) by defining the strain at the gel point to zero. As a result, the drilling-induced strain is separated from the process-induced strain. This seamless monitoring makes it possible to distinguish between the process-induced strain and machining-induced strain, and it is impossible to know the sign (tensile or compressive) of the internal strain until the seamless strain monitoring is conducted, just like in this study. It was found that the internal strain detected by the FBG sensor was correlated with not only damage size or a delamination factor but also its relative position and total internal strain.

It is found from the experiment results that the CTE of a fabricated FML was accurately measured using embedded fiber Bragg grating (FBG) sensors to verify that the CTE had a near-zero value around room temperature. The temperature dependence of the FML CTE from 20 to 120°C was investigated via finite element analysis (FEA), taking the temperature-dependent material properties into account. It was demonstrated from the experiment and FEA that the present FML had a near-zero CTE around room temperature (20-40°C) and higher Young's modulus and specific modulus compared with other relevant materials.

In conclusion, the seamless internal strain and strain change during the whole processing and machining was successfully monitored using an embedded FBG sensor and thermocouple. It is found that, the internal strain and drilling-induced strain are correlated with the relative FBG sensor position and the delamination factor, which is never reported in any references. Furthermore, the accurate measurement of near-zero CTE has been clarified using embedded FBG sensors. The FML laminate has a high specific modulus compared with other competing materials and conventional FMLs even though quasi-isotropy and zero CTE are maintained simultaneously.

TABLE OF CONTENT

SUMMARY i

TABLE OF CONTENT iv

LIST OF FIGURES vii

LIST OF TABLES xi

LIST OF SYMBOLS AND ABBREVIATIONS xii

CHAPTER 1: INTRODUCTION 1

1.1. General Background 1

1.2. Literature Review 6

1.3. Research Objectives 11

1.4. Thesis Outline 11

CHAPTER 2: THEORETICAL BACKGROUND 13

2.1. Fiber Bragg Grating (FBG) Sensor 13

2.1.1. Principle of FBG sensor 13

2.1.2. Strain and Temperature Sensitivity 14

2.2. Laminate Theory and CTE 17

2.2.1. Generalized Hooke's Law For Nonisotropic Materials 17

2.2.2. Stress and Strain, Plane Stress for Specially Orthotropic Plate 18

2.2.3. Stress and Strain, Plane Stress for Generally Orthotropic Plates 20

2.2.4. Laminate Theory 22

2.2.5. Thermal Expansion of Laminate 27

CHAPTER 3. SEAMLESS MONITORING OF INTERNAL STRAIN DURING PROCESSING AND DRILLING IN A CFRP LAMINATE 29

3.1 Experimental Procedure 29

3.1.1 Material and sensors 29

3.1.2 Cure-process monitoring 31

3.1.3 Drilling monitoring 32
3.2. Result and Discussion 35
3.2.1 Process-Induced Strain of cross-ply laminates 35
3.2.2 Process-Induced Strain of quasi-isotropic laminates 38
3.2.2 Drilling-Induced Strain 40
3.2.3 Wavelength spectrum during and after drilling. 47
3.2.4 Drilling-Induced Damage 49
3.3. Conclusions 54
CHAPTER 4. IN-SITU MONITORING OF CFRP-METAL LAMINATE WITH LOW THERMAL EXPANSION 55
4.1. Design of the CTE based on lamination theory 55
4.1.1. Theory. 55
4.1.2. Calculation of CTE and Young's modulus. 57
4.2. Experimental Procedure 60
4.2.1. CTE measurement using FBG sensors 60
4.3. Finite element analysis 66
4.4. Result and Discussion 67
4.4.1. Experiment result 67
4.4.2. FEA result 73
4.5. Conclusions 76
CHAPTER 5. CONCLUSIONS AND FUTURE WORK 77
5.1. General Conclusions 77
5.2. Future Work 78
REFERENCES 79
ACKNOWLEDGMENTS 87

LIST OF FIGURES

Figure 1- 1 The chart for specific stiffness and strength [8] 2

Figure 1- 2 Composite applications. 3

Figure 1- 3 Composite Aerospace applications development in the last 40 years [17]..... 3

Figure 1- 4 Focus of the present study in the field of CFRP manufacturing. 10

Figure 1- 5 Thesis Outline 12

Figure 2- 1 Basic principle of FBG sensor 14

Figure 2- 2 Difference between an isotropic and an orthotropic plate. 18

Figure 2- 3 Generally orthotropic lamina 21

Figure 2- 4 Notation for laminate coordinate within a laminae 22

Figure 2- 5 Bending Geometry in the x-z plane. 23

Figure 3- 1 Location of an FBG sensor and a thermocouple in (a) CFRP cross-ply laminate and (b) quasi-isotropic laminate. 31

Figure 3- 2 Cure-process monitoring using an FBG sensor. 32

Figure 3- 3 Experimental setup for real-time strain monitoring during drilling. 33

Figure 3- 4 The instrument of X-Ray radiography and x-ray experiment result sample. 34

Figure 3- 5 Delamination size and location of the FBG sensor around a hole. 35

Figure 3- 6 The internal strain and temperature of a CFRP cross-ply laminate during processing. 36

Figure 3- 7 The internal strain and temperature of a CFRP quasi-isotropic laminate during processing. 38

Figure 3- 8 (a) Internal strain and (b) temperature change during drilling of a cross-ply laminate. 42
Figure 3- 9 (a) Internal strain and (b) temperature change during drilling of a quasi-isotropic laminate. 43
Figure 3- 10 Relation between the relative position of the FBG sensor and internal strain and strain change after cross-ply laminate drilling..... 46
Figure 3- 11 Relation between the relative position of the FBG sensor and internal strain and strain change after quasi-isotropic laminate drilling..... 46
Figure 3- 12 Wavelength spectrum during drilling of cross-ply laminate (a) condition-1 (b) condition-5..... 48
Figure 3- 13 Wavelength spectrum during drilling of quasi-isotropic laminate (a) condition-1 (b) condition-5..... 49
Figure 3- 14 Internal strain and strain change against delamination factor of cross-ply laminate. 50
Figure 3- 15 Internal strain and strain change against delamination factor of quasi-isotropic laminate. 51
Figure 3- 16 Quasi-isotropic laminate cross-section of drilled hole wall with (a) small damage and (b) large damage/delamination (c) FBG section gage..... 52
Figure 3- 17 Cross-ply laminate cross-section of FBG sensor at a quasi-isotropic laminate cross-section of drilled hole wall with (a) small damage and (b) extensive damage/delamination (c) FBG section gage..... 53

Figure 4- 1 CTE and Young's modulus of the FML. 59
Figure 4- 2 Density and specific modulus of the FML 59
Figure 4- 3 Specific modulus vs. CTE of competing materials in Table 3-1. 60
Figure 4- 4 Temperature and pressure condition in the (a) fabrication process and (b) heating/cooling cycle. 62
Figure 4- 5 Locations of FBG sensors and thermocouples embedded in the UD-CFRP, QI-CFRP, and FML. 62
Figure 4- 6 Experimental setup for fabrication and CTE monitoring during a heating/cooling cycle using an autoclave. 63
Figure 4- 7 Photograph showing (a) appearance of the FML (250 mm square), (b) embedding of the FBG sensor, and (c) the interface between the SST foil and CFRP plies. 65
Figure 4- 8 Schematic illustration showing (a) dimensions, (b) boundary conditions for analysis of thermal expansion, and (c) boundary conditions for analysis of Young's modulus in the finite element analysis. 67
Figure 4- 9 Measured CTE of UD-CFRP and QI-CFRP laminates. 68
Figure 4- 10 Temperature dependence of the CTE of the QI-CFRP laminate. 69
Figure 4- 11 Temperature dependence of normalized elastic moduli of UD-CFRP [23]. ... 70
Figure 4- 12 Thermal strain-temperature diagrams for the two FBG sensors embedded in the FML. 71
Figure 4- 13 CTE-temperature diagrams for the two FBG sensors embedded in the FML. 72
Figure 4- 14 Calculated thermal strain distributions εx and εy on the top surface (SST) of the FML. The CTEs and elastic moduli are temperature-dependent (Case III). 74

Figure 4- 15 FEA results of the thermal strain vs. temperature of the FML. Cases I, II, and III represent the calculated CTE, assuming that (I) CTEs and elastic modulus are constant, (II) CTEs are temperature dependent, and (III) CTEs and elastic modulus are temperature-dependent. 74

Figure 4- 16 Comparison of the temperature dependence between the measured and calculated CTE of the FML. 75

LIST OF TABLES

Table 4- 1 Comparison of CTE, Young's modulus, shear modulus, and specific modulus among relevant competing materials at room temperature. The values in the literature [19] are referred for GLARE, CARAL, and Ti/Gr. 58

Table 4- 2 Values in equation (66) 63

Table 4- 3 CTE and Young's modulus of the FML at RT 75

LIST OF SYMBOLS AND ABBREVIATIONS

A	1st quadrant of laminate stiffness matrix, 3x3
α	Experimentally measured CTE
α_δ	Change of the refraction index, α_δ = 5...8*10-6/K
α_{sp}	Expansion coefficient per K of specimen
CFRP	Carbon Fiber Reinforced Plastic/Polymer
CS	Wavelength–strain sensitivity
CT	Wavelength–temperature sensitivity.
CTE_x	Coefficient of thermal expansion in the x-direction
CTE_y	Coefficient of thermal expansion in the y-direction
DIC	Digital Image correlation
D_{max}	Maximum diameter of delamination
D_{nom}	Nominal hole diameter
ΔT	Temperature change
$\Delta\lambda$	Wavelength shift
E1	Lamina elastic modulus in fiber direction
E2	Lamina elastic modulus in transverse direction
EFPI	Extrinsic Fabry-Perot interferometry
ε	Strain
ε_m	Mechanically caused strain
ε_T	Temperature caused strain
ε_x	Strain in the x-direction
ε_y	Strain in the y-direction
Fd	Delamination factor
FEA	Finite element analysis
FML	Fiber metal laminate
G_{12}	Lamina shear modulus
h	Thickness of laminate

k	Ply number index
k	Gage factor, k = 0.78
Λ	Grating period of the FBG
λ_B	Bragg wavelength,
λ_0	Base wavelength
n	Effective refractive index of the FBG
p	Photo elastic coefficient, p = 0.22
PAN	polyacrylonitrile
Q	Ply stiffness matrix
SST	Stainless Steel
T	Temperature
t	Ply thickness
τ	Transformation matrix, 3x3
TMA	Thermomechanical analysis
UD	Uni-directional
v_{12}	Lamina Poisson's ratio
x-y	Coordinate system aligned with laminate 0º (x) and 90º (y) directions
1-2	Coordinate system aligned with lamina fiber (1) and transverse (2) directions

CHAPTER 1: INTRODUCTION

1.1. General Background

A composite material is a material made from two or more constituent materials with different physical or chemical properties significantly that, when combined, produce a material with new characteristics different from the individual constituent materials. The individual components remain separate and distinct within the finished structure, differentiating composites from mixtures and solid solutions. In general, fiber composite materials have two constituent elements; reinforcement fibers and a matrix. The matrix in a composite material act to transfer the load to the reinforcement fibers, provide temperature resistance and chemical resistance, and maintain the reinforcement fibers in a fixed orientation. The second constituent of composite material is the reinforcement fiber [1, 2]. The tensile properties, stiffness, and impact resistance of composite materials are influenced by the type of fiber reinforcement[3, 4].

In Carbon Fiber Reinforced Plastic/Polymer (CFRP), the reinforcement is carbon fiber, which provides the strength. Carbon fiber is made from organic polymers, which consist of long strings of molecules held together by carbon atoms. Most carbon fibers (about 90%) are made from the polyacrylonitrile (PAN) process. A small amount (about 10%) are manufactured from rayon or the petroleum pitch process (Pitch-Based)[5]. It is realized that the mechanical properties of a composite material depend on the matrix and the reinforcement materials used to manufacture the composite [6,7]. Unlike isotropic materials like steel and aluminum, CFRP has directional strength properties. The properties of CFRP depend on the layouts of the carbon fiber and the proportion of the carbon fibers relative to the polymer.

CFRP laminates have a diverse laminated structure, consisting of individual layers of high-modulus, high-strength carbon fibers in a thermoplastic or thermoset matrix. The individual layers that compile the laminates are known as laminae or plies and are generally orthotropic or transversely isotropic, with the laminate then exhibiting anisotropic, orthotropic or quasi-isotropic behavior depending on its stacking sequence. Composites and more specifically, CFRP lie close to the top left corner of both charts: they have a high specific stiffness and a high specific strength, as can be seen in the Ashby [8] plots of Figure 1-1. This interesting combination of stiffness, strength and low mass has allowed CFRP materials to experience significant growth and increased market demand in various industrial fields such as aviation and aerospace [9,10], automotive [11]–[13], wind energy [14], construction[15] and machinery [16] as shown in Figures 1-2 and 1-3.

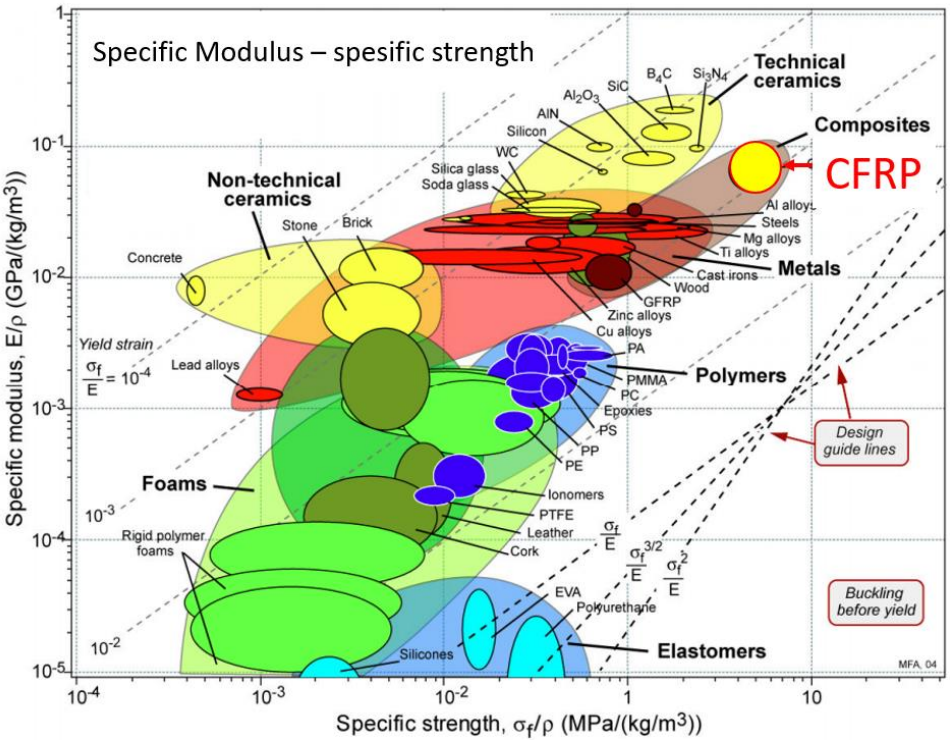

Figure 1- 1 The chart for specific stiffness and strength [8]

Figure 1- 2 Composite applications.

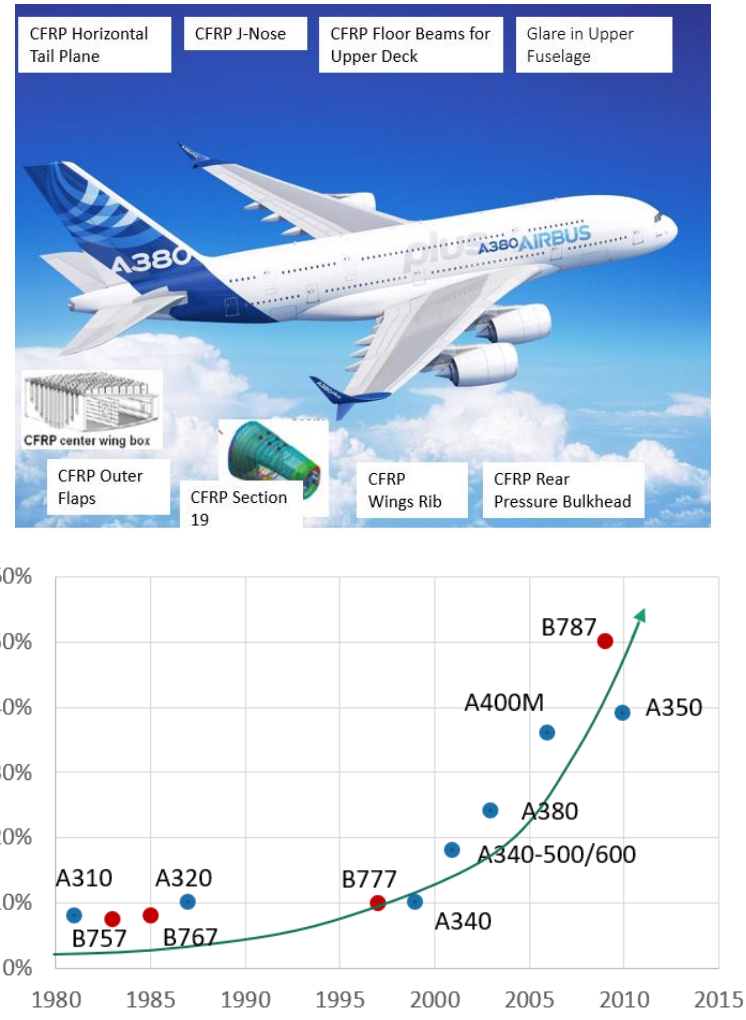

Figure 1- 3 Composite Aerospace applications development in the last 40 years [17].

They have become increasingly popular in almost every field associated with high performance. Their popularity is due to the fact that when compared to many other engineering materials, they offer superior stiffness, strength, and fatigue properties at relatively low density. They also have stable tensile strength, excellent corrosion resistance and dimensional stability. For example, there are several advantages of using them over aluminum and titanium alloys: Reduction in the number of components and fasteners, which bring about the decrease of manufacturing and assembly costs. For instance, using CFRP instead of metals in automobile vehicles is reported to bring a weight reduction factor, significantly improving fuel efficiency, maneuverability, and payload capacity of the vehicles.

Recently, applications of composite parts have become more and more interesting and relevant also in general machine construction and especially in the machine tool sector. Whereas for a long time, CFRP and other composite materials have been used predominantly in scientific works and prototypes of machine tool structural elements, elements, tool components, and spindles, nowadays, a rising number of industrial implementations can be found [16].

The lightweight CFRP construction potentials provide new possibilities to reduce moved masses (e.g. of slides, columns, rams), to lower inertia moments (e.g. of spindle or tool shafts), to relieve the drive systems of the machines, to enhance the feed motion dynamics and path accuracy, and to improve the energy efficiency of the machine tools during machining operations. Furthermore, due to the higher material damping properties of composite materials, increased structural damping ratios can be achieved. In addition, the very low or even negative thermal expansion coefficients of CFRP parts can be utilized for a higher thermal stability of the machines [18]. As a consequence of the

buildup and internal structure of composite parts, including fibers and matrix, by exploiting the design degrees of freedom regarding the types of fibers, fiber orientation, and layer composition, quasi-isotropic or targeted anisotropic mechanical and thermal characteristics can be created.

In industrial machinery such as for semiconductor manufacturing equipment that requires high dimensional accuracy, it is essential to consider materials with high stiffness and dimensional stability (low thermal expansion) rather than strength or damage resistance against high mechanical loads. In addition to such properties, quasi-isotropy in terms of both the elastic modulus and coefficient of thermal expansion (CTE) is necessary, especially for precision surface plates.

CFRP laminate and FMLs are commonly produced at high temperatures, such as autoclave processing. After processing and subsequent cooling of composite laminate from the relatively high temperature to service temperature, residual stress/strain arise due to the significantly higher shrinkage of matrix compare with fibers. This type of residual stress/strain formation is present in all fiber-reinforced polymers and FMLs due to their inherent in-homogenous nature. The presence of residual stresses/strain influences the properties of the composite structures significantly. It is important that the residual thermal stresses/strain are taken into account in both the design and analytic modeling of composite structures.

This unexpected deformation is not only generated in composite processing but also in machining. In the machining-process, the transient and permanent residual strains appear due to cutting force, temperature, and machining-induced damage [19]. The presence of internal residual stress or strain due to processing and machining may cause

difficulties in assembly or degradation of in-service life of CFRP components. For instance, stress or strain generated during cure and cooling stages due to chemical and thermal shrinkage causes distortion of the component and affects the mechanical properties significantly [26, 27]. Therefore, it is essential to minimize the deformation after processing and machining in order to assure the structural integrity of the final part.

1.2. Literature Review

Figure 1-4 presents the CFRP manufacturing process and the focus area of the present study. As mentioned previously, in any manufacturing, particularly in the cure processing and machining of composite, unexpected deformation due to the presence of residual stress or strain after processing and machining must be minimized for part quality assurance.

Numerous studies have been carried out with regard to residual stress or strain during the processing of CFRP. In the curing process of CFRP, it has been reported that several factors such as chemical (cure) shrinkage, thermal shrinkage/expansion, laminate lay-up, cure time and temperature, and mold thermal expansion affect shape deformation and damage initiation of composite through the development of residual stress or strain [26],[53-59].

In the machining-process of CFRP, the transient and permanent residual strains appear due to cutting force, temperature, and machining-induced damage [19]. Most studies in the machining of CFRP related to the tool materials and geometry [60,61], machining conditions such as feed rate, cutting speed, cutting materials, and quality of the part machined [30]–[38]. However, little attention has been paid to the relation between the residual strain during machining and machining induced-damage except for

some literature [39]. In addition, in-situ strain monitoring during machining using FBG sensors has not been reported thus far, although such sensors were employed for detecting wear of drilling tools [40] and damage evolution from a drilled hole [41]. Therefore, to assure the structural integrity of the CFRP part/component, it is essential to clarify deformation and damage state during and after processing and machining.

To date, a variety of methods have been developed to measure the residual and thermal strains in composite materials [42,43],[52]–[54],[44]–[51][55]. Strain measurement methods are generally classified into two categories: (i) point-by-point measurement and (ii) full-field measurement. The electric resistance strain gauge measurement is the most common among the first category [42]. The strain gauges can not only be bonded to the surface of the specimen but also embedded in the specimen. For example, Kanerva et al.[45] measured residual strain in a CFRP/tungsten hybrid laminate using both embedded strain gauges and fiber Bragg grating (FBG) sensors. Another point-by-point method is Raman Micro-spectroscopy, by which the stress or strain is estimated from the peak shift of Raman scattering (Raman shift) with the change in the vibration energy of molecules [54]. The third method of the first category is measurement using fiber optic sensors, such as extrinsic Fabry-Perrot interferometry (EFPI) sensors [53] and FBG sensors [36, 43, 47]. EFPI sensors are immune to ambient temperature fluctuation. A disadvantage of EFPI sensors is the relatively large diameter that leads to perturbation of the strain around the embedded sensor. In contrast, FBG sensors with smaller diameters are more appropriate for embedding in a composite laminate, although they need temperature compensation when subjected to temperature change. Moiré interferometry [45, 46], digital image correlation (DIC) [38, 43], and speckle interferometry [40, 44] are classified into the full-field measurement category.

The above three methods have the advantage of non-contact full-field measurement, generally coupled with image processing. However, it is difficult to precisely obtain small thermal strains of a laminate heated in a thermostatic chamber or an autoclave because the light does not directly reach the target to be measured. Furthermore, thermomechanical analysis (TMA) is commonly used to measure the CTE of a composite [56]. Careful sample preparation is crucial for accurate TMA measurement of near-zero CTE with an absolute value less than $1x10^{-6}$/°C. For the above reasons, embedded FBG sensors are the most suitable for the measurement of small thermal strains (less than 100 με) or CTE, so long as the appropriate temperature compensation is performed.

FBG sensor not only useful tools to monitor the internal strain during curing but also the machining process. In an extensive review by Luyckx et al. [55], some technical issues were described on the strain monitoring of fibrous composites using embedded FBG sensors. Minakuchi et al. [43] used embedded FBG sensors to calculate residual stress by simultaneously determining shrinkage strain and stiffness change during curing. They also developed a fiber-optic-based technique for tensile characterization of direction-dependent cure-induced shrinkage in thermoset fiber-reinforced composite [57]. Oliveira et al.[58] investigated the influence of the mold material on the build-up of internal stresses during autoclave cure of carbon fiber composites by using embedded FBG sensors. Takeda et al. [59] discussed the reflection spectra form from the FBG sensor correlated with delamination length.

Much work has been performed investigating the properties of FMLs [60]. Representative FMLs developed for aircraft structure are ARRAL [61], aramid reinforced aluminum laminate, GLARE [62], glass-reinforced aluminum laminate, CARRAL [63], carbon-reinforced aluminum laminates, and TiGr. [64], titanium graphite laminate. These

materials have high resistance against fatigue and impact. In contrast, because stiffness and dimensional stability are the most critical properties for industrial machinery, steel can be a candidate as the metal used for FMLs. There is a possibility of Galvanic corrosion in an FML made of steel and CFRP [65]. However, this does not matter because most precision industrial machinery is operated under controlled humidity environments. Another concern is the integrity of adhesion between the steel and CFRP [66]. This is not significant either because the applied strain in such applications is supposed to be small enough not to generate interfacial damage.

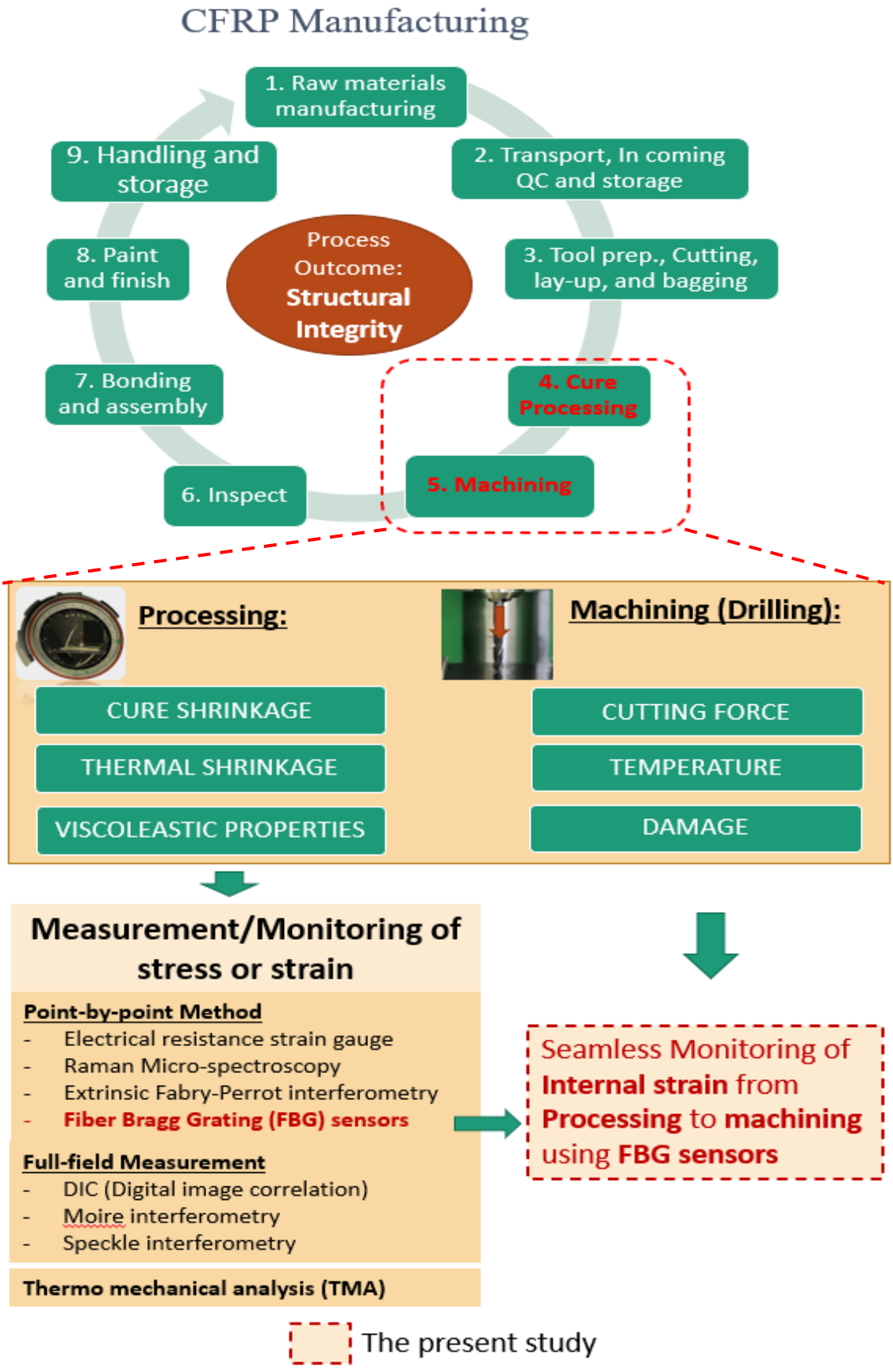

Figure 1- 4 Focus of the present study in the field of CFRP manufacturing.

1.3. Research Objectives

The objectives of this study are as follows:

(i) Investigation of the internal strain of CFRP laminate during processing and machining.

(ii) Development and verification of very low CTE of a CFRP-metal laminate using FBG sensors.

1.4. Thesis Outline

This thesis comprises five chapters, as shown in Figure 1-4. Chapter One introduces the general background of CFRP and FML and their application in various industries, problem statement, and objective of the study. This chapter also reviews the previous studies in internal stress/strain measurement of composite laminates. Chapter Two elaborates on the theoretical background. It describes the Fiber Bragg Grating (FBG) sensor as a useful tool for temperature strain monitoring and laminate theory. Chapter Three investigates the internal strain from processing to machining seamlessly. Process-induced strain and machining induced strain discussed in detail, as well as damage-induced strain after drilling. It is found the novelty of this study in this chapter that the machining-induced strain was correlated with not only damage or delamination size but also its relative position of sensors. Chapter Four discusses the design of a quasi-isotropic fiber metal laminate (FML) with a low Coefficient of thermal expansion (CTE) and high specific modulus based on lamination theory. The temperature dependance of the FML CTE is also discucessed and inestigated via finite element analysis. Chapter Five presents the general conclusion of this research and future work.

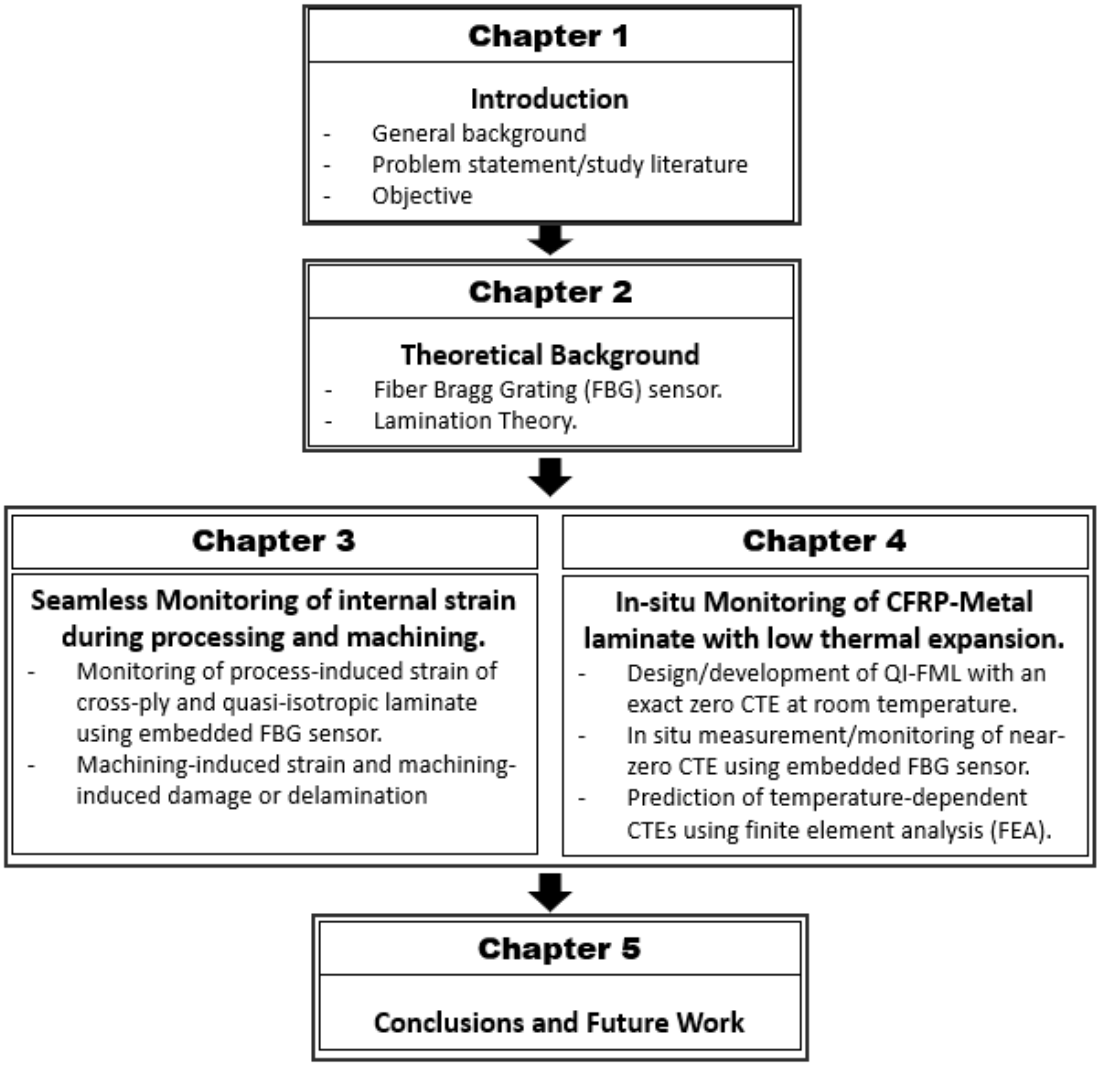

Figure 1- 5 Thesis Outline

CHAPTER 2: THEORETICAL BACKGROUND

2.1. Fiber Bragg Grating (FBG) Sensor

FBG sensor is optical fiber sensors that have many advantages, i.e., lightweight, small size, high resolution, accuracy, and immunity to electromagnetic interference. These sensors have been employed in a variety of engineering applications such as health monitoring of composite structures[67][68], operational load monitoring of wind turbine blades, non-destructive evaluation, and damaging detection[41][69]. They are helpful because they enable direct measurement of strain in the interior of a host structure at critical locations, thus providing useful information about the high strain state in a complicated structure. The optical fiber sensors can be classified into three different types of sensors based on the light parameters, which are modulated, namely, wavelength, phase, and intensity. FBG sensors based on wavelength modulation have been widely used in structural health monitoring.

2.1.1. Principle of FBG sensor

FBGs are obtained by creating periodic variations in the refractive index of the core of an optical fiber. Figure 2-1 shows the internal structure of an optical fiber with an FBG written in it.

When light propagates through the grating at a particular wavelength, called the Bragg wavelength, the light reflected by the different zones of refractive indices will be in phase and amplified. The Bragg wavelength is expressed as

$$\lambda_B = 2n\Lambda \quad (1)$$

Where λ_B is the Bragg wavelength, n is the effective refractive index of the FBG, and Λ is the grating period? Here, n and Λ both depend on the strain and temperature, so the Bragg wavelength is sensitive to both of them.

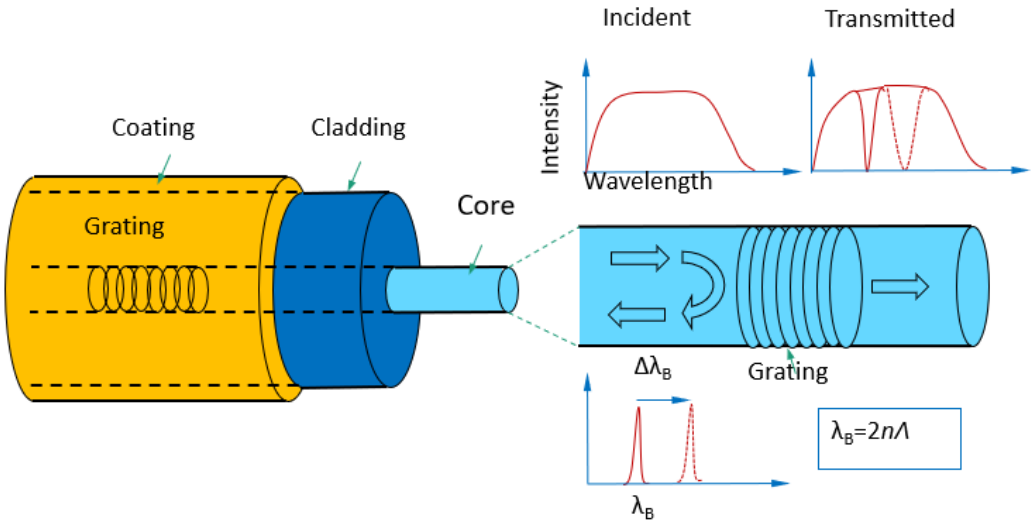

Figure 2- 1 Basic principle of FBG sensor

2.1.2. Strain and Temperature Sensitivity

The wavelength of FBG changes with strain and temperature according to the equation (1)

$$\frac{\Delta\lambda}{\lambda_0} = k.\varepsilon + \alpha_\delta.\Delta T \quad (2)$$

$\Delta\lambda$ = wavelength shift

λ_0 = base wavelength

$$k = 1 - p \quad (3)$$

p = photo elastic coeficient, $p = 0.22$

k = gage factor, $k = 0.78$

ε = strain

ΔT = temperature change

α_δ = change of the refraction index,

α_δ = 5...8*10^{-6}/K

$$\alpha_\delta = \frac{\delta n/n}{\delta T} \tag{4}$$

The first expression ($k * \varepsilon$) of equation (2) describes the strain impact caused by force (ε_m) and temperature (ε_T). The second part ($\alpha_\delta * \Delta T$) describes the change of the glass refraction index *n* caused only by temperature.

$$\varepsilon = \varepsilon_m + \varepsilon_T \tag{5}$$

ε_m = mechanically caused strain

ε_T = temperature caused strain

$$\varepsilon_T = \alpha_{sp}.\Delta T \tag{6}$$

α_{sp} = expansion coefficient per K of specimen

Equations (2), (3) and (6) lead to equations (7) and (8) which describe the behavior of an FBG under the impact of both strain and temperature

$$\frac{\Delta\lambda}{\lambda_0} = (1-p).\left(\varepsilon_m + \alpha_{sp}.\Delta T\right) + \frac{\delta n/n}{\delta T}.\Delta T \tag{7}$$

$$\frac{\Delta\lambda}{\lambda_0} = k.\left(\varepsilon_m + \alpha_{sp}.\Delta T\right) + \alpha_\delta.\Delta T \tag{8}$$

In the case of a pure temperature sensor, a Bragg grating is not stressed (the fiber then is fixed only at one point, sufficiently apart from the Bragg grating). The FBG $\Delta\lambda/\lambda_0$ the signal then changes only with temperature according to equation (9). In this case, α is the thermal expansion coefficient (α_{glass})glass of the fiber.

$$\frac{\Delta\lambda}{\lambda_0} = (1-p).\left(\alpha_{glass}.\Delta T\right) + \frac{\delta n/n}{\delta T}.\Delta T \tag{9}$$

$$\frac{\Delta\lambda}{\lambda_0} = (k.\alpha_{glass} + \alpha_\delta).\Delta T \tag{10}$$

$$\Delta T = \frac{1}{k.\alpha_{glass} + \alpha_\delta} \frac{\Delta\lambda}{\lambda_0} \tag{11}$$

Equation (11) for a temperature-measuring FBG, $\alpha_{glass} = 0.55 * 10^{-6}/K$.

The expansion coefficient α_{glass} of the fiber is very low or almost zero. The most significant impact results from the temperature-dependent change of the refraction index α_δ. When a fiber is embedded to a specimen, the FBG signal $\Delta\lambda/\lambda_0$ changes with the strain $(\varepsilon_m + \varepsilon_T)$ of the specimen and therefore the thermal expansion coefficient is α_{sp} then and not α_{glass}.

$$\frac{\Delta\lambda}{\lambda_0} = k.\varepsilon_m + (k.\alpha_{sp} + \alpha_\delta).\Delta T \tag{12}$$

$$\varepsilon_m = \frac{1}{k}\frac{\Delta\lambda}{\lambda_0} - \left(\alpha_{sp} + \frac{\alpha_\delta}{k}\right).\Delta T \tag{13}$$

Equation (13) for a strain-measuring FBG.

When the FBG is fixed to the specimen on a region without mechanical strain ($\varepsilon_m = 0$) it works as a temperature compensation FBG. Its signal calculates, according to equations (14) and (15).

$$\frac{\Delta\lambda}{\lambda_0} = (k.\alpha_{sp} + \alpha_\delta).\Delta T \tag{14}$$

$$\Delta T = \frac{1}{k.\alpha_{sp} + \alpha_\delta} \frac{\Delta\lambda}{\lambda_0} \tag{15}$$

Equation (14) and (15) for temperature compensation.

There are several temperature compensations have been proposed to measure strain. Minakuchi proposed a simple formula as follows:

$$\lambda_B = \frac{\varepsilon}{C_s} + \frac{\Delta T}{C_T} \tag{16}$$

$$\varepsilon = C_s\left(\lambda_B - \frac{\Delta T}{C_T}\right) \tag{17}$$

Where C_S is the wavelength–strain sensitivity and C_T is the wavelength–temperature sensitivity. Preliminary calibration tests determine these sensitivity parameters. To obtain FBG axial strain ε from the measured wavelength shift $\Delta\lambda_B$, it is necessary to uncouple the strain and temperature contributions to the wavelength shift.

2.2. Laminate Theory and CTE

2.2.1. Generalized Hooke's Law For Nonisotropic Materials

Normal Stress and Strain, Uniaxially Applied Force.

Figure 2-2 is a schematic of an isotropic and a unidirectional fiber-reinforced material. The stiffness of the isotropic plate can be described by one value, the modulus, E, of the material, regardless of the direction of load. Two values must describe the stiffness of the orthotropic plate, one along the longitudinal direction of the fibers, commonly referred to as E_L, and one transverse to the direction of fibers, usually denoted by E_T. Subscripts 1 and 2 will be used such that $E_L = E_1$ and $E_T = E_2$. Thus, indices must be added to the stress, strain, and modulus values to describe the direction of the applied force. For example, for an isotropic material, the stress-strain relationship is written:

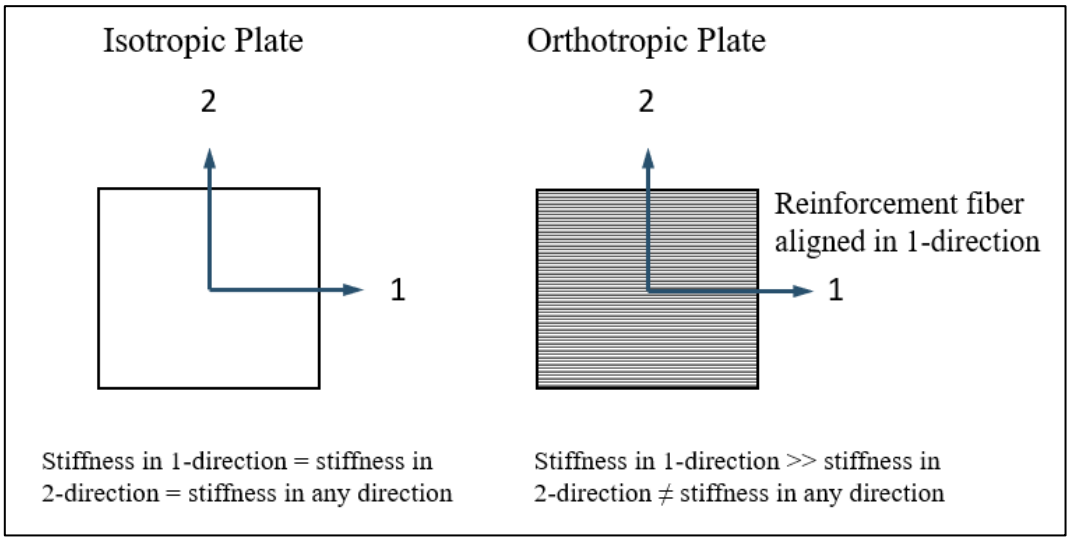

Figure 2- 2 Difference between an isotropic and an orthotropic plate.

For the orthotropic system, the direction must be specified. For example:

$$\sigma_1 = E_1\varepsilon_1 \quad \text{or} \quad \sigma_2 = E_2\varepsilon_2 \tag{18}$$

If the applied load acts either parallel or perpendicular to the fibers, then the plate is considered specially orthotropic.

2.2.2. Stress and Strain, Plane Stress for Specially Orthotropic Plate

In general, plates will experience stresses in more than one direction within the plane. This is referred to as plane stress. Also, Poisson's ratio now becomes essential. Poisson's ratio is the ratio of the strain perpendicular to a given loading direction to the strain parallel to this given loading direction:

$$\text{Poisson Ratio} = \nu_{12} = \frac{\varepsilon_T}{\varepsilon_L} = \frac{\varepsilon_2}{\varepsilon_1} \quad or \quad \nu_{21} = \frac{\varepsilon_L}{\varepsilon_T} = \frac{\varepsilon_1}{\varepsilon_2} \tag{19}$$

The strain components are now stretch due to an applied force, minus the contraction of Poisson's effect due to another force perpendicular to this applied force. Thus:

$$\varepsilon_1 = \frac{\sigma_1}{E_1} - \nu_{21}\varepsilon_2 \;\; and \;\; \varepsilon_2 = \frac{\sigma_2}{E_2} - \nu_{12}\varepsilon_1 \tag{20}$$

The equation can be written in matrix form:

$$\begin{bmatrix} \varepsilon_1 \\ \varepsilon_2 \\ \gamma_{12} \end{bmatrix} = \begin{bmatrix} S_{11} & S_{12} & 0 \\ S_{12} & S_{22} & 0 \\ 0 & 0 & S_{66} \end{bmatrix} \begin{bmatrix} \sigma_1 \\ \sigma_2 \\ \tau_{12} \end{bmatrix} \tag{21}$$

Where

$S_{11} = 1/E_1$,

$S_{22} = 1/E_2$,

$S_{12} = -\nu_{12}/E_1 = -\nu_{21}/E_2$,

$S_{66} = 1/G_{12}$

Note that the 3,3 position in this 3x3 matrix is called the compliance matrix.

By inverting the compliance matrix, we can get stress as a function of strain.

$$\begin{bmatrix} \sigma_1 \\ \sigma_2 \\ \tau_{12} \end{bmatrix} = \begin{bmatrix} Q_{11} & Q_{12} & 0 \\ Q_{12} & Q_{22} & 0 \\ 0 & 0 & Q_{66} \end{bmatrix} \begin{bmatrix} \varepsilon_1 \\ \varepsilon_2 \\ \gamma_{12} \end{bmatrix} \tag{22}$$

Where

$$Q_{11} = \frac{E_1}{1 - \nu_{12}\nu_{21}}$$

$$Q_{22} = \frac{E_2}{1 - \nu_{12}\nu_{21}}$$

$$Q_{12} = \frac{\nu_{12}E_2}{1 - \nu_{12}\nu_{21}} = \frac{\nu_{21}E_1}{1 - \nu_{12}\nu_{21}}$$

$$Q_{66} = G_{66}$$

The Q's are referred to as the reduced stiffnesses, and the matrix is abbreviated as [Q].

2.2.3. Stress and Strain, Plane Stress for Generally Orthotropic Plates

Now suppose that the unidirectional lamina in figure 2-3 is loaded at some angle other than 0° or 90°. The lamina is now referred to as generally orthotropic since, in general, the loading direction does not coincide with the principal material directions. The stresses and strains must be transformed into coordinates that do coincide with the principal material directions. This can be accomplished using the free-body diagram in figure (6). From free body diagram (a), and summing forces in &e 1-direction:

$$\sigma_1 = \sigma_x \cos^2\theta + \sigma_y \sin^2\theta + 2\tau_{xy} \sin\theta \cos\theta \tag{23}$$

$$\sigma_2 = \sigma_x \sin^2\theta + \sigma_y \cos^2\theta - 2\tau_{xy} \sin\theta \cos\theta \tag{24}$$

$$\tau_{12} = -\sigma_x \sin\theta \cos\theta + \sigma_y \sin\theta \cos\theta + 2\tau_{xy}(\cos^2\theta - \sin^2\theta) \tag{25}$$

Equation (14) can be written in matrix form as:

$$\begin{bmatrix} \sigma_1 \\ \sigma_2 \\ \tau_{12} \end{bmatrix} = \begin{bmatrix} cos^2\theta & sin^2\theta & 2\, sin\theta cos\theta \\ sin^2\theta & cos^2\theta & -2\, sin\theta cos\theta \\ -sin\theta cos\theta & sin\theta cos\theta & (cos^2\theta - sin^2\theta) \end{bmatrix} \begin{bmatrix} \sigma_x \\ \sigma_y \\ \tau_{xy} \end{bmatrix} \tag{26}$$

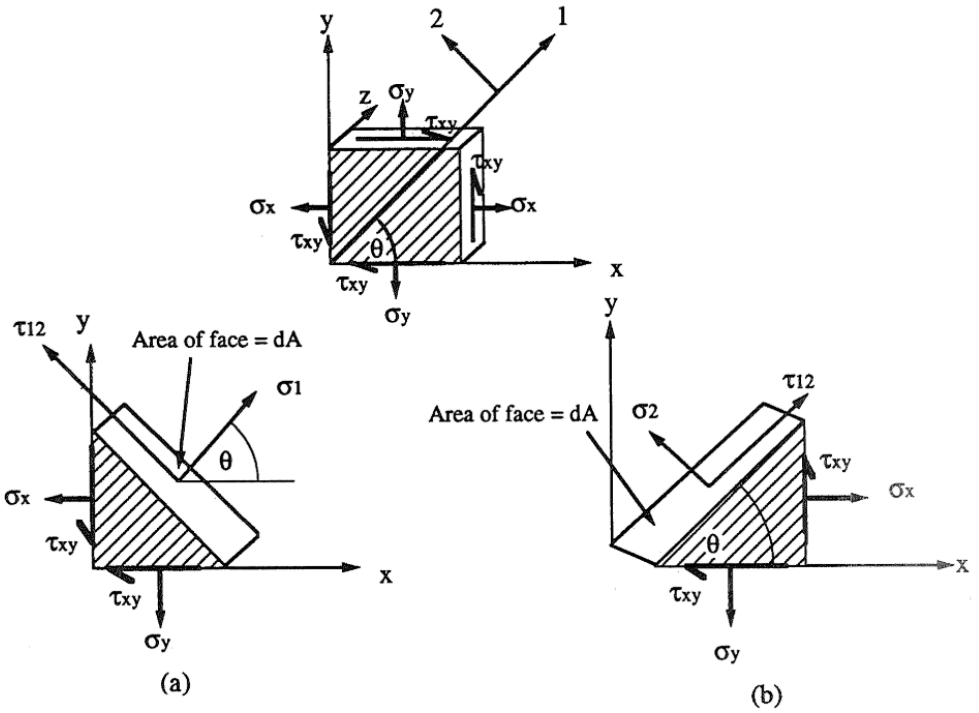

Figure 2- 3 Generally orthotropic lamina

The 3x3 matrix in equation (26) is called the transformation matrix and is denoted by *[T]*. The same matrix is used to transform strains. To change the matrix from the 1-2 coordinate system to the x-y coordinate system, the inverse of *[T]* must be calculated and given by:

$$[T]^{-1} = \begin{bmatrix} cos^2\theta & sin^2\theta & -2\,sin\theta cos\theta \\ sin^2\theta & cos^2\theta & 2\,sin\theta cos\theta \\ sin\theta cos\theta & -sin\theta cos\theta & (cos^2\theta - sin^2\theta) \end{bmatrix} \quad (27)$$

$$\begin{bmatrix} \sigma_1 \\ \sigma_2 \\ \tau_{12} \end{bmatrix} = [T] \begin{bmatrix} \sigma_x \\ \sigma_y \\ \tau_{xy} \end{bmatrix} \; and \; \begin{bmatrix} \sigma_x \\ \sigma_y \\ \tau_{xy} \end{bmatrix} = [T]^{-1} \begin{bmatrix} \sigma_1 \\ \sigma_2 \\ \tau_{12} \end{bmatrix} \quad (28)$$

Similiar for strain;

$$\begin{bmatrix} \varepsilon_1 \\ \varepsilon_2 \\ \varepsilon_{12} \end{bmatrix} = [T] \begin{bmatrix} \varepsilon_x \\ \varepsilon_y \\ \varepsilon_{xy} \end{bmatrix} \; and \; \begin{bmatrix} \varepsilon_x \\ \varepsilon_y \\ \varepsilon_{xy} \end{bmatrix} = [T]^{-1} \begin{bmatrix} \varepsilon_1 \\ \varepsilon_2 \\ \varepsilon_{12} \end{bmatrix} \quad (29)$$

2.2.4. Laminate Theory

2.2.4.1 Laminate Coordinate system

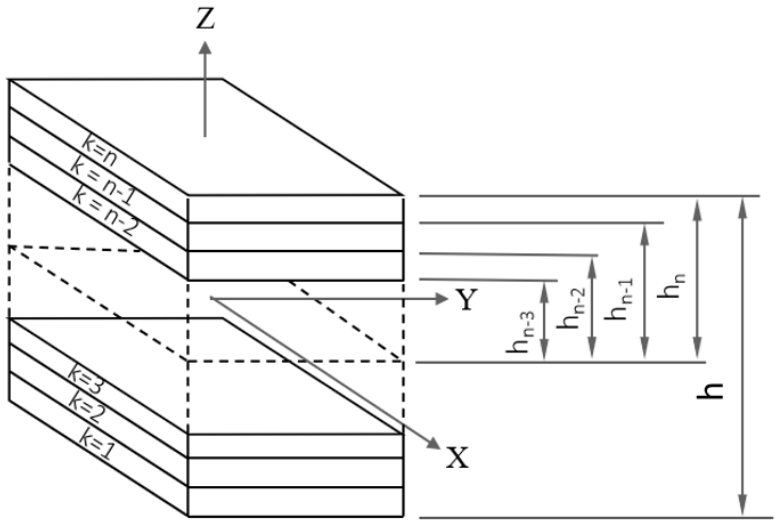

Figure 2- 4 Notation for laminate coordinate within a laminae

2.2.4.2 Classical Laminate Theory

The classical laminate theory is a direct extension of the classical plate theory for isotropic and homogeneous material. The expansion of this theory to laminates requires some modifications to take into account the inhomogeneity in the thickness direction. In the following, the assumptions made in this theory, along with the assumptions made for classical plate theory, are given.

- The laminate consists of perfectly bonded layers. There is no slip between the adjacent layers. In other words, it is equivalent to saying that the displacement components are continuous through the thickness.
- Each lamina is considered to be a homogeneous layer such that its effective properties are known.
- Each lamina is in a state of plane stress.
- The individual lamina can be isotropic, orthotropic, or transversely isotropic.

- The laminate deforms according to the Kirchhoff - Love assumptions for bending and stretching of thin plates (as assumed in classical plate theory). The assumptions are: (a) The normals to the mid-plane remain straight and normal to the midplane even after deformation, (b) The normals to the mid-plane do not change their lengths.

This theory is known as the classical laminated plate theory and abbreviated as CLPT.

2.2.4.3 Strain Displacement Relationship

Consider a section of laminate in the x-y plane, which is deformed due to some loading, as in figure 2-5. We assume the point A at the geometrical midplane undergoes some displacement u_0 in the x-direction. Also, we assume that the normal (perpendicular) to the deformed midplane. Displacement C in the x-direction is given by the linear relationship

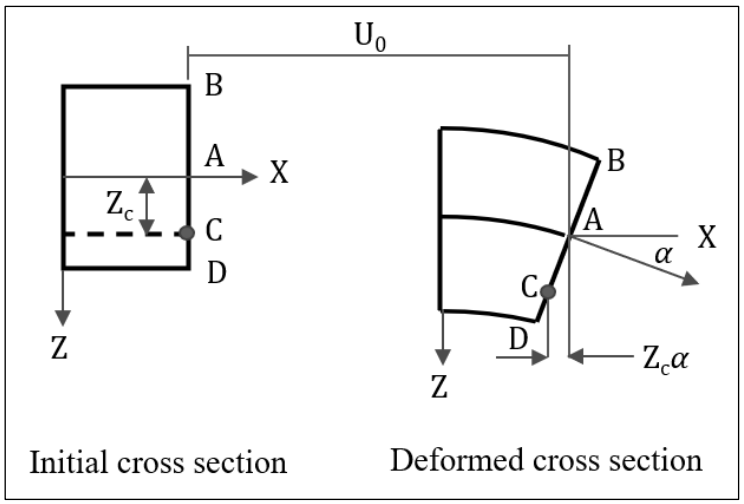

Figure 2- 5 Bending Geometry in the x-z plane.

$$u_c = u_0 - z_c\alpha \tag{30}$$

$$\alpha = \frac{\partial_w}{\partial_x} \tag{31}$$

$$u = u_0 - z\frac{\partial_w}{\partial_x} \tag{32}$$

$$v = v_0 - z\frac{\partial_w}{\partial_y}$$

$$v = v_0 - z\frac{\partial_w}{\partial_y} \tag{33}$$

Where v_0 is the midplane displacement in the y-direction

Then the strain-stain relationships displacement equation can be written in terms of the midplane strain ε_x^0 ,ε_y^0 ,γ_{xy}^0 , and the plate curvature k_x^0 ,k_y^0 ,$k\gamma_{xy}^0$, as follow:

$$\begin{bmatrix}\epsilon_x\\ \epsilon_y\\ \gamma_{xy}\end{bmatrix} = \begin{bmatrix}\epsilon_x^0\\ \epsilon_y^0\\ \gamma_{xy}^0\end{bmatrix} + z\begin{bmatrix}k_x\\ k_y\\ k_{xy}\end{bmatrix} \tag{34}$$

2.2.4.4 Laminate Constitutive Equations

The stress resultants can be written in the form of a vector as follows:

$$\begin{bmatrix}N_x\\ N_y\\ N_{xy}\end{bmatrix} = \int_{-h/2}^{h/2}\begin{bmatrix}\sigma_x\\ \sigma_y\\ \tau_{xy}\end{bmatrix}dz \tag{35}$$

$$\begin{bmatrix}N_x\\ N_y\\ N_{xy}\end{bmatrix} = \begin{bmatrix}A_{11} & A_{12} & A_{16}\\ A_{12} & A_{22} & A_{26}\\ A_{16} & A_{26} & A_{66}\end{bmatrix}\begin{bmatrix}\epsilon_x^0\\ \epsilon_y^0\\ \gamma_{xy}^0\end{bmatrix} + \begin{bmatrix}B_{11} & B_{12} & B_{16}\\ B_{12} & B_{22} & B_{26}\\ B_{16} & B_{26} & B_{66}\end{bmatrix}\begin{bmatrix}k_x\\ k_y\\ k_{xy}\end{bmatrix} \tag{36}$$

$$[N] = [A][\epsilon^0] + [B][k] \tag{37}$$

where

$$A_{ij} = \sum_{k=1}^{n}(\bar{Q}_{ij})_k(h_k - h_{k-1}) \tag{38}$$

$$B_{ij} = \frac{1}{2}\sum_{k=1}^{n}(\bar{Q}_{ij})_k(h_k^2 - h_{k-1}^2 \tag{39}$$

Equation (37) is the midplane stress resultants for general laminated.

In the case of laminate influenced by thermal, for general laminate, the equation (37) becomes:

$$[N] = [A][\epsilon^0] + [B][k] - N^T \tag{40}$$

where N^T is thermal stress resultant.

In a symmetric laminate, each B_{ij} is zero ($B_{16} = B_{26} = 0$), therefore equation (40) can be written:

$$[N] = [A][\epsilon^0] - N^T \tag{41}$$

or

$$\begin{bmatrix} N_x \\ N_y \\ N_{xy} \end{bmatrix} = \begin{bmatrix} A_{11} & A_{12} & 0 \\ A_{12} & A_{22} & 0 \\ 0 & 0 & A_{66} \end{bmatrix} \begin{bmatrix} \epsilon_x^0 \\ \epsilon_y^0 \\ \gamma_{xy}^0 \end{bmatrix} - \begin{bmatrix} {N_x}^T \\ {N_y}^T \\ {N_{xy}}^T \end{bmatrix} \tag{42}$$

$$[A] = \int_{-h/2}^{h/2} Q\, dz = \sum_{k=1}^{n} Q_k t_k \tag{43}$$

where Q_k and t_k is stiffness matris of the *k-th* and thickness of the *k-th* lamina respectively.

$$N^T = \int_{-h/2}^{h/2} Q\varepsilon^T dz = \sum_{k=1}^{n} Q_k \varepsilon_k^T\, t_k \tag{44}$$

The thermal strain of the *h-th* lamina can be expressed as:

$$\varepsilon_k^T = \begin{bmatrix} \alpha_x \\ \alpha_y \\ \alpha_{xy} \end{bmatrix}_k \Delta T \tag{45}$$

In processing (curing), when applied stress is zero *N=0*, equation (41) becomes

$$[\varepsilon] = [A^{-1}]\,[N]^T = \begin{bmatrix} \varepsilon_x \\ \varepsilon_y \\ \gamma_{xy} \end{bmatrix} \tag{46}$$

In a cross-ply laminate, stiffnes matrix of 0°-ply and 90°-ply as follows:

$$0^o - ply: \quad Q_1 = \begin{bmatrix} Q_{11} & Q_{12} & 0 \\ Q_{12} & Q_{22} & 0 \\ 0 & 0 & Q_{66} \end{bmatrix}, \quad \varepsilon_1^T = \begin{bmatrix} \beta_1 \\ \beta_2 \\ 0 \end{bmatrix} \tag{47}$$

$$90^o - ply: \quad Q_2 = \begin{bmatrix} Q_{22} & Q_{12} & 0 \\ Q_{12} & Q_{11} & 0 \\ 0 & 0 & Q_{66} \end{bmatrix}, \quad \varepsilon_2^T = \begin{bmatrix} \beta_2 \\ \beta_1 \\ 0 \end{bmatrix} \tag{48}$$

$$A_{11} = A_{22} = (Q_{11} + Q_{22})\frac{h}{2}, \quad A_{12} = Q_{12}h \tag{49}$$

$$A_{11} + A_{12} = \frac{h}{2}(Q_{11} + Q_{22} + 2Q_{12}) \tag{50}$$

where

$$[A^{-1}] = \frac{1}{{A_{11}}^2 - {A_{12}}^2}\begin{bmatrix} A_{11} & -A_{12} & 0 \\ -A_{12} & A_{11} & 0 \\ 0 & 0 & ({A_{11}}^2 - {A_{12}}^2)/A_{66} \end{bmatrix} \tag{51}$$

$$\begin{gathered} {N_x}^T = ({Q_1}{\varepsilon_1}^T + {Q_2}{\varepsilon_2}^T)\frac{h}{2} \\ {N_x}^T = (Q_{11}\beta_1\Delta T + Q_{12}\beta_2\Delta T + Q_{22}\beta_2\Delta T + Q_{12}\beta_1\Delta T)\frac{h}{2} \\ {N_x}^T = \{((Q_{11} + Q_{12})\beta_1 + (Q_{22} + Q_{12})\beta_2\}\Delta T\frac{h}{2} \\ {N_x}^T = {N_y}^T \end{gathered} \tag{52}$$

The in-plane thermal residual strain of cross-ply laminate can be calculated by following equation:

$$\varepsilon_x = \varepsilon_y = \frac{(Q_{11} + Q_{12})\beta_1 + (Q_{22} + Q_{12})\beta_2}{Q_{11} + Q_{22} + 2Q_{12}}\Delta T \tag{53}$$

Where $\beta_{ij}(j = 1,2)$ is the coefficient of thermal expansion laminate.

2.2.5. Thermal Expansion of Laminate

CTE (Coefficient of Thermal Expansion)

For a unidirectional continuous fiber lamina, coefficients of linear thermal expansion in the 0° and 90° directions can be calculated from the following equations[2]:

$$\alpha_{11} = \frac{\alpha_{fl} E_f v_f + \alpha_m E_m v_m}{E_f v_f + E_m v_m} \tag{54}$$

And

$$\alpha_{22} = (1 + v_f)\frac{(\alpha_{fl} + \alpha_{fr})}{2} V_f + (1 + v_m)\alpha_m v_m - \alpha_{11} v_{12} \tag{55}$$

where

$v_{12} = \nu_f V_f + \nu_m V_m$

α_{fl} = coefficient of linear thermal expansion for the fiber in the longitudinal (fiber) direction

α_{fr} = coefficient of linear thermal expansion for the fiber in the radial (perpendicular to fiber) direction

α_m = coefficient of linear thermal expansion for the matrix

If the fibers are at an angle θ with the x direction, the coefficients of thermal expansion in the x and y directions can be calculated using α_{11} and α_{22}:

$$\alpha_{xx} = \alpha_{11}\, cos^2\theta + \alpha_{22}\, sin^2\theta,$$

$$\alpha_{yy} = \alpha_{11}\, sin^2\theta + \alpha_{22}\, cos^2\theta, \qquad (56)$$

$$\alpha_{xy} = (2\, sin\,\theta\, cos\,\theta)(\alpha_{11} - \alpha_{22})$$

Where α_{xx} and α_{yy} are coefficients of linear expansion and α_{xy} is the coefficient of shear expansion. It is important to observe that, unless $\theta = 0$ or 90°, a change in temperature produces a shear strain owing to the presence of α_{xy}. The other two coefficients, α_{xx} and α_{yy}, produce extensional strains in the x and y directions, respectively.

CHAPTER 3. SEAMLESS MONITORING OF INTERNAL STRAIN DURING PROCESSING AND DRILLING IN A CFRP LAMINATE

3.1 Experimental Procedure

3.1.1 Material and sensors

The composite laminate used in this work is CFRP laminates fabricated by carbon fibers and epoxy prepreg containing a 60% fiber volume fraction. The matrix is an epoxy material, and the reinforcement is T700 carbon fibers. The physical properties of the composite specimens are given in table 3-1. Two types of stacking sequence were used in this study, cross-ply laminate $[(0°_2/90°_2)_3]_S$ and quasi-isotropic ply stacking sequence of $[0°_3/-45°_3/90°_2/45°_3]_S$.

Table 3-1 Physical property of the studied T700S/2592 CFRP composite[70].

Properties	English	Metric
Tensile Strength*	415 ksi	2,860 MPa
Tensile Modulus*	19 MSi	134 GPa
Tensile Strain	2.02%	
Compressive Strength*	210 ksi	1,450 MPa
Flexural Strength*	245 ksi	1,690 MPa
Flexural Modulus*	17 Msi	120 GPa
ILSS	13 Msi	86.9 MPa
In Plain Shear Strength	20 ksi	136 MPa
90° Tensile Strength	12 ksi	81 MPa

*Normalized to 60% fiber volume, cured with #2592 epoxy at 130 °C.

A small-diameter (145μm) FBG sensor (specification as listed in table 3-2) with a gauge length of 1 mm was embedded between 22nd- and 23rd-ply close to the exit of a hole so that the strain change due to drilling is sensitively detected as shown in figure

3-1. In addition, a thermocouple with an uncoated wire diameter of 75μm was also embedded near the FBG sensor to measure the temperature.

Table 3-2 The FBG sensor specification.

FBG Type	Single FBG
Gage length	1 mm
Diameter	145 μm
FBG Profile	apodized
Fiber type	Polyimide fiber
Fiber recoating	Polyimide recoat
Manufacturer	Technica Optical Component Company)

When the strain ε in the sensor axial direction and the temperature change ΔT are applied to the FBG sensor, the wavelength shift $\Delta\lambda_B$ is given equation (66) in the previous chapter

$$\varepsilon(\mu\varepsilon) = \frac{1\ x\ 10^6}{F_G}\frac{\Delta\lambda_{\boldsymbol{B}}}{\lambda_0} - \left(\frac{C_1}{F_G} - C_2\right)\Delta T$$

where $F_G = 0.838$ denotes the gage factor, $C_1 = 6.156\ \mu\varepsilon/\mathrm{K}$ the temperature coefficient of refractive index, $C_2 = 0.7\ \mu\varepsilon/\mathrm{K}$ the CTE of the FBG sensor and $\lambda_0 = 1550\ \mathrm{nm}$ the Bragg wavelength.

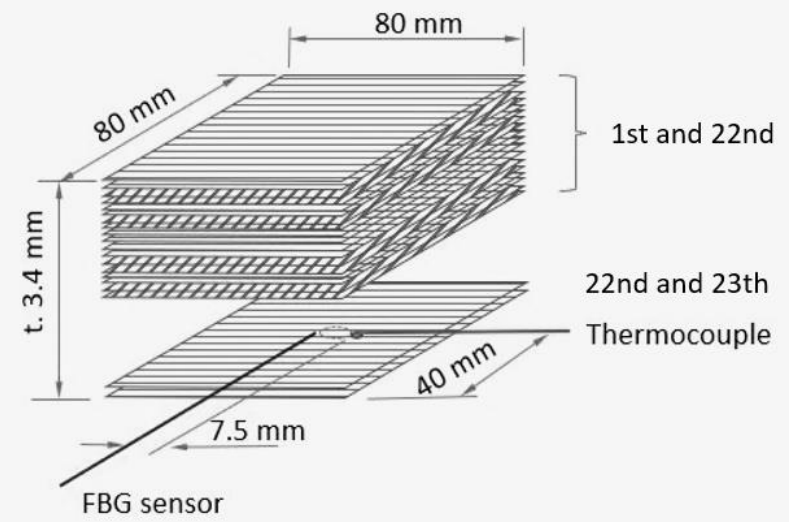

(a)

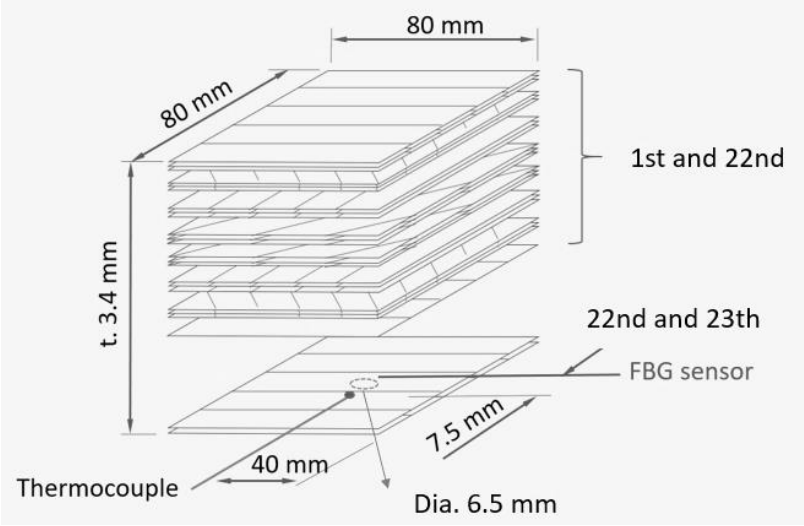

(b)

Figure 3- 1 Location of an FBG sensor and a thermocouple in (a) CFRP cross-ply laminate and (b) quasi-isotropic laminate.

3.1.2 Cure-process monitoring

Figure 3-2 illustrates the experimental setup for cure-process monitoring. A 160 mm square cross-ply laminate with an embedded FBG sensor and a thermocouple was set in a vacuum bag for autoclave processing. The laminate was fabricated at a pressure of 0.3 MPa and a temperature of 130°C for 2 hours.

The strain at the gel point when the laminate starts to vitrify was defined as zero of internal strain in both processing and drilling. The fiber volume fraction and thickness of the cured laminate were 0.6 and 3.4 mm, respectively.

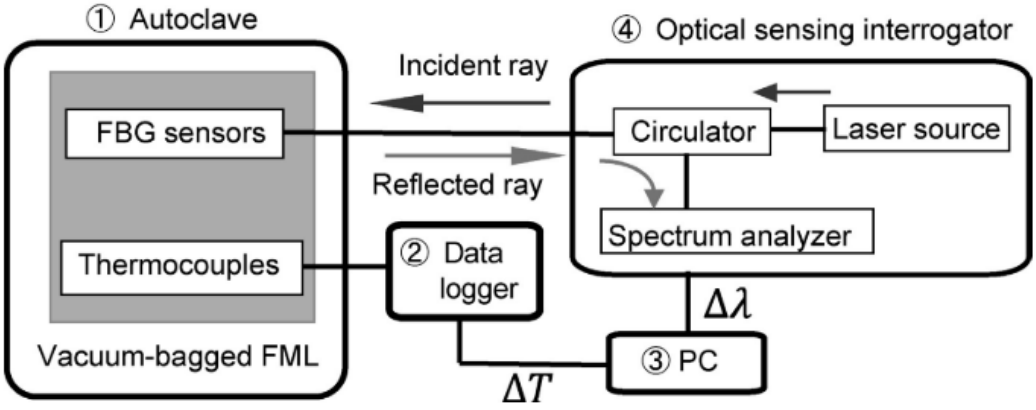

Figure 3- 2 Cure-process monitoring using an FBG sensor.

3.1.3 Drilling monitoring

Figure 3-3 depicts the experimental setup for real-time strain monitoring during drilling. The workpiece was fixed by a clamping device placed on the table of a drilling machine. The workpiece was moved upward (forward) at a predetermined feed rate by a step motor while a drill bit was kept fixed. The upward movement was stopped automatically when the tip of the drill bit was located at 2.8 mm below the bottom surface (full-penetration). After a few seconds, the workpiece was then moved downward (backward) at a constant feed rate of 0.5 mm/s. The strain and temperature were continuously measured after full penetration until the temperature became room temperature. Diamond-coating drill bits (ø 6.5 mm) with different wear conditions as well as high-speed steel drill bits were employed to induce various degrees of hole damage.

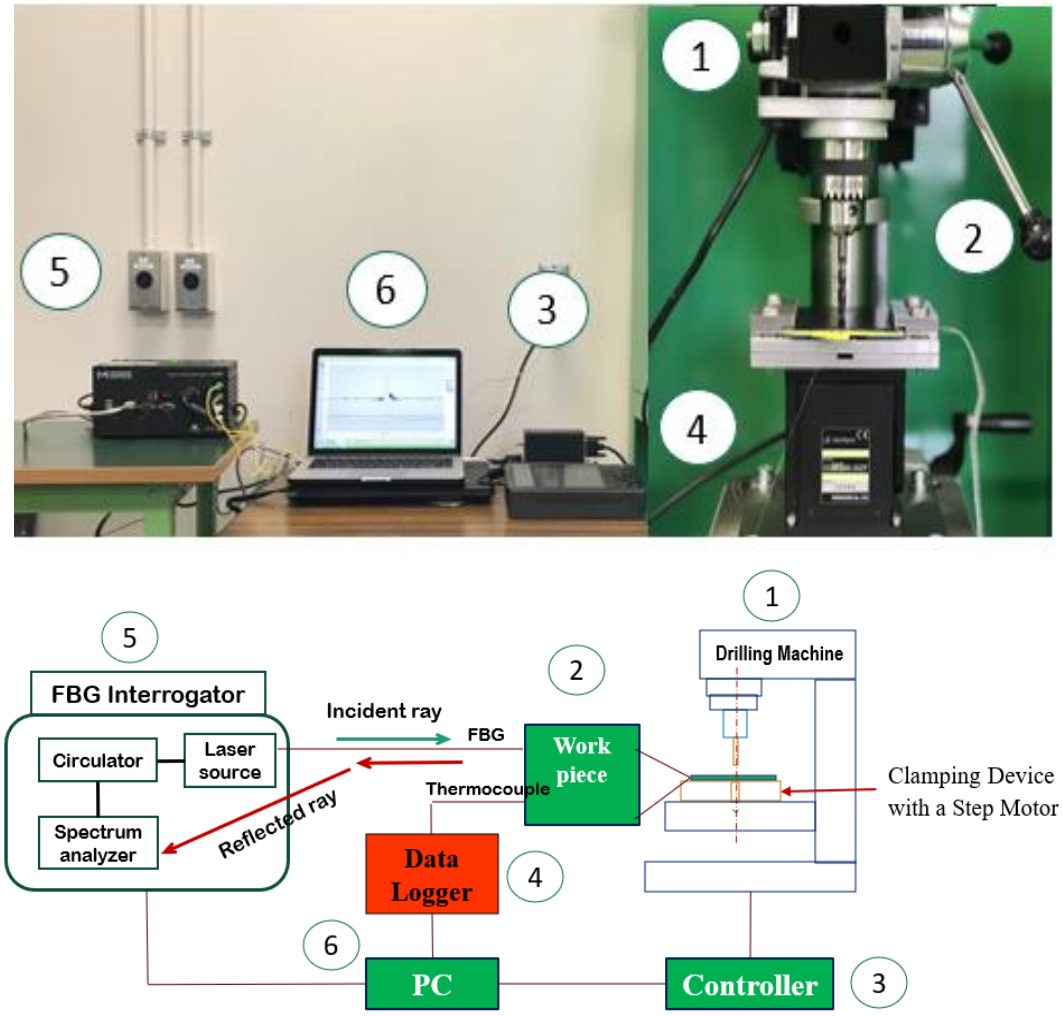

Figure 3- 3 Experimental setup for real-time strain monitoring during drilling.

Table 3-3 Drilling conditions.

Drill bit	diamond coating (DC)	high-speed steel (HSS)
Spindle speed (min^{-1})	3600	1600 / 3600
Forward feed Rate (mm/s)	0.3/ 0.5 / 1	0.3/ 0.5 / 1
Backward feed Rate (mm/s)	0.5	0.5

The drilling conditions are summarized in Table 3-3. The target distance-X between the center of the hole and the FBG sensor was roughly set to 3.75 mm, as shown in Figure 3-4. However, the location of the hole was slightly shifted because of

the backlash of the jig and the drill. Therefore, the exact location of the FBG sensor X and the damage size around a drilled hole was identified using soft X-ray radiography after drilling, as depicted in figure 3-4. To quantitatively evaluate the degree of damage around the drilled hole, an index named a delamination factor (Fd) [29][71] is used, which is defined as

$$F_{\mathrm{d}} = \frac{d_{\max}}{d_{\mathrm{nom}}} \tag{57}$$

where $d_{\max}$ is the maximum diameter of the delamination, and d_{nom} is the nominal hole diameter, which is approximately equal to the diameter of the drill bit (see Figure 3-5).

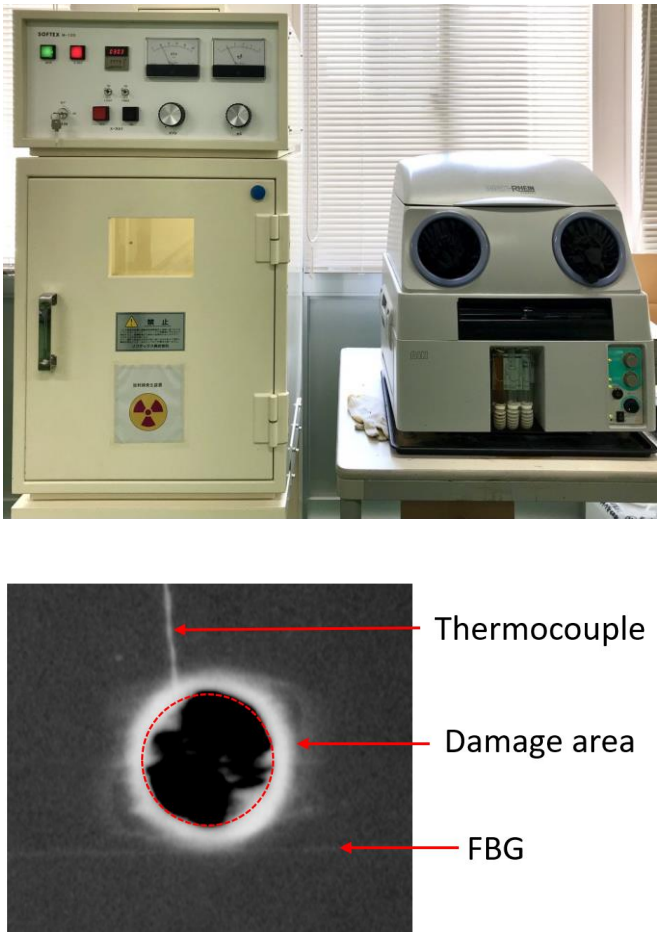

Figure 3- 4 The instrument of X-Ray radiography and x-ray experiment result sample.

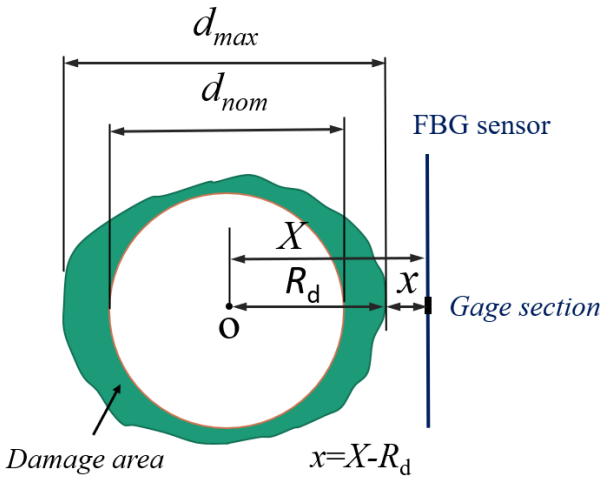

Figure 3- 5 Delamination size and location of the FBG sensor around a hole.

3.2. Result and Discussion

3.2.1 Process-Induced Strain of cross-ply laminates

Figure 3-6 shows the typical result of internal strain and temperature near the hole exit during processing. At the heating stage, the FBG sensor does not detect accurate strain yet since the resin is in a rubbery state with very low stiffness. After the gel point (at 110 min during the curing stage), cure shrinkage occurs, and the shrinkage strain of the laminate is transferred to the FBG sensor. The average cure shrinkage strain was $-30.6\ \mu\varepsilon$. This value is much smaller than that in the transverse direction of a unidirectional (UD) laminate of the same material (${\varepsilon_2}^C$ value is around $-2500\ \mu\varepsilon$) [43]. In contrast, the average thermal shrinkage strain during the cooling stage was $-336.0\ \mu\varepsilon$. Therefore, the measured process-induced train was $-366.6\ \mu\varepsilon$ in total.

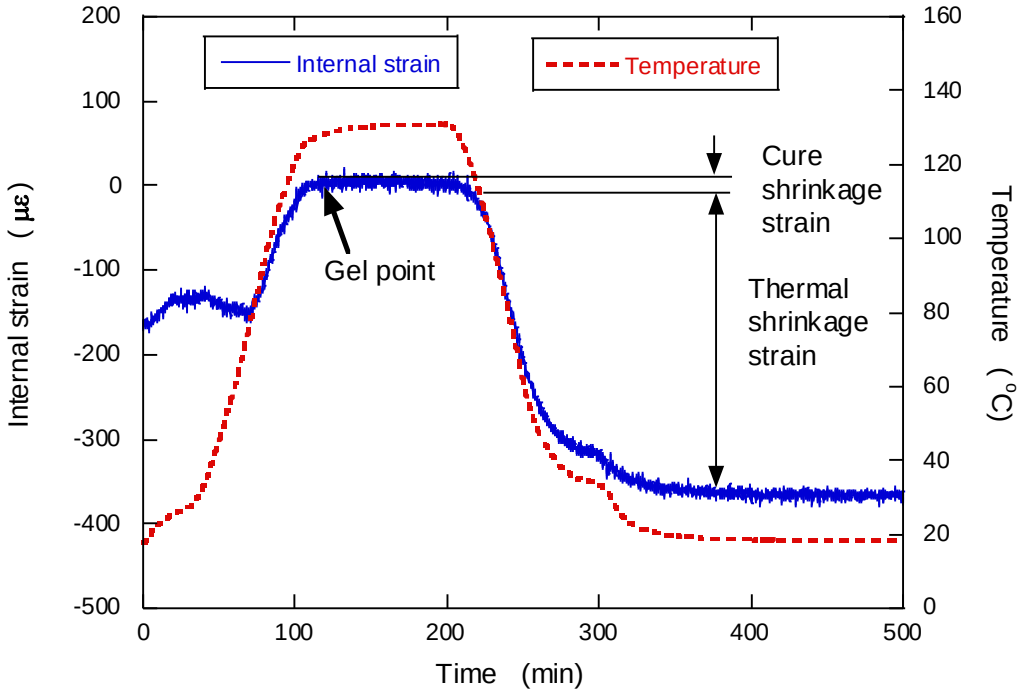

Figure 3- 6 The internal strain and temperature of a CFRP cross-ply laminate during processing.

When the volumetric shrinkage strain of epoxy resin λ_{m} is provided, the coefficients of a UD laminate λ_j $(j = 1, 2)$ are expressed based on a micromechanical model as [72]

$$\lambda_1 = \frac{(\lambda_{\mathrm{m}}/3)E_{\mathrm{m}}(1 - V_{\mathrm{f}})}{E_{11\mathrm{f}}V_{\mathrm{f}} + E_{\mathrm{m}}(1 - V_{\mathrm{f}})} \tag{58}$$

$$\lambda_2 = \left(\frac{\lambda_{\mathrm{m}}}{3}\right)(1 + \nu_m)(1 - V_{\mathrm{f}}) - \nu_{12}\lambda_1 \tag{59}$$

where the subscripts j = 1 and 2 denote the fiber and transverse directions, respectively, the subscripts f and m respectively represent fiber and matrix resin. V_{f} is the fiber volume fraction, and $E_{11\mathrm{f}}$ and E_{m} are the Young's modulus of carbon fiber and epoxy resin, respectively. Using the following values [43][72][73]; V_{f} = 0.6, $E_{11\mathrm{f}}$ =230 GPa, ν_{12}= 0.35, ν_{m}= 0.38, the final degree of cure α_{final} = 1.0 and the transverse shrinkage strain ${\varepsilon_2}^{\mathrm{C}} = \lambda_2 . \alpha_{\mathrm{final}} = -2500$ με with assumed average resin

modulus in curing of E_{m}= 0.6 GPa, gives $\lambda_{\mathrm{m}} = -1.36 \times 10^{-2}$ and the longitudinal shrinkage strain ${\varepsilon_1}^{\mathrm{C}} = \lambda_1 . \alpha_{\mathrm{final}} = -7.83$ με. The cure shrinkage strain of a balanced cross-ply laminate is then given by

$$ {\varepsilon_{\mathrm{CP}}}^{\mathrm{C}} = \frac{(Q_{11} + Q_{12}){\varepsilon_1}^{\mathrm{C}} + (Q_{22} + Q_{12}){\varepsilon_2}^{\mathrm{C}}}{Q_{11} + Q_{22} + 2Q_{12}} \tag{60} $$

where Q_{ij} denotes the components of the stiffness matrix of a UD laminate, calculated using the lamination theory as follows: Q_{11} =138.5 GPa, Q_{22} =1.49 GPa and Q_{12}=0.522 GPa. Equation (60) yields ${\varepsilon_{\mathrm{CP}}}^{\mathrm{C}} = -43.3$ με, which reasonably agrees with the experimental result (-30.6 με).

Similarly, the coefficients of thermal expansion (CTEs) of a unidirectional laminate β_j $(j = 1, 2)$ are expressed by[72]

$$ \beta_1 = \frac{\beta_{1\mathrm{f}} E_{11\mathrm{f}} V_{\mathrm{f}} + \beta_{\mathrm{m}} E_{\mathrm{m}} (1 - V_{\mathrm{f}})}{E_{11\mathrm{f}} V_{\mathrm{f}} + E_{\mathrm{m}} (1 - V_{\mathrm{f}})} \tag{61} $$

$$ \beta_2 = (\beta_{2\mathrm{f}} + \nu_{12\mathrm{f}} \beta_{1\mathrm{f}}) V_{\mathrm{f}} + (1 + \nu_{\mathrm{m}}) \beta_{\mathrm{m}} (1 - V_{\mathrm{f}}) - \nu_{12} \beta_1 \tag{62} $$

Substituting the additional material properties $\beta_{1\mathrm{f}} = -0.38 \times 10^{-6}\ \mathrm{K}^{-1}$, $\beta_{2\mathrm{f}} = 10 \times 10^{-6}\ \mathrm{K}^{-1}$, $\nu_{12\mathrm{f}} = 0.27$, $\beta_{\mathrm{m}} = 65 \times 10^{-6}\ \mathrm{K}^{-1}$ and $E_{\mathrm{m}} = 2.35$ GPa [4, 13, 14] offers $\beta_1 = 6.23 \times 10^{-8}\ \mathrm{K}^{-1}$ and $\beta_2 = 41.8 \times 10^{-6}\ \mathrm{K}^{-1}$. It should be noted that the average modulus and CTE of the resin during the cooling stage were adopted as E_{m} and β_{m} since their temperature dependence is considerably large [72]. The thermal shrinkage strain of the cross-ply laminate is then given by

$$ {\varepsilon_{CP}}^{T} = \frac{(Q_{11} + Q_{12})\beta_1 + (Q_{22} + Q_{12})\beta_2}{Q_{11} + Q_{22} + 2Q_{12}} \Delta T \tag{63} $$

Where ΔT denotes the temperature difference from the curing temperature ($= -110$ K). Assuming $E_{\mathrm{m}} = 2.35$ GPa as the average resin modulus in cooling leads to $Q_{11} = 139.6$ GPa, $Q_{22} = 5.76$ GPa and $Q_{12} = 2.02$ GPa. Hence, equation (63) provides ${\varepsilon_{\mathrm{CP}}}^{\mathrm{T}} = -256.1$ με, which is 76 % of the measured value. The total process-induced strain ${\varepsilon_{\mathrm{CP}}}^{\mathrm{C}} + {\varepsilon_{\mathrm{CP}}}^{\mathrm{T}}$ is predicted to be $-299\ (= -43.3 - 256.1)$ με, which is a reasonable value (82% of the measured internal strain), considering that the viscoelastic effect is not taken into account in the analysis.

3.2.2 Process-Induced Strain of quasi-isotropic laminates

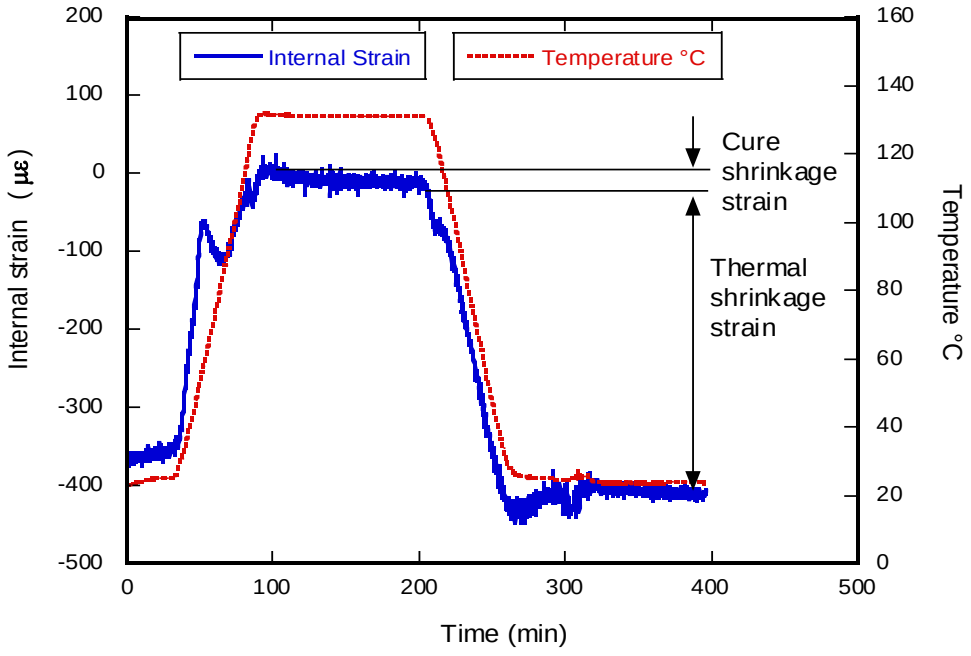

Figure 3- 7 The internal strain and temperature of a CFRP quasi-isotropic laminate during processing.

Figure 3-7 present the typical internal strain and temperature result during the curing process of a quasi-isotropic laminate. The average cure shrinkage and thermal shrinkage strain out of ten specimens were -35 με and -375.2 με, respectively.

Using the same as cross-ply laminate material, they provide the transverse shrinkage strain $\varepsilon_2{}^{\mathrm{C}} = 2500\ \mu\varepsilon$ and longitudinal shrinkage strain $\varepsilon_1{}^{\mathrm{C}} = -7.83\ \mu\varepsilon$. The cure shrinkage strain of a quasi-isotropic laminate is calculated by

$$\varepsilon_{\mathrm{QI}}{}^{\mathrm{C}} = \frac{(Q_{11} + Q_{12})\varepsilon_1{}^{\mathrm{C}} + (Q_{22} + Q_{12})\varepsilon_2{}^{\mathrm{C}}}{Q_{11} + Q_{22} + 2Q_{12}} \tag{64}$$

where Q_{ij} represent the stiffness matrix of a UD laminate, calculated using the lamination theory as follows:

Q_{11}=138.5 GPa.

Q_{22} =1.49 GPa.

Q_{12}=0.522 GPa.

Equation (64) result $\varepsilon_{\mathrm{CP}}{}^{\mathrm{C}} = -43.3\ \mu\varepsilon$, which is exactly the same as the cure shrinkage of a cross-ply laminate.

Similarly, The thermal shrinkage strain of the quasi-isotropic laminate is expressed by

$$\varepsilon_{QI}{}^{T} = \frac{(Q_{11} + Q_{12})\beta_1 + (Q_{22} + Q_{12})\beta_2}{Q_{11} + Q_{22} + 2Q_{12}} \Delta T \tag{65}$$

Substituting the material properties $\beta_1 = 6.23 \times 10^{-8}\ \mathrm{K}^{-1}$ and $\beta_2 = 41.8 \times 10^{-6}\ \mathrm{K}^{-1}$, $Q_{11} = 139.6\ \mathrm{GPa}, Q_{22} = 5.76\ \mathrm{GPa}$, $Q_{12} = 2.02\ \mathrm{GPa}$, and temperature change $\Delta T = -110$ °K result $\varepsilon_{\mathrm{CP}}{}^{\mathrm{T}} = -256.1\ \mu\varepsilon$, lead to a total prediction of $-299\ \mu\varepsilon$. This result is slightly underestimated since the total measured strain $-410.2\ \mu\varepsilon$ (prediction value is 73% of residual strain measured), which is lower than in the case of cross-ply laminate. The difference may attribute to the difference in sensor orientation.

3.2.2 Drilling-Induced Strain

In the drilling process, the internal strain is influenced not only by thermal strain associated with temperature rise but also by mechanical stress due to cutting and trust force of drill bit during drilling. In addition to the above effect, the stress relief by material removal machining and damage-induced strain could also be considered.

Figures 3-8 and 3-9 exhibit the internal strain and the temperature change during drilling of cross-ply and quasi-isotropic laminate. Various drilling conditions are given in Tables 3-3 and 3-5. The internal strain at the beginning of drilling (t = 0 min) under each condition is adjusted to the average process-induced strain (= -366.6 με and -410.2 με for CP and QI respectively) for easy comparison. In both graphs at t = 0 min (arrow A), the drill bit contacts the top surface of the workpiece, and the strain increase with a steep slope in the forward feeding process because of both mechanical force and temperature rise. The maximum strain is observed in the vicinity of full penetration (arrow B), which is defined as the time when the tip of the drill bit is located at 2.8 mm below the bottom surface, this moment where the cutting edge was the closest distance from the FBG sensor. After that, the strain decreases between the peak and the moment of the detachment of the drill bit (arrow C). This decrease is relatively small compared to the increase in the forward process since the temperature is still high, as shown in Figures 3-8 (b) and 3-9 (b). Even after the detachment, the strain continues to decrease with temperature fall and strain recovery due to the viscoelastic effect (arrow D). The above condition indicates the similarity between cross-ply and quasi-isotropic laminate associated with the internal strain during drilling. The final strain and the strain change before and after drilling a cross-ply laminate and quasi-

isotropic laminate are also summarized in Tables 3-3 and 3-5. The average drilling temperature reveals a sufficient difference as pointed in Figures 3-8 (b) and 3-9 (b). The average temperature of cross-ply during drilling exhibits larger than quasi-isotropic laminate; this is attributed to machining conditions. In cross-ply drilling, all machining conditions applied spindle speed 3600 rpm, which is equivalent to cutting speed 73.5 m/min, while in a quasi-isotropic laminate 1600 rpm or equivalent to cutting speed 32.7 m/min. As well known, the drilling temperature increase with cutting speed. However, the cutting speed does not significantly affect the thrust force, which is the largest factor in developing delamination during drilling.

Table 3-3 Drilling conditions in Figure 3-8. The spindle speed is 3600 min^{-1} under all the conditions for cross-ply laminate.

Condition	**Drill bit/ feed rate (mm/s)**	**Peak Strain (με)**	**Final strain (με)**	**Strain change (με)**
1	HSS /1	1316	134.2	500.8
2	HSS / 0.5	842.4	0.0	366.6
3	DC / 1	332.0	-215.2	151.4
4	DC / 0.5	217.9	-318.1	48.5
5	HSS / 0.3	485.0	−421.6	−55.0

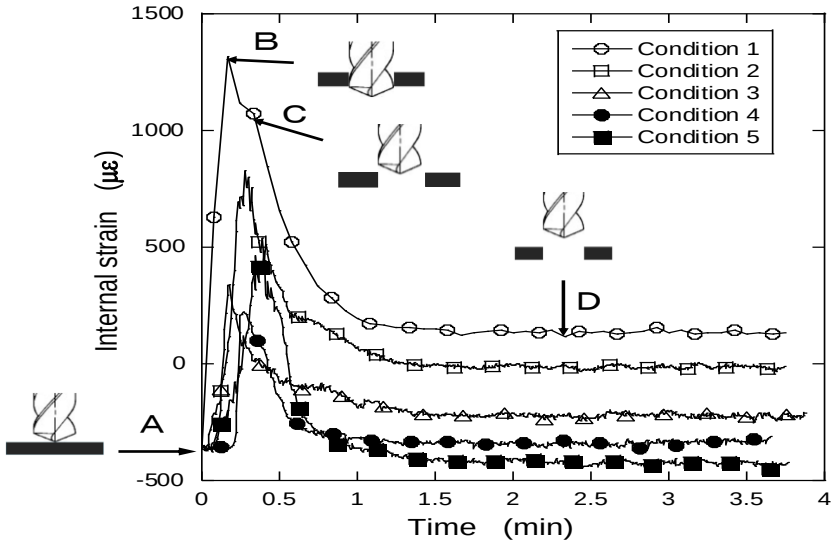

(a)

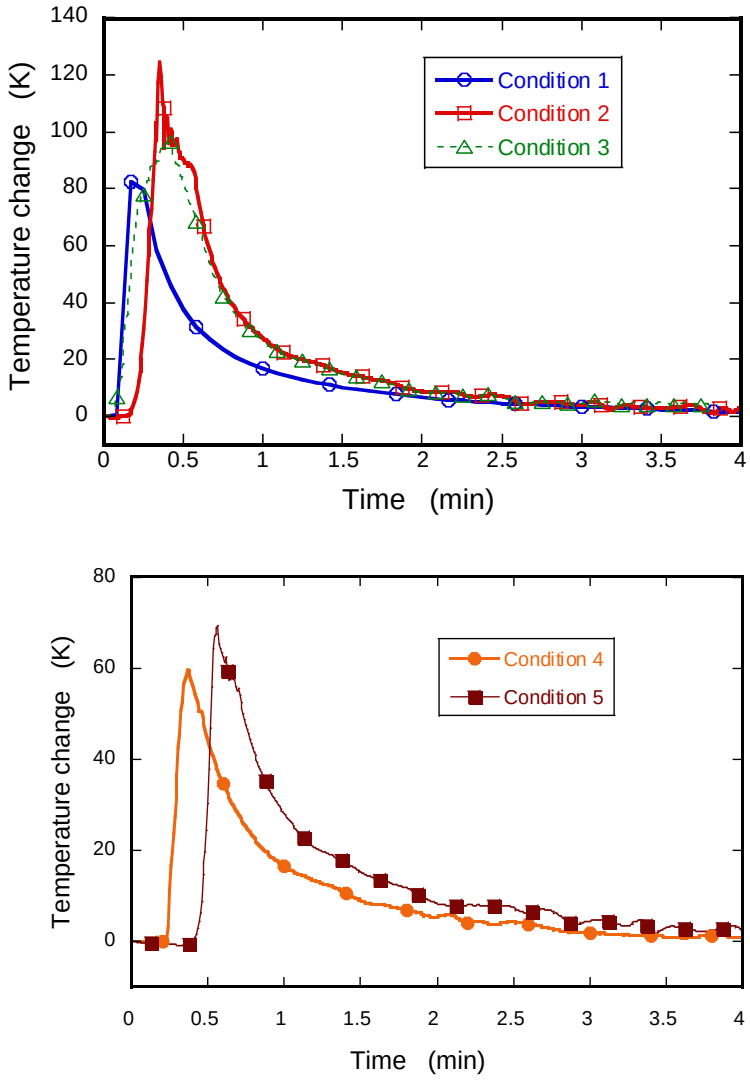

(b)

Figure 3- 8 (a) Internal strain and (b) temperature change during drilling of a cross-ply laminate.

Table 3-4 Distance X and relative position x of the FBG sensor and delamination factor F_d under all the drilling conditions for cross-ply laminate.

Condition	***X* (mm)**	***x* (mm)**	$\boldsymbol{F_d}$
1	3.77	-0.95	1.453
2	4.04	-0.66	1.447
3	4.58	-0.07	1.430
4	4.75	0.14	1.417
5	5.38	0.9	1.377

Table 3-5 Wearing conditions in Figure 3-8. The spindle speed is 1600 min^{-1} under all the conditions for quasi-isotropic laminate.

Condition wear condition	Drill bit/ feed rate (mm/s)	Peak Strain (με)	Final strain (με)	Strain change (με)
1	HSS / 0.5	1152.2	-251.9	158.3
2	HSS / 0.5	1128.3	-325.0	85.2
3	HSS / 0.5	943.2	-331.8	78.4
4	HSS / 0.5	478.8	-395.9	14.3
5	HSS / 0.5	463.9	-411.6	-1.4

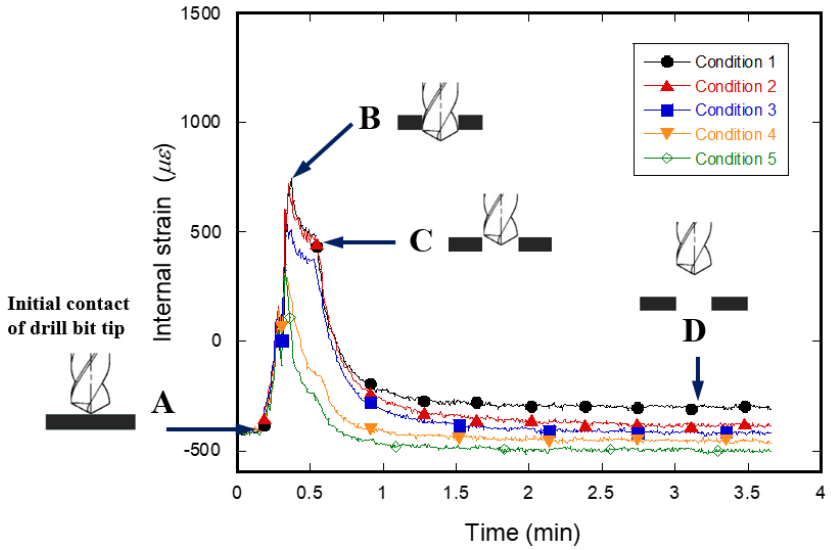

(a)

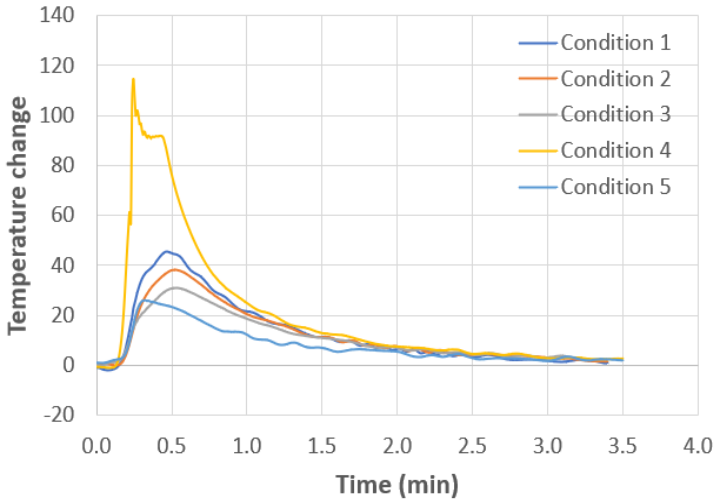

(b)

Figure 3- 9 (a) Internal strain and (b) temperature change during drilling of a quasi-isotropic laminate.

Table 3-6 Distance X and relative position x of the FBG sensor and delamination factor F_d under all the drilling conditions for quasi-isotropic laminate

Tool wear Condition	X **(mm)**	x **(mm)**	F_d
1	4.03	-0.94	1.528
2	4.42	-0.33	1.462
3	4.62	0.29	1.334
4	4.72	0.40	1.329
5	4.26	0.03	1.303

Tables 3-4 and 3-6 list the distance X and the relative position x of the FBG sensor (see Figure 3-5) as well as the delamination factor F_d in each drilling condition. It is found from Tables 3-3 to 3-6 that, under most circumstances (condition 1 to 4), the strain change due to drilling (drilling-induced strain) is positive and has a strong correlation with the peak strain, which corresponds to the maximum drilling force and temperature rise. In contrast, the drilling-induced strain becomes negative under Condition 5 with the least damage (F_d) and the farthest from the hole center among the five conditions. This phenomenon has been reported by Guemes [74], and it is concluded that drilling could cause the stress-release in the vicinity of a hole.

The clear evidence showing the moment of damage generation was not observed in the present study. It is well known that the vicinity of the hole exit is apt to be damaged due to push-out of the drill bit [39]. Hence, a sudden strain change could be observed just after the full penetration (Arrow B in Figure 3-8 (a) and 3-9 (a)). It is presumed that the damage-induced strain is much smaller than the strain change with a decrease in drilling force and temperature fall.

Figure 3-10 depicts the internal strain as well as drilling-induced strain against the relative FBG sensor position x for cross-ply laminate. The difference between the

two strains corresponds to the process-induced strain (= 366.6 με). Both strains are approximately fitted by bilinear curves denoted by solid and dotted lines, as shown in Figure 3-10. The numbers 1 to 5 in this figure represent the drilling conditions in Tables 3-3 and 3-4. From this figure, it is found that the internal strain decreases for $-1.0 < x < 0.3$ mm and gradually increases for $0.3 < x < 2.0$ mm. The strain change is negative within the range of $0.17<x<2.0$ mm. The delamination factor F_d for the negative strain change zone is less than 1.41 while F_d for the positive strain change zone is larger than 1.41, as shown in Table 3-4.

The trend result mentioned above is also obtained in case of internal strain change of quasi-isotropic laminate as depicted in Figure 3-11. The difference between the two strains is 410.2, which is corresponds to a process-induced strain of quasi-isotropic laminate. The figure pointed that the internal strain decline for $-1.0 < x < 0.03$ mm and gradually increases for $0.03 < x < 2.0$ mm. The strain change is negative within the range $-0.15 < x < 0.6$ mm. The delamination factor F_d for the negative strain change zone is less than 1.329 while F_d for the positive strain change zone is larger than 1.329, as shown in table 3-6. These results indicate that stress relief occurs in the negative strain change zone, which is relatively far away from the delamination front.

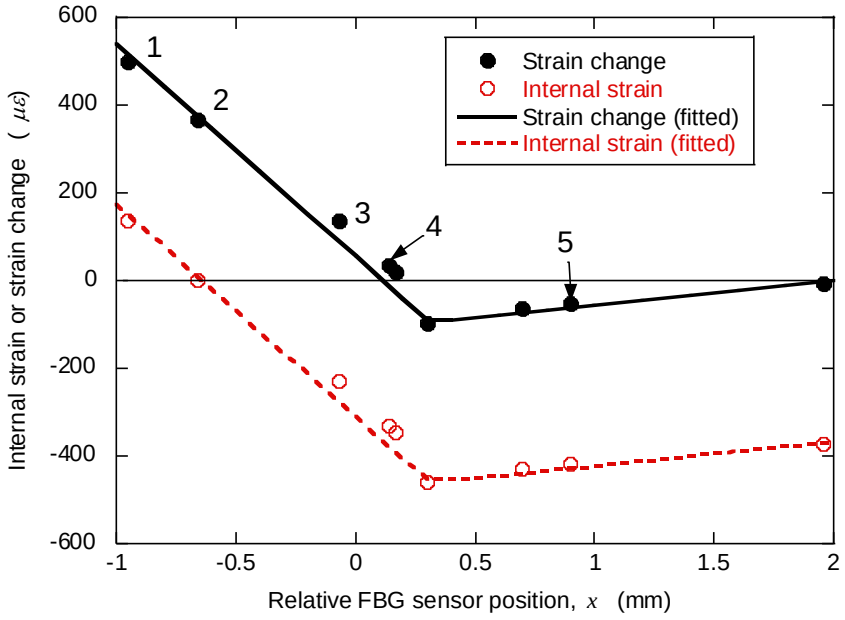

Figure 3- 10 Relation between the relative position of the FBG sensor and internal strain and strain change after cross-ply laminate drilling.

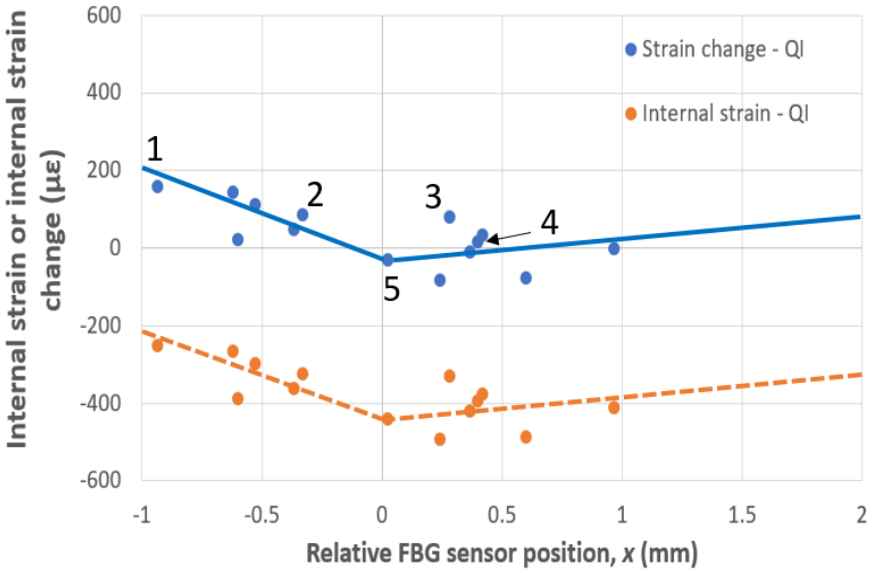

Figure 3- 11 Relation between the relative position of the FBG sensor and internal strain and strain change after quasi-isotropic laminate drilling.

3.2.3 Wavelength spectrum during and after drilling.

The reflected spectrum of the Bragg grating after processing and or machining can remain uniform or distorted. It depends on several factors, including composite morphology and the coating of the FBG. The distortion of the FBG spectrum is mainly caused by residual strain, which is built up during the composite manufacturing process known as a birefringent effect. The spectrum's single sharp peak can be broader or split into two or more peaks due to loading conditions. In general, distortion is caused by the non-axisymmetric load. This deformation of the spectrum will lead to misreading in the strain or temperature measurement.

Figure 3-12 and 3-13 present the FBG spectrum during and after drilling. The reflected spectrum before drilling and after drilling is similar in all conditions. A small peak shifted was observed after drilling, while a significant peak shifted during drilling at the moment of full penetration of drill bit, which is affected by the thermal strain and cutting force as explained in the previous section. Furthermore, a significant distortion of the spectrum has not been found after drilling, except small sidelobes, as shown in figure 3.13. After drilling, the unaltered spectrum indicates that the transverse load or unsymmetric load at sensor gage was not detected. This result leads to the assurance of the axial strain accuracy measurement.

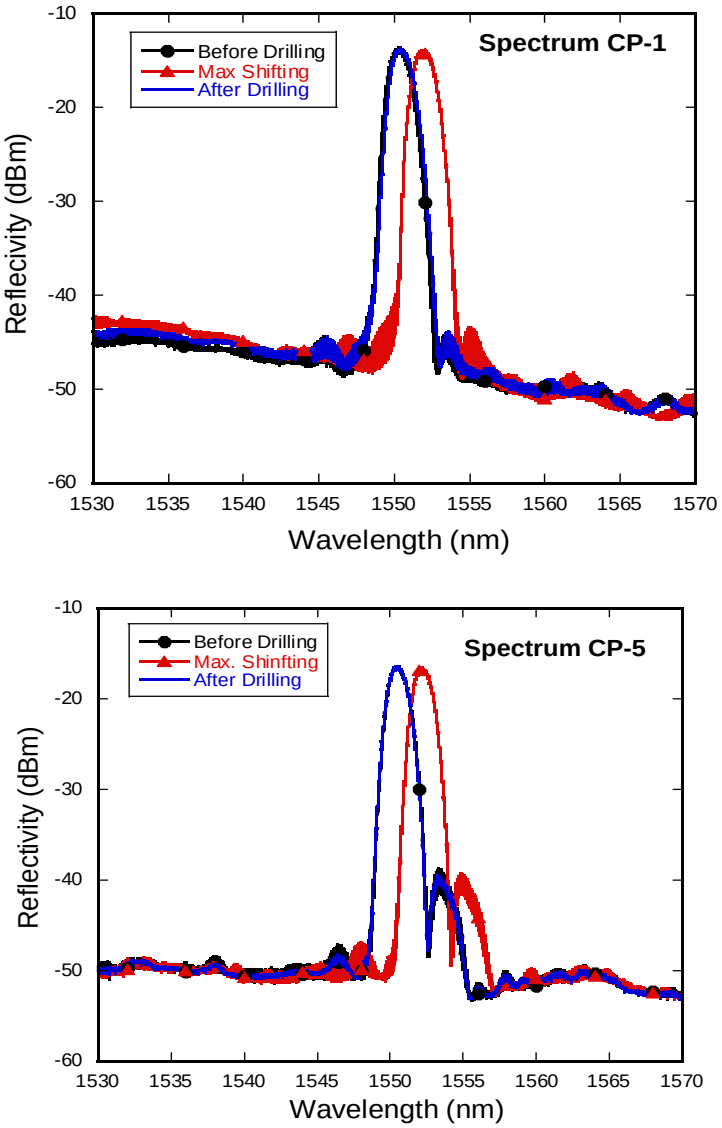

Figure 3- 12 Wavelength spectrum during drilling of cross-ply laminate (a) condition-1 (b) condition-5.

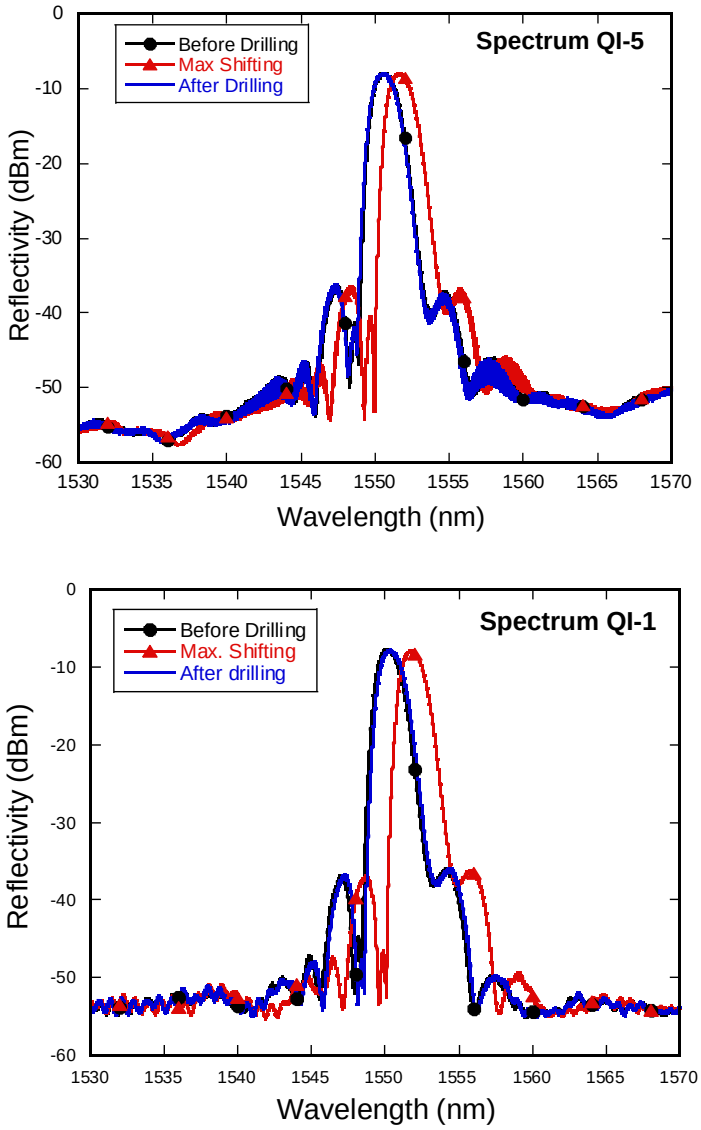

Figure 3- 13 Wavelength spectrum during drilling of quasi-isotropic laminate (a) condition-1 (b) condition-5.

3.2.4 Drilling-Induced Damage

The effect of delamination factor F_d on the internal strain and the strain change after drilling for cross-ply laminate and quasi-isotropic laminate presented in Figures 3-14 and 3-15. The numbers 1 to 5 in these figures also denote the drilling conditions. The solid and dotted curve for two figures are obtained by fitting using linear equation except $1.40 < F_d$ in figure 3-12 using the quadratic equation.

In cross-ply laminate, for $1.0 < F_d \leq 1.40$, the strain change slightly decreases with increasing F_d whereas it rapidly increased for $1.40 < F_d$. As mentioned before, the strain change is positive when F_d is larger than 1.41. This corresponds to the fact that the delamination size is relatively large and that the relative FBG sensor position is close to the delamination front. The same trend is also observed in the internal strain, which becomes positive only when the delamination factor is larger than 1.45. It is impossible to know the sign (tensile or compressive) of the internal strain until the seamless strain monitoring from the processing to drilling is conducted, just like in this study.

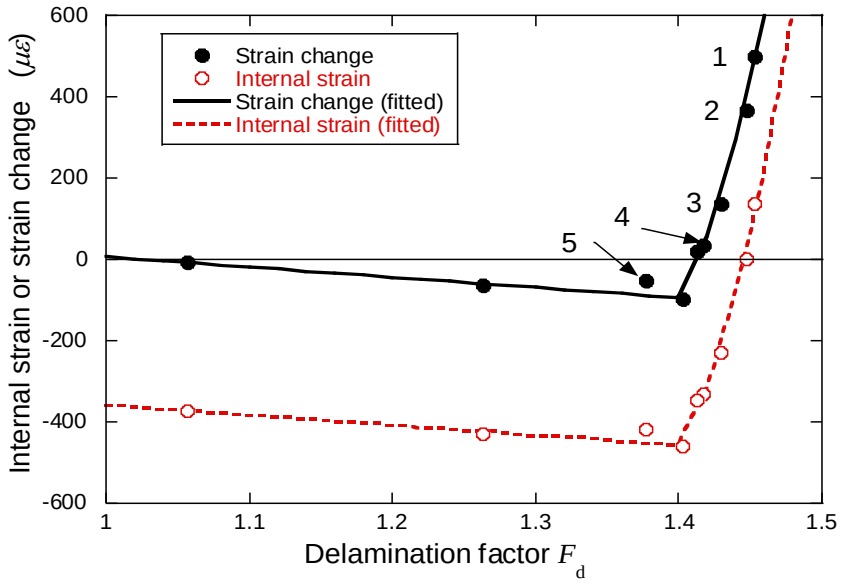

Figure 3- 14 Internal strain and strain change against delamination factor of cross-ply laminate.

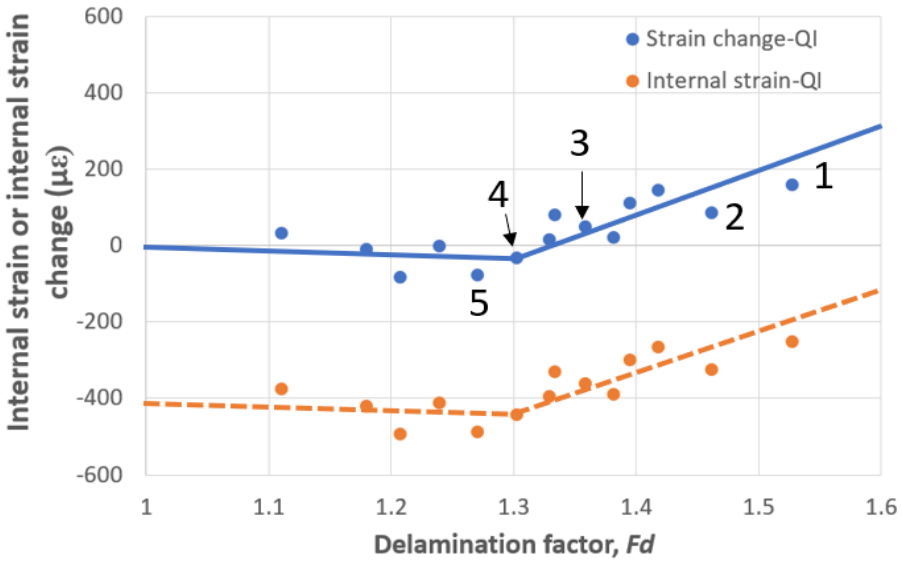

Figure 3- 15 Internal strain and strain change against delamination factor of quasi-isotropic laminate.

In quasi-isotropic laminate, a similar trend is found that the internal strain change decline slightly for $1.0 < F_d \leq 1.32$. Otherwise, the internal strain change increased with the delamination factor (for $1.32 < F_d \leq 1.53$). However, this climb is not as high as at the cross-ply laminate. This difference is presumably the result of the FBG sensor sensitivity associated with the FBG gauge position and orientation. In order to observe this effect, cross-ply and quasi-isotropic laminate were cut at cross-section around the gage sensor after drilling as depicted in Figures 3-16 and 3-17. Figure 3-17 (b) shows considerable damage and the sensor situated in the damaged area (projected from the top). However, the sensor gage apparently intake/undamaged, even the delamination/damage size is large. A different situation was observed in the case of cross-ply laminate, as shown in Figure 3-16. The gage sensor apparently to be damaged, especially the polyamide coating, which is most likely due to delamination/damage as depicted in Figure 3-16 (c).

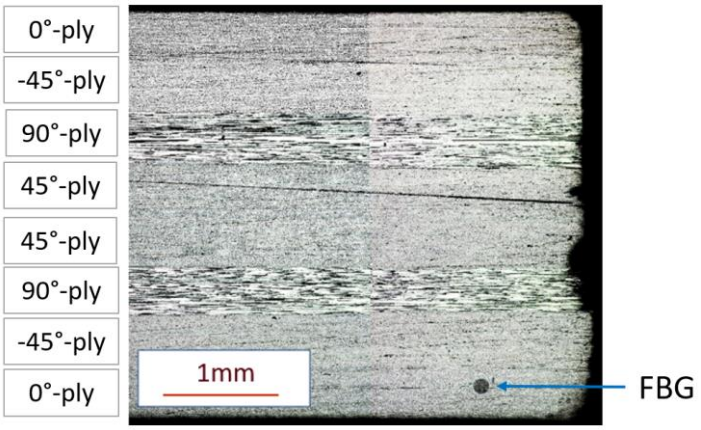

(a)

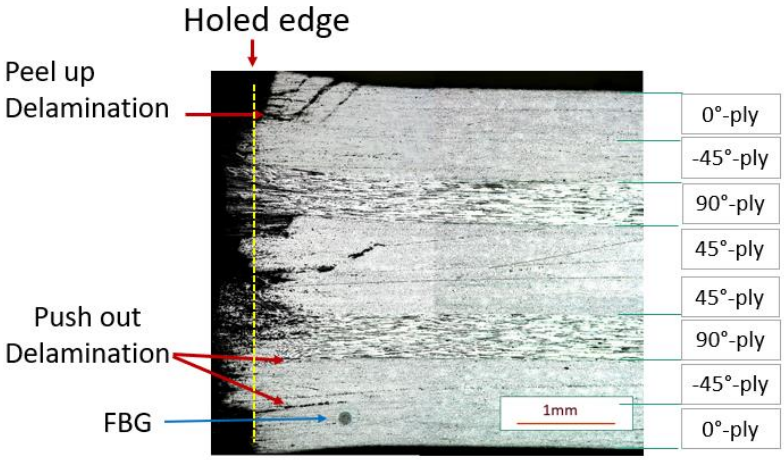

(b)

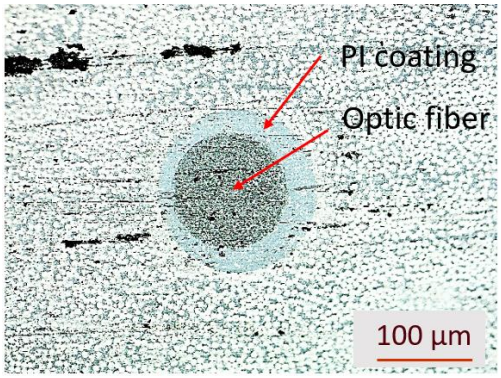

(c)

Figure 3- 16 Quasi-isotropic laminate cross-section of drilled hole wall with (a) small damage and (b) large damage/delamination (c) FBG section gage.

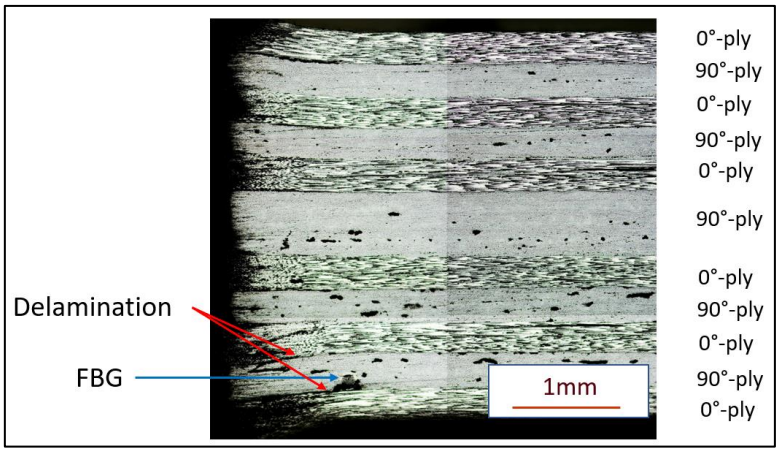

(a)

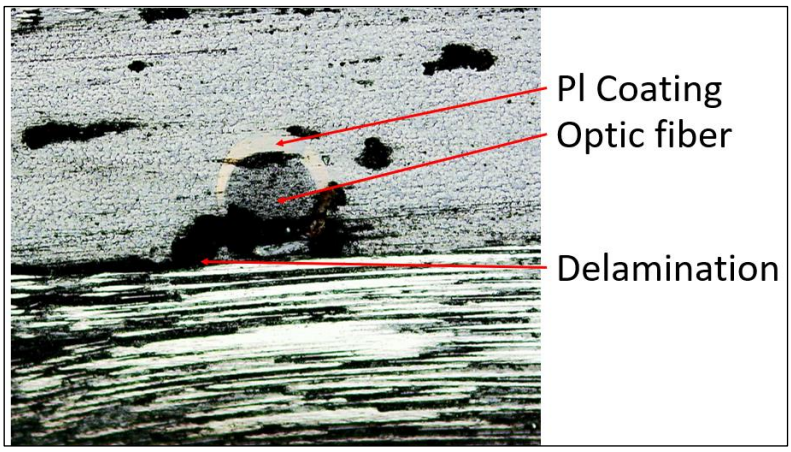

(b)

Figure 3- 17 Cross-ply laminate cross-section of FBG sensor at a quasi-isotropic laminate cross-section of drilled hole wall with (a) small damage and (b) extensive damage/delamination (c) FBG section gage.

3.3. Conclusions

This study demonstrates seamless monitoring of internal strain using embedded FBG sensors from processing to drilling in CFRP cross-ply and quasi-isotropic laminate. The process-induced strain measured with FBG sensors is reasonably in good agreement with predictions using the lamination theory in conjunction with the micromechanical model. The drilling-induced strain was also successfully monitored using the same sensors. The internal strain and drilling-induced strain are correlated with the relative FBG sensor position and the delamination factor.

The drilling process increases the internal strain when the relative position of the sensor x is smaller than some critical value. The critical values in this study for cross-ply and quasi-isotropic laminates are 0.14 mm and -0.33 mm, respectively. When the relative sensor position of the FBG sensor is greater than this value, the internal strain is negative. It means stress relief occurs in the negative strain zone, which is relatively far away from the delamination front.

CHAPTER 4. IN-SITU MONITORING OF CFRP-METAL LAMINATE WITH LOW THERMAL EXPANSION

4.1. Design of the CTE based on lamination theory

4.1.1. Theory.

An FML with a stacking sequence of [SST/45°$_n$/0°$_n$/45°$_n$/90°$_n$]s is considered in this section. The total thickness of the FML, h, is $2t_s + 8nt_p$, where t_p and t_s are the thickness of the pitch-based CFRP prepreg sheet and SST foil, respectively. Because the in-plane stiffness is considered here, the SST foil can be inserted between any of the layers as long as symmetric lamination is maintained. The in-plane CTEs of the FML, $\alpha_x^L(k = x, y, xy)$ are expressed using lamination theory as:

$$\alpha_x^L = (k = x, y, xy)$$
$$\alpha_x^L = \frac{A_{22}n_x^T - A_{12}n_x^T}{A_{11}\,A_{22} - {A_{12}}^2}, \alpha_y^L = \frac{A_{22}n_y^T - A_{12}n_x^T}{A_{11}\,A_{22} - {A_{12}}^2}, \alpha_{xy}^L = 0, \quad (66)$$

Where A_{ij} (i,j = 1, 2, 6) denote the components of the extensional stiffness matrix and n_i^T are the thermal force resultants per temperature change. Let the components of the stiffness matrices of the CFRP and SST be Q_{ij} and $Q_{ij,s}(i, j = 1,2,6)$, respectively, A_{ij} of the FML are given by:

$$A_{11} = A_{22} = 2t_sQ_{11,s} + 2nt_p[\frac{3}{2}(Q_{11} + Q_{22}) + (Q_{12} + 2Q_{66}$$
$$A_{12} = 2t_sQ_{11,s} + 2nt_p[\frac{1}{2}(Q_{11} + Q_{22}) + 3Q_{12} - 2Q_{66} \quad (67)$$
$$A_{66} = 2t_sQ_{66,s} + 2nt_p[\frac{1}{2}(Q_{11} + Q_{22}) - Q_{12} + 2Q_{66}$$

Q_{ij} means that FML is quasi-isotropic with respect to the elastic modulus. n_i^T are expressed as:

$$n_x^T = n_y^T = 2t_s\left(Q_{11,s} + Q_{11,s}\right)\alpha_s + 4nt_p[(Q_{11} + Q_{12})\alpha_1 + (Q_{22} + Q_{12})\alpha_2] \tag{68}$$

In which α_i $(i = 1,2,6)$ and α_s are respectively referred to as the CTE of CFRP and SST. Subtitution of equations (67) and (68) into equation (66) leads to:

$$\alpha_x^L = \alpha_y^L = \frac{\psi r\alpha_s + 2\{\phi\alpha_1 + (1-\phi)\alpha_2}{\psi r + 2} \tag{69}$$

with:

$$\psi = \frac{\left(Q_{11,s} + Q_{12,s}\right)}{2(Q_{11} + Q_{22} + 2Q_{12})}, \phi = \frac{(Q_{11} + Q_{12})}{Q_{11} + Q_{22} + 2Q_{12}}, r = \frac{2t_s}{nt_p} \tag{70}$$

It is shown from equation (69) that the FML is quasi-isotropic also in terms of the CTE, and that CTEs of the FML depend on r, which is the SST to CFRP thickness ratio. The condition for accomplishing a zero-CTE is then given by:

$$\psi rs + 2\{\phi\alpha_1 + (1-\phi)\alpha_2\} = 0 \tag{71}$$

For an FML using pitch-based CFRP, α_s and α_2 are positive while α_1 is negative. The young's modulus *E*, Poisson ratio *v*, shrear modulus G, and density ρ, are written as:

$$E = \frac{{A_{11}}^2 - {A_{12}}^2}{hA_{11}}, \tag{72}$$

$$\upsilon = -\frac{A_{12}}{A_{22}}, G = \frac{A_{66}}{h}, \tag{73}$$

$$\rho = \frac{r\rho_s + 8\rho_c}{r + 8}, \tag{74}$$

Where ρ_s and ρ_c are the density of CFRP and SST, respectively. Subtituting r that satisfies equation (71) into equations (72), (73), and (74) gives the elastic muduli and density of the zero-CTE FML. As the CTE and the Young's modulus of the resin depend on temperature, those of the FML also exhibit temperature dependence.

4.1.2. Calculation of CTE and Young's modulus.

The material properties of the pitch-based UD-CFRP and SST (type 304) are listed in Table 4-1. All the material properties of the UD-CFRP were measured or assumed at room temperature. The CTE and Young's modulus of the FML (n=4) are shown in Figure 4-1[75], where temperature dependence is not considered. Both the CTE and Young's modulus increased with increasing r .The CTE becomes exactly zero for $r = 0.21$ and the corresponding Young's modulus is 163 GPa, which is 83% that of SST and comparable to that of cast iron, as shown in Table 3-1. Figure 4-2 depicts the density ρ and specific modulus E/ρ of the FML plotted against r. For the zero-CTE FML $r = 0.21$, the density is 1.86 g/cm^3, which is less than a quarter that of SST, while the specific modulus is 87.7 GPa cm^3/g, which is 3.5 times as that of SST. Table 4-1 also summarizes the properties of other relevant competing materials such as spheroidal graphite cast iron, granite,

zero-CTE glass ceramics (Neoceram N-0, Nippon Electric Glass), and zero-CTE invar alloy (LEX-ZERO, Nippon Chuzo) together with conventional FMLs. Specific modulus is plotted against CTE in Figure 4-3 for the above materials. Cast iron has the disadvantage of a high CTE and low specific modulus even though its stiffness is comparable to that of the FML. Granite has lower CTE and higher specific modulus compared with cast iron, however, its Young's modulus is only half that of cast iron. Both zero-CTE glass ceramics and invar alloy have a Young's modulus and specific modulus lower than those of the present FML. Consequently, only the present FML meets the requirements of having a near-zero CTE at room temperature, a stiffness as high as that of cast iron, and a density lower than that of glass ceramics.

Table 4- 1 Comparison of CTE, Young's modulus, shear modulus, and specific modulus among relevant competing materials at room temperature. The values in the literature [75] are referred for GLARE, CARAL, and Ti/Gr.

	CTE ($\times 10^{-6}$ /K)	Young's modulus (GPa)	Shear modulus (GPa)	Poisson's ratio	Density (g/cm^3)	Specific modulus (GPa cm^3/g)
UD-CFRP (XN80/Epoxy)	$\alpha_1 = -1.2$[*1] $\alpha_2 = 38$[*1]	$E_1 = 472$[*1] $E_2 = 6.2$[*1]	$G_{12} = 3.5$[*2] $G_{23} = 3.5$[*2] $G_{31} = 3.5$[*2]	$\nu_{12} = 0.35$[*1] $\nu_{23} = 0.45$[*2] $\nu_{31} = 0.0046$	1.70[*1]	-
SST (Type 304)	17.3	197	76	0.30	7.93	24.8
QI-CFRP	-0.5	162	61.0	0.33	1.70	95.3
FML (QI-CFRP/SST)	0±0.12[*2]	163	61.4	0.33	1.86	87.7
GLARE[*3]	15	55	18.2	0.33	2.61	21.3
CARALL[*3]	11	58	17.1	0.32	2.51	23.4
Ti/Gr[*3]	5	89	37.3	0.32	3.56	25.1
Spheroidal graphite cast iron (FCD400[*3])	10	170	66	0.28	7.1	22.5
Granite[*3]	5.3	93	37	0.27	2.9	32.1
Glass ceramics (Neoceram N-0)	-0.1[*4]	94	39	0.2	2.5	37.6
Invar alloy (Lex Zero)	0±0.2[*5]	133	51.6	0.29	8.1	16.4

[*1]Measured in this study, [*2]Assumed values, [*3]Typical values, [*4]Average between 30 and 380 °C, [*5]Average between 20 and 25°C

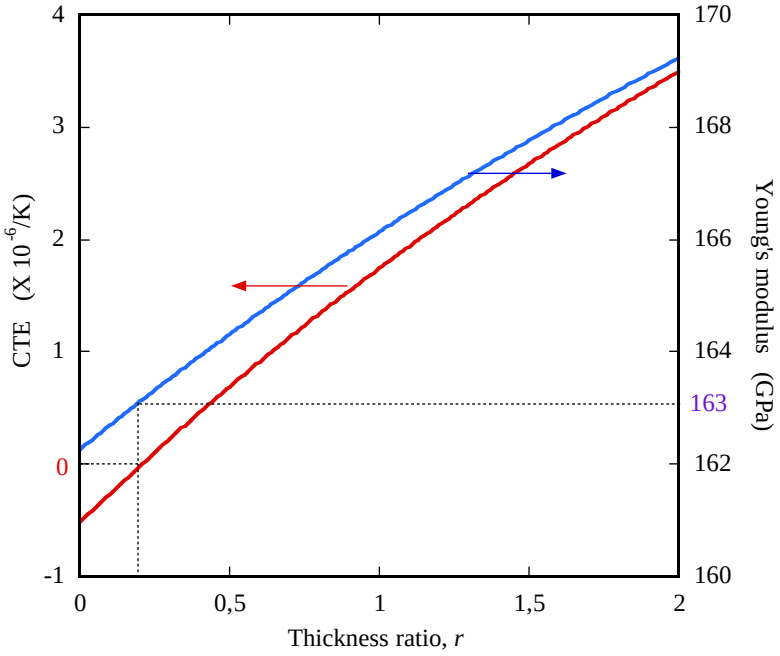

Figure 4- 1 CTE and Young's modulus of the FML.

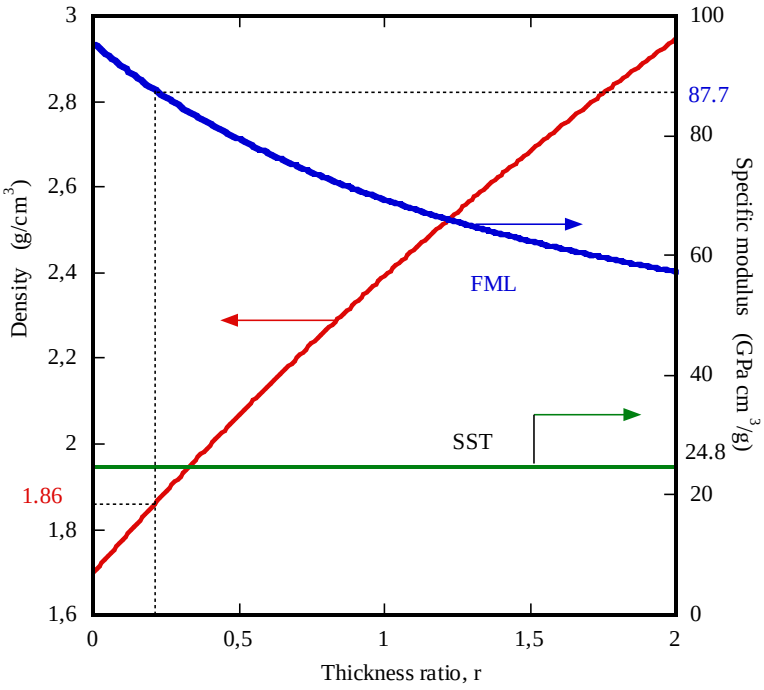

Figure 4- 2 Density and specific modulus of the FML

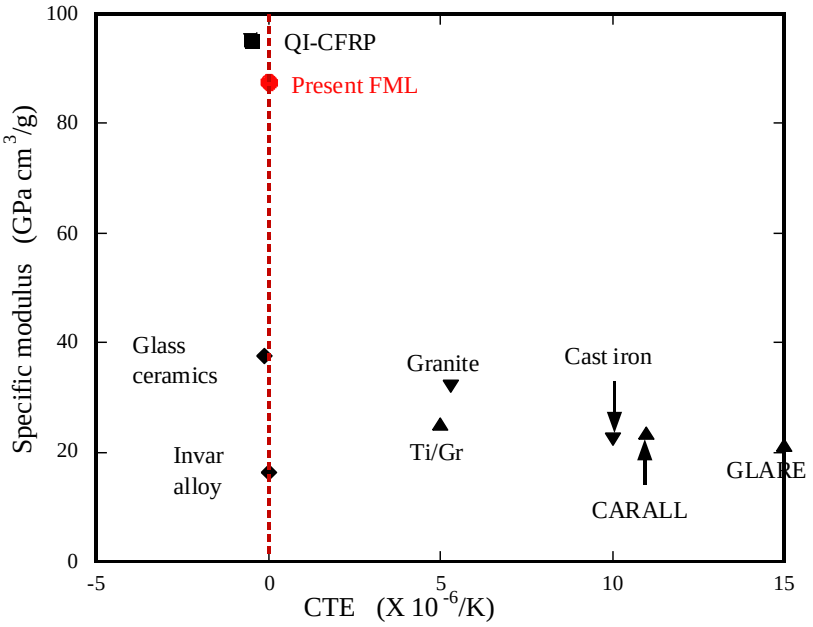

Figure 4- 3 Specific modulus vs. CTE of competing materials in Table 3-1.

4.2. Experimental Procedure

4.2.1. CTE measurement using FBG sensors

First, the CTEs of the pitch-based UD-CFRP and QI-CFRP (XN80/Epoxy, Nippon Graphite Fiber) were measured. The average ply thickness after the cure was 185 μm while the prepreg was 200 μm thick before densification. Figure 4-4 displays the temperature and pressure conditions during the fabrication process and a heating/cooling cycle. A vacuum-bagged UD-CFRP laminate $[0°_{32}]$ and a QI-CFRP laminate $[45°_4/0°_4/-45°_4/90°_4]_S$ were fabricated in an autoclave at a pressure of 0.3 MPa and a temperature of 130 °C for 3 h. After fabrication, the laminates in the autoclave without any pressure were heated up to 160 °C (heating stage) and then cooled down to 20 °C (cooling stage) at a rate of 2 °C/min each. Using $r = 0.21$ in addition to t_p=185 μm and n = 4, the thickness of the SST foil $t_s = nrt_p/2$ was determined as 78 μm. In this study, an 80-μm-thick commercially

available SST foil was employed to produce near-zero CTE FMLs. Two kinds of FML were fabricated under the same conditions presented in Figure 4-4 (a); one was a 100 mm square plate with a stacking sequence of $[SST/45°_4/0°_4/-45°_4/90°_4]_S$, and another was a 250 mm square plate of $[45°_4/SST/0°_4/-45°_4/90°_4]_S$. The latter plate was manufactured for observation of the interface between the SST foil and CFRP plies. Polyimide-coated FBG sensors with a diameter of 145 μm were embedded in the 100 mm square UD-CFRP, QI-CFRP, and FML plates, as depicted in Figure 4-5. The sensor gauge length was selected to be 10 mm from the perspective of the S/N ratio and accuracy. The sensors were embedded at the midplane of the $0°_4$ and $90°_8$ ply groups in the direction parallel to fiber in order to alleviate the effect of birefringence due to residual thermal stress in the QI-CFRP and FML. Two thermocouples were also embedded close to the FBG sensors to measure the temperature inside the laminate.

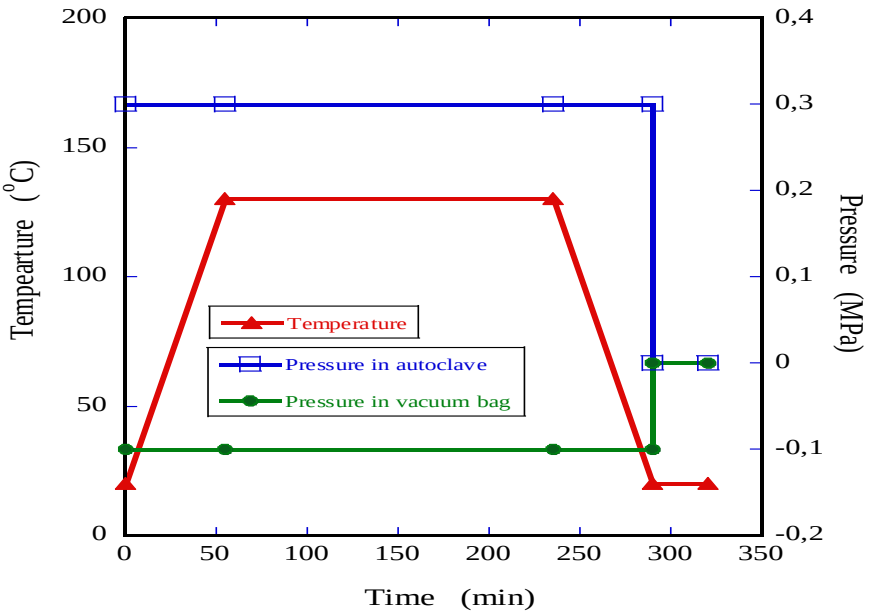

(a)

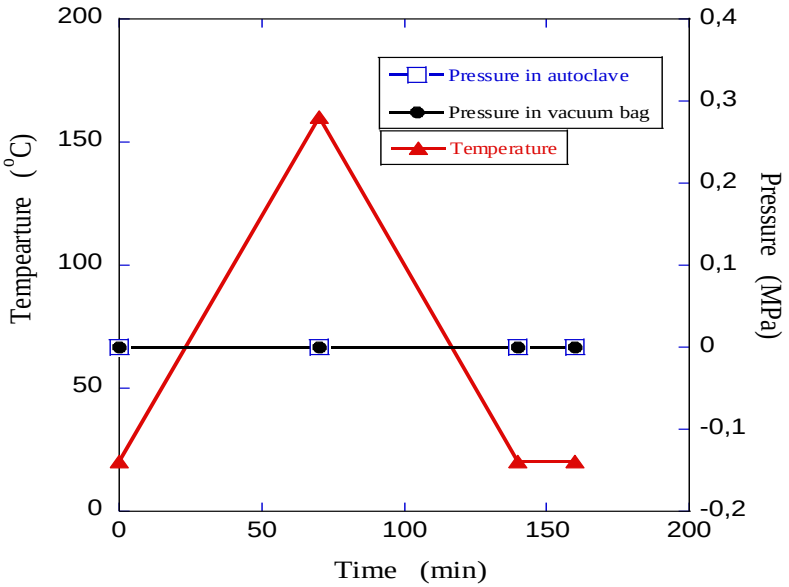

(b)

Figure 4- 4 Temperature and pressure condition in the (a) fabrication process and (b) heating/cooling cycle.

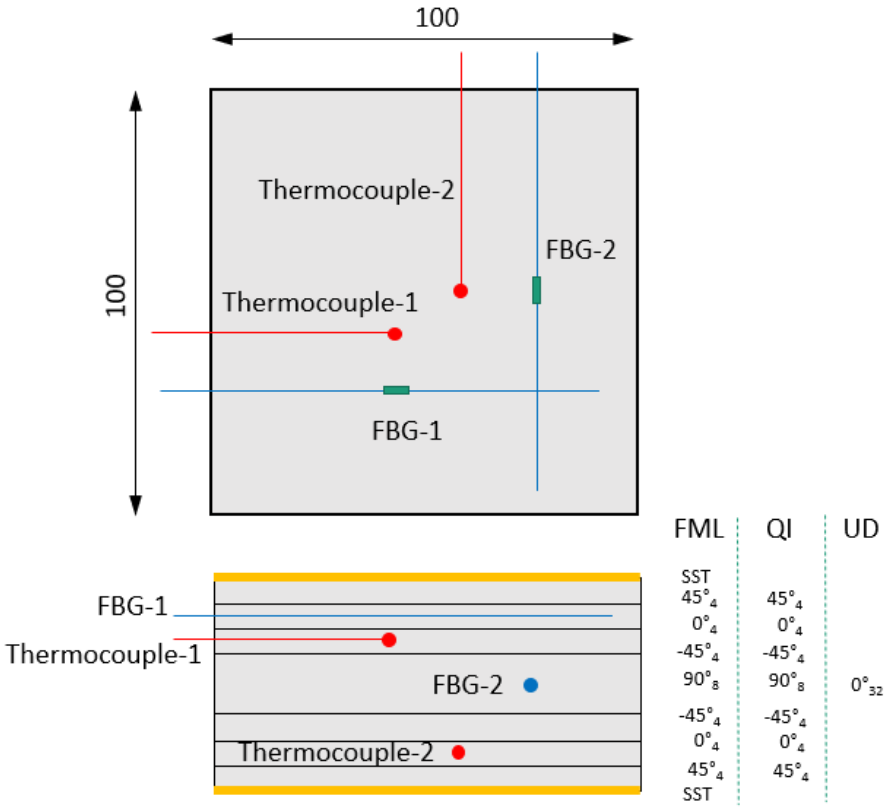

Figure 4- 5 Locations of FBG sensors and thermocouples embedded in the UD-CFRP, QI-CFRP, and FML.

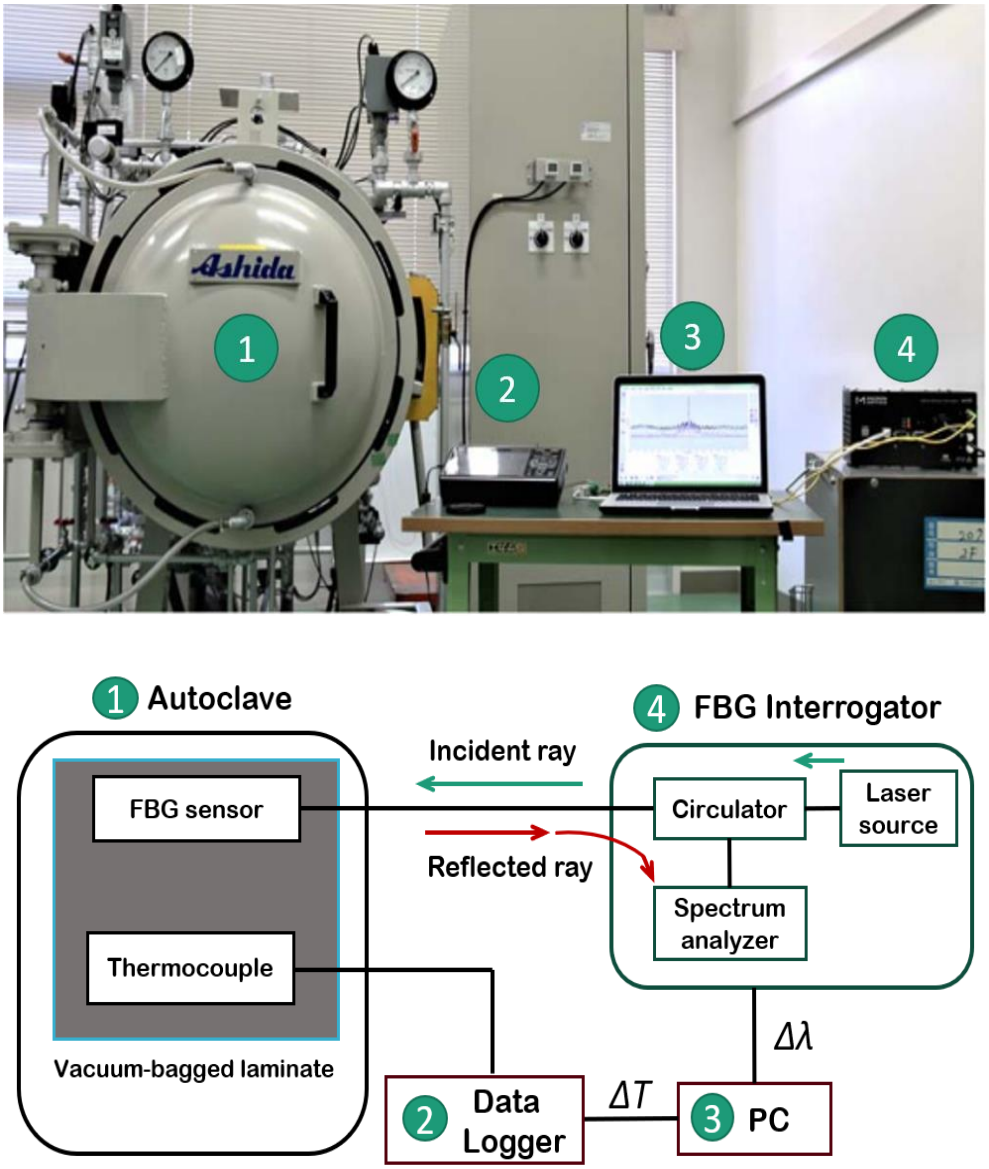

Figure 4- 6 Experimental setup for fabrication and CTE monitoring during a heating/cooling cycle using an autoclave.

Table 4- 2 Values in equation (66)

F_G	C_1 (x 10^{-6}/k)	C_1 (x 10^{-6}/k)	$\lambda_{0\,(nm)}$
0.838	6.156	0.7	1550

Figure 4-6 demonstrates the measurement system for strain and temperature using FBG sensors and thermocouples, respectively. The laser light enters the optic fiber via a circulator. The light reflected from the gauge section returns to the interrogator and the peak wave length was obtained by a spectrum analyzer. The peak wave length from the interrogator and the temperature signals through the data logger were transferred to a personal computer. The thermal strain was calculated using the peak wave length shift $\Delta\lambda$ and temperature change ΔT as:

$$\varepsilon(\mu\varepsilon) = \frac{1\ x\ 10^6}{F_G}\frac{\Delta\lambda_{\boldsymbol{B}}}{\lambda_0} - \left(\frac{C_1}{F_G} - C_2\right)\Delta T \tag{75}$$

where F_G denotes the gauge factor, C_1 is a constant associated with the temperature dependence of effective refractive index, C_2 is a CTE of the FBG sensor, and λ_0 is the Bragg wavelength (see Table 4-2). The Bragg wavelength and temperature at a gel point were defined as the references ($\Delta\lambda = 0$ and $\Delta T = 0$).

Figure 4-7 shows the fabricated FML (250 mm square) and micrographs of the cross-section showing an embedded FBG sensor and interfaces between the SST foil and CFRP plies. It was observed that no voids or delamination were generated around the FBG sensor and at the interfaces, which indicates intact embedment of FBG sensors and bonding at the interfaces.

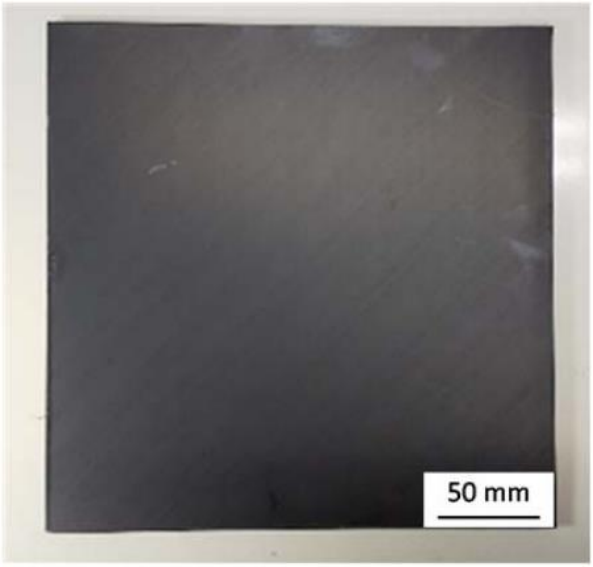

(a)

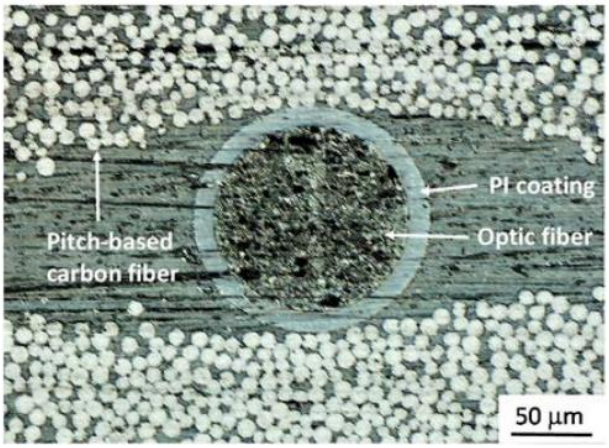

(b)

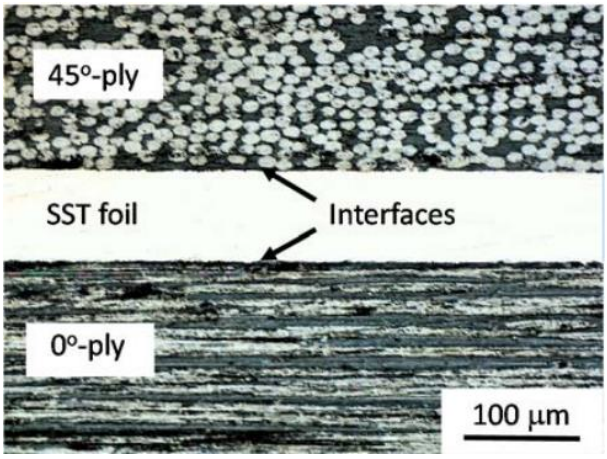

(c)

Figure 4- 7 Photograph showing (a) appearance of the FML (250 mm square), (b) embedding of the FBG sensor, and (c) the interface between the SST foil and CFRP plies.

4.3. Finite element analysis

In this chapter, finite element analysis (FEA) was conducted using commercial software (Marc 2019, MSC) to verify the reasonability of the CTE and Young's modulus calculated based on lamination theory. Figure 4-8 illustrates the dimensions and boundary conditions for analysis of the thermal expansion and Young's modulus. A full-scale model with the size of 100 mm x 100 mm x 6.08 mm (Figure 4-8 (a)) was subdivided into 480,000 8-node brick elements with a total number of nodes of 650,446. The black arrows denote the directions of displacement at the fixed points or surface, while the yellow arrows stand for the direction of applied stress. The model was fixed at the three points shown in Figure 4-8 (b) to obtain the thermal strain between 20 and 130 °C. The CTE was defined as the slope of a thermal strain-temperature diagram. On the other hand, the Young's modulus was calculated from the displacement when the stress of 1 MPa is applied to the right surface, keeping the left surface fixed (Figure 4-8 (c)).

The FEA of the CTE was performed for the following three cases: (Case I) both CTEs and elastic moduli of CFRP are constant, (Case II) only CTEs are temperature dependent, and (Case III) both CTEs and elastic moduli are temperature dependent. The analysis in Case I was performed using the material properties listed in Table 4-1, assuming transverse isotropy of CFRP, where the properties in the thickness direction are identical to those in the transverse directions. Temperature-dependent CTE and elastic moduli described in the next section were employed in Cases II and III.

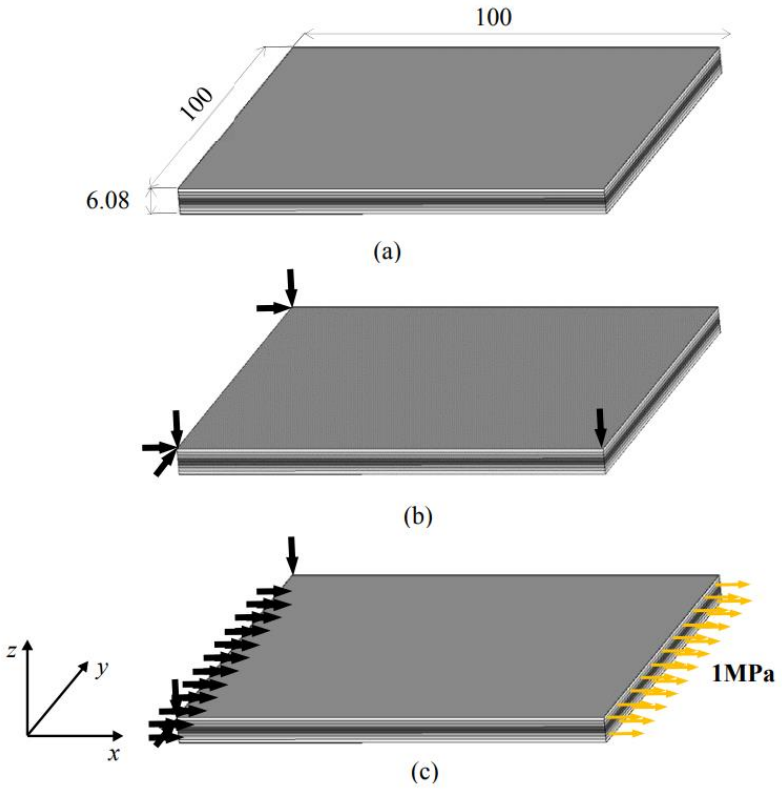

Figure 4- 8 Schematic illustration showing (a) dimensions, (b) boundary conditions for analysis of thermal expansion, and (c) boundary conditions for analysis of Young's modulus in the finite element analysis.

4.4. Result and Discussion

4.4.1. Experiment result

Figure 4-9 shows the measured CTEs of UD-CFRP and QI-CFRP. Small CTEs with absolute values less than $1\text{x}10^{-6}$/°C were measured with high accuracy using the embedded FBG sensors. The CTE of pitch-based carbon fiber is -1.5 /°C at room temperature [76][77]. This indicates that the longitudinal CTE of pitch-based CFRP is -1.3 /°C, which agrees well with the experimental result shown in Figure 4-9. The longitudinal and transverse CTEs of the UD-CFRP exhibit a temperature dependence approximated by the following linear or quadratic functions of temperature:

$$\alpha_1 = (-1.689 + 0.01704T)\text{x}\frac{10^{-6}}{\text{°C}} \tag{76}$$

$$\alpha_2 = (44.96 - 0.5155T + 0.00795T^2)\text{x}\frac{10^{-6}}{℃}$$

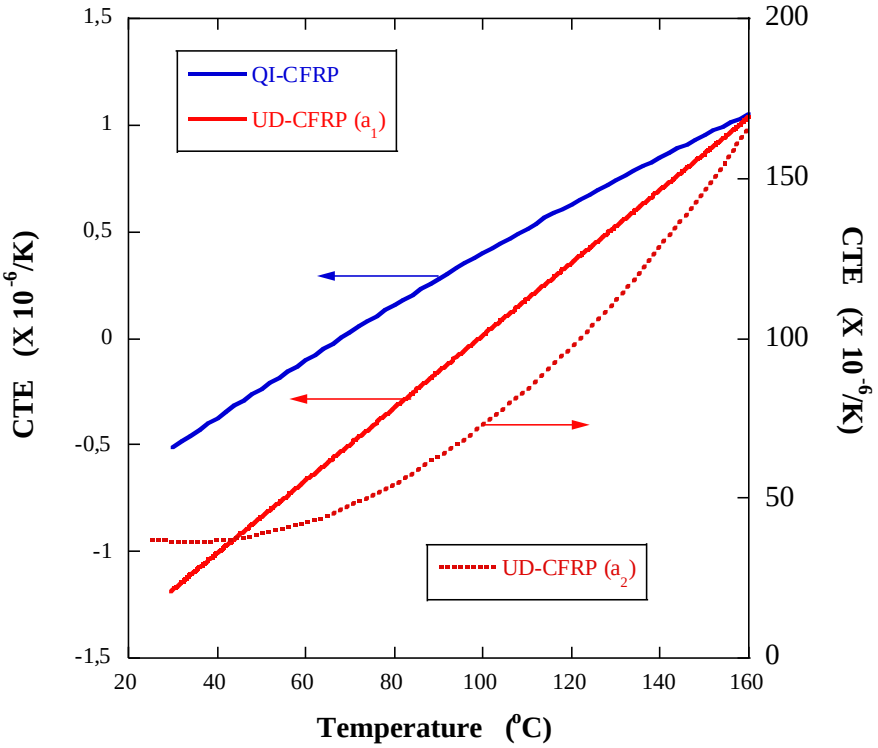

Figure 4- 9 Measured CTE of UD-CFRP and QI-CFRP laminates.

This temperature dependence is ascribed to the fact that the CTE of the epoxy resin increases markedly at temperatures higher than the glass transition temperature T_g, which was estimated to be ~90°C via differential scanning calorimetry. Thus, the CTE in the transverse direction α_2 shows a remarkable increase at temperatures exceeding 90 °C (dotted curve in Figure 4-9). The CTE of QI-CFRP also demonstrated a linear dependence with temperature in the same manner as the CTE in the longitudinal direction of UD-CFRP α_1.

Figure 4-10 compares the CTE of QI-CFRP between the values predicted by lamination theory (equation (69)) and those measured with the FBG sensors. The

predicted CTE is in reasonably good agreement with the measured one, except at elevated temperatures, even though the prediction employs the elastic moduli at 25 °C. Putting $r = 0$ into equation (69) gives the CTEs of QI-CFRP as:

$$\alpha_x^L = \alpha_y^L = \phi\alpha_1 + (1-\phi)\alpha_2 \cong (1-\phi)\alpha_2 \tag{77}$$

The reduction of the transverse modulus E_2 directly leads to an increase in ϕ, and therefore the measured CTE at elevated temperatures becomes smaller than the prediction. The normalized elastic moduli of UD-CFRP estimated from literature [78] using the same 130 °C-cure type UD-CFRP were plotted against temperature in Figure 4-11. These curves can be approximated by cubic functions of temperature and were employed in Case III of the FEA.

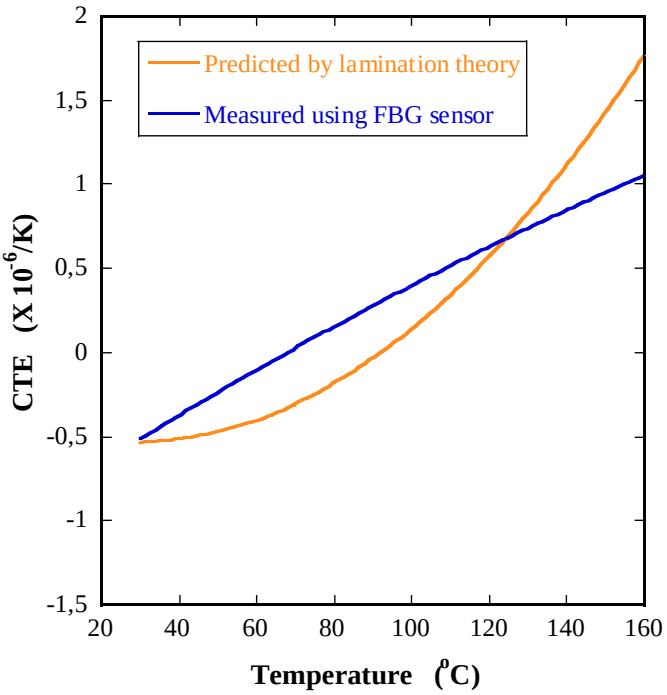

Figure 4- 10 Temperature dependence of the CTE of the QI-CFRP laminate.

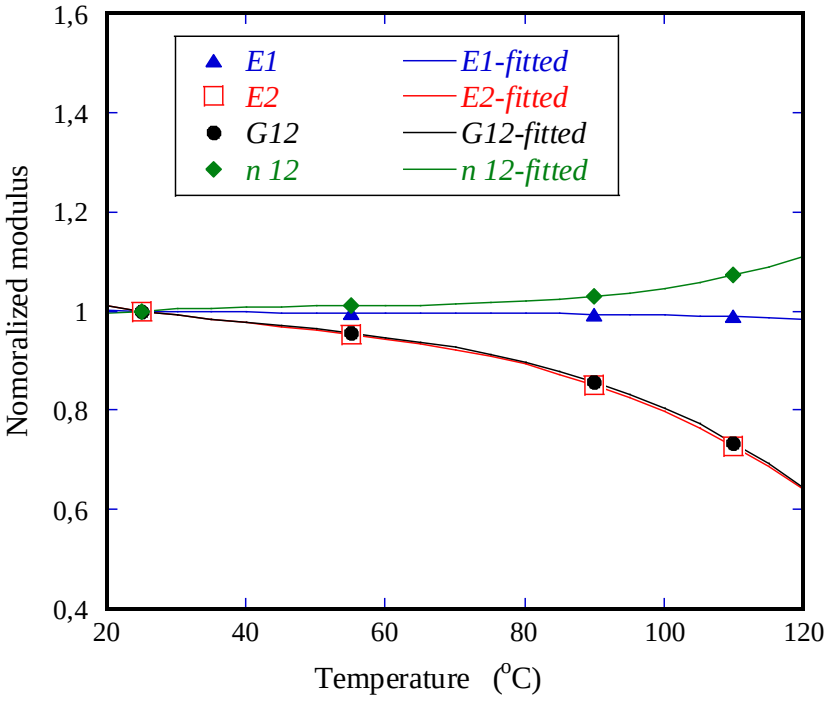

Figure 4- 11 Temperature dependence of normalized elastic moduli of UD-CFRP [23].

Figure 4-12 indicates thermal strain-temperature diagrams obtained during a heat cycle. It should be noted that this thermal strain includes the process-induced strain due to cure and thermal shrinkage. A slight hysteresis was observed during the heat cycle. Because these curves can be fitted by quartic functions of temperature, the CTEs were calculated as differentials of these functions. The obtained CTEs for the two FBG sensors are presented in Figure 4-13. Because the preliminary test confirmed that the CTE-temperature curves in the second heat cycle mostly coincided with the curve at the cooling stage in the first heat cycle, attention was paid to the CTE during the cooling stage here. While evident temperature dependence appeared, which was also observed for QI-CFRP (Figure 4-9), the CTE was limited between −0.3 and 1.0^{-6}/°C in the temperature range of 20–120 °C. In particular, CTEs at room temperature (25 °C) for the two sensors were approximately zero (−0.12 and 0.12×10^{-6} / °C).

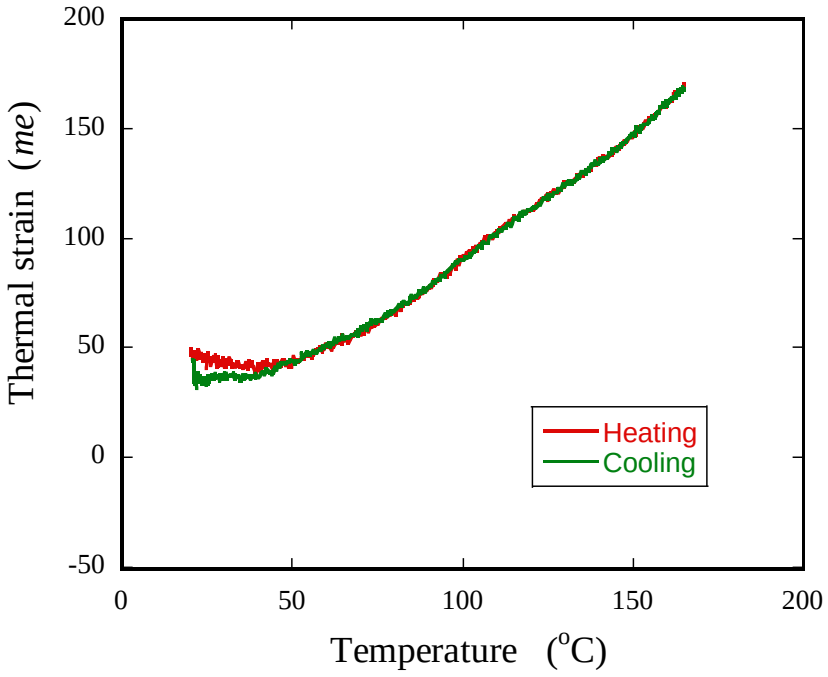

(a) FBG-1 (0°-ply)

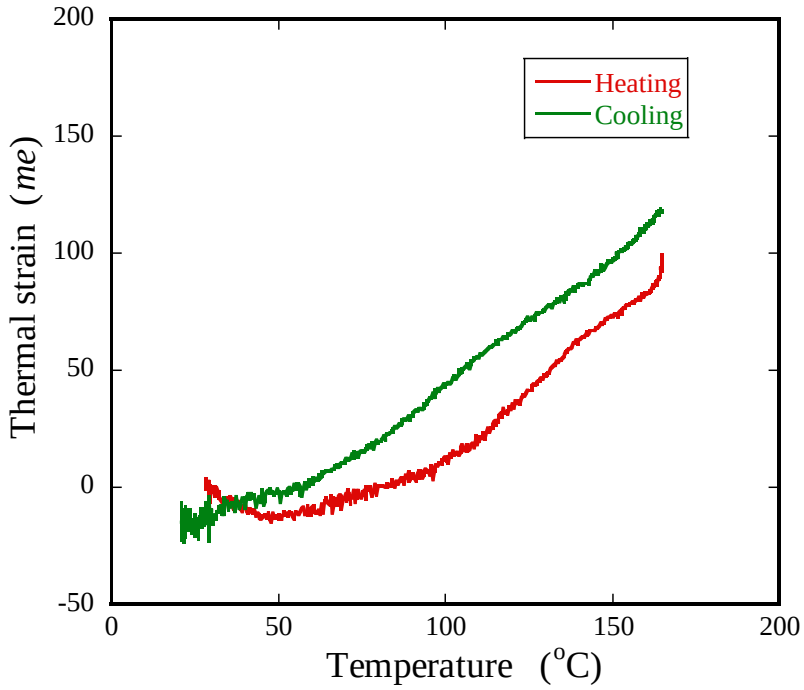

(b) FBG-2 (90°-ply)

Figure 4- 12 Thermal strain-temperature diagrams for the two FBG sensors embedded in the FML.

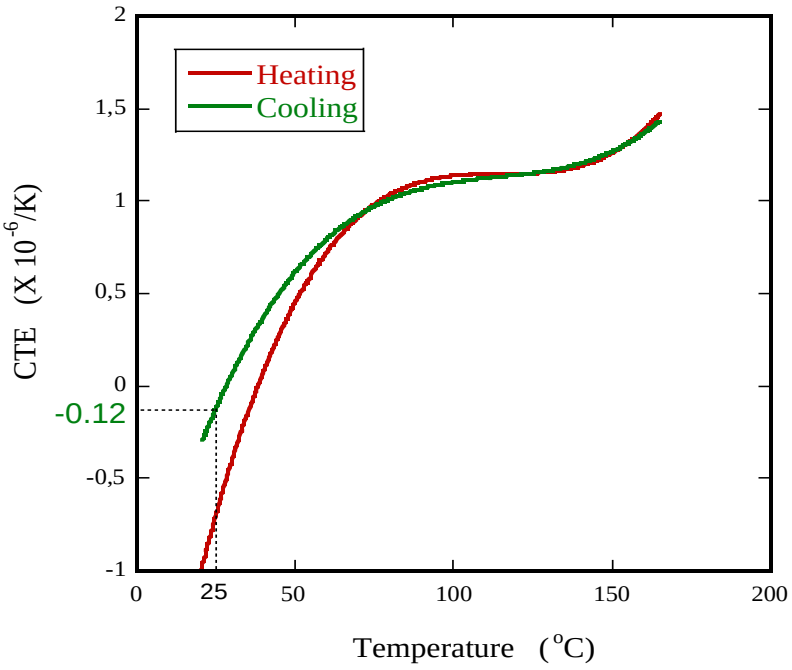

(a) FBG-1 (0°-ply)

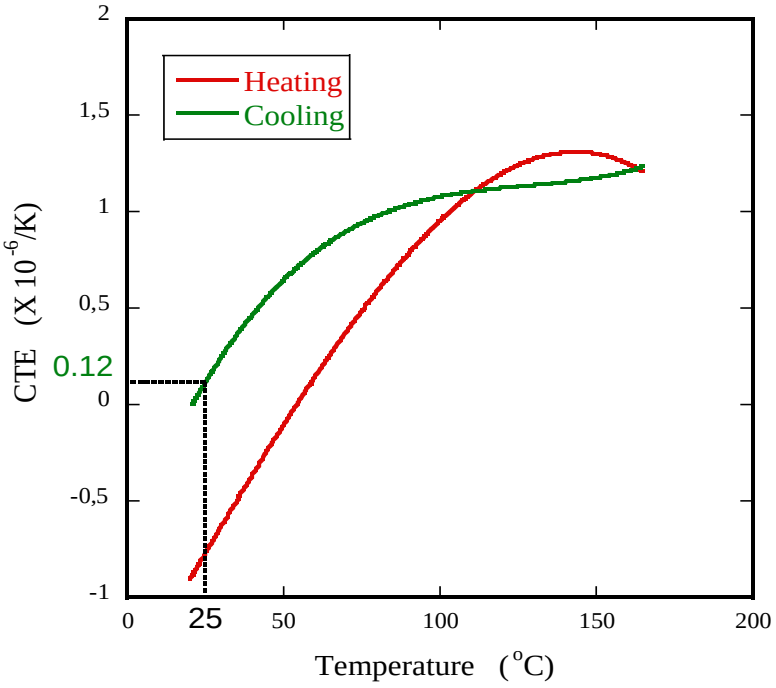

Figure 4- 13 CTE-temperature diagrams for the two FBG sensors embedded in the FML.

4.4.2. FEA result

Figure 4-14 depicts calculated thermal strain distributions ε_x and ε_y on the top surface (SST) of the FML. The uniform temperature change from 20°C to 130°C is given to this model assuming that both CTEs and elastic moduli are temperature dependent (Case III). It is proved that the CTE is quasi-isotropic because the distribution of ε_x except near the edges is almost equal to that of ε_y. Figure 4-15 presents the thermal strain-temperature curves for Cases I, II, and III. The slopes of these curves, CTEs, are nearly zero in the vicinity of room temperature.

The results of FEA at room temperature are summarized in Table 4-3 together with the experiment results. It is demonstrated that the FML has a near-zero CTE at room temperature, with the CTEs at 25°C estimated to be 0.03, −0.04, and −0.12 x 10^{-6}/°C for Cases I, II, and III, respectively. The Young's modulus was determined to be 161.8 GPa, which is very close to the value predicted using lamination theory.

Finally, the temperature dependence of the CTE is compared in Figure 4-16 based on the experimentally obtained results and the numerical predictions by FEA. In Case I, the CTE of the FML is kept constant because the CTE of CFRP is constant. The CTEs in Cases II and III increased with increasing temperature, and the differences between Cases II and III are minor at low temperatures. The CTE in Case II deviated markedly from the experimental result at temperatures >80 °C, while the CTE in Case III shows better agreement with the experimental result even at high temperatures. Underestimation of the CTE in Case III is presumably because of the temperature dependence of coefficients C_1 and C_2 in equation (75). Nevertheless, it can be said that the prediction using lamination theory and the accuracy of the

experimental results were verified from the above FEA results in the temperature range of 20–120 °C.

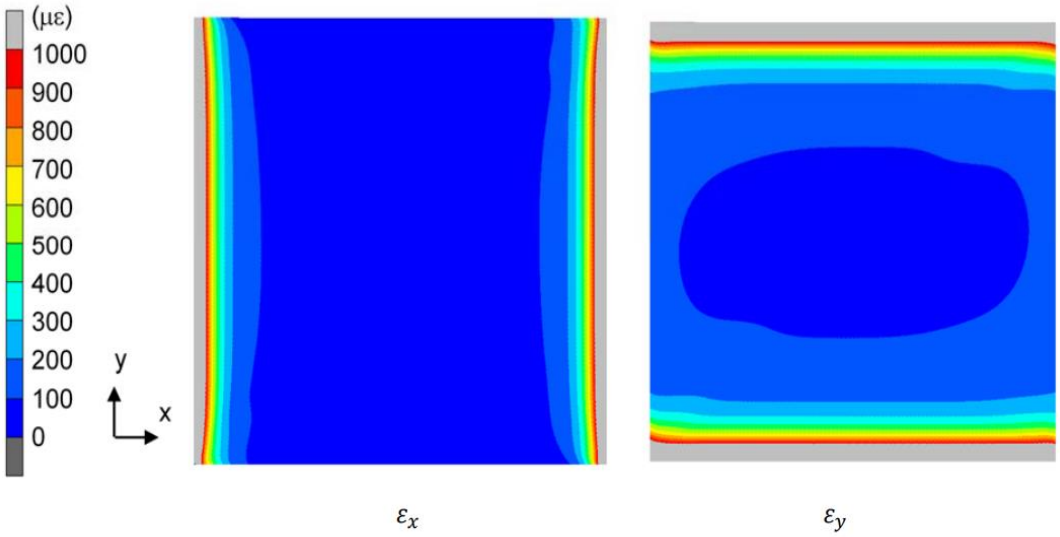

Figure 4- 14 Calculated thermal strain distributions ε_x and ε_y on the top surface (SST) of the FML. The CTEs and elastic moduli are temperature-dependent (Case III).

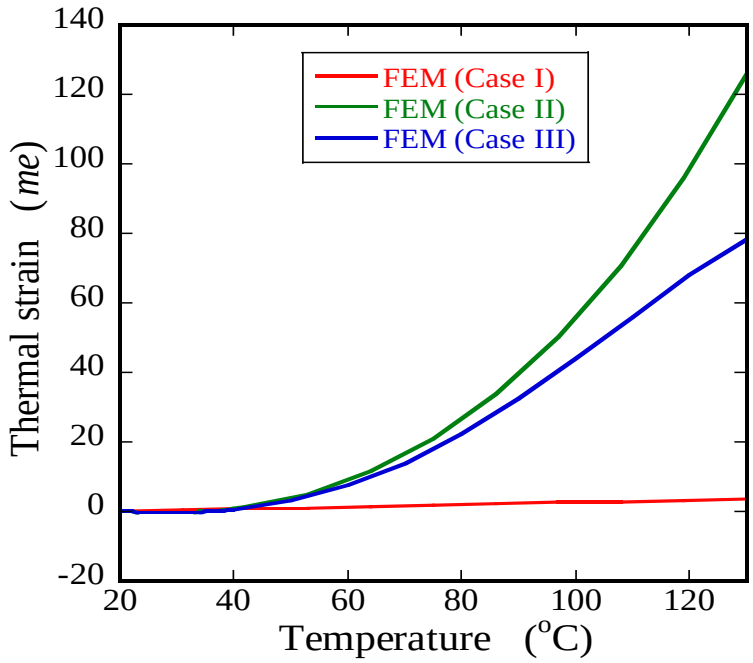

Figure 4- 15 FEA results of the thermal strain vs. temperature of the FML. Cases I, II, and III represent the calculated CTE, assuming that (I) CTEs and elastic modulus are constant, (II) CTEs are temperature dependent, and (III) CTEs and elastic modulus are temperature-dependent.

Table 4- 3 CTE and Young's modulus of the FML at RT

		CTE at 25°C (x 10-6/K)	Young's Modulus (GPa)
Lamination theory *[a]		0.00	163
FEA *[b]	Case I	0.03	161.8
	Case II	-0.04	161.8
	Case III	0.12	161.8
Experiment *[b]	0°-ply 90°-ply	-0.12 0.12	-

[a] SST foil thickness = 155 µm

[b] SST foil thickness = 160 µm

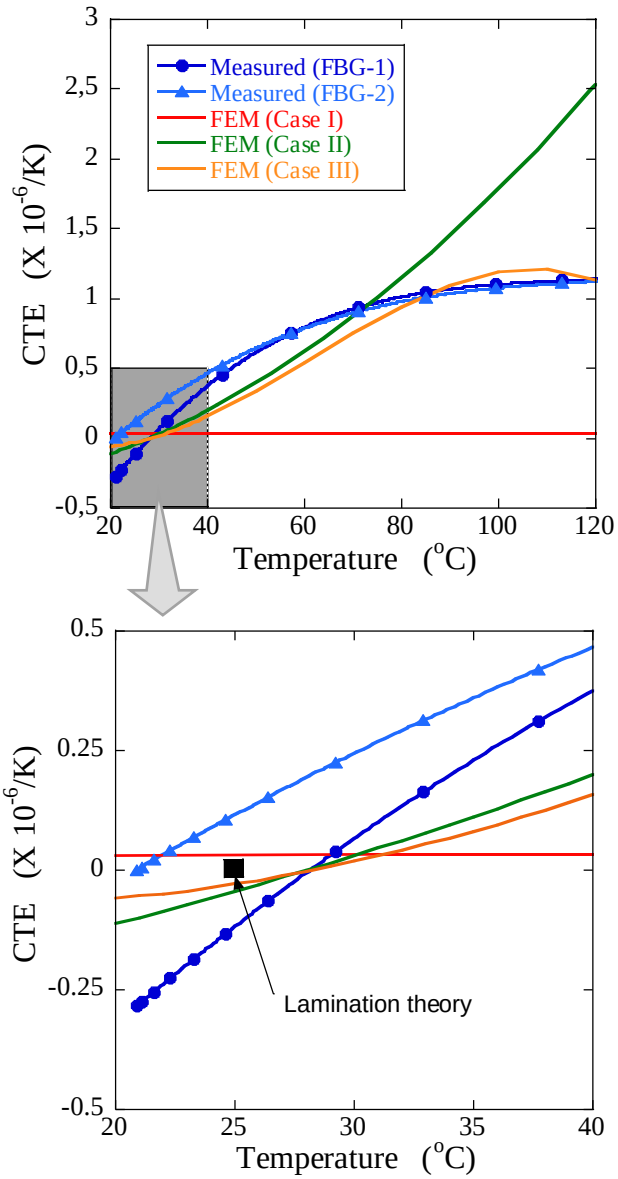

Figure 4- 16 Comparison of the temperature dependence between the measured and calculated CTE of the FML.

4.5. Conclusions

As a structural material with dimensional stability and high stiffness, and FML consisting of pitch-based CFRP and SST foil was established so as to have near-zero CTE around room temperature. The CTE of the FML can be adjusted to be zero by changing the thickness ratio of the SST to CFRP. The CTEs of UD-CFRP, QI-CFRP, and FMLs were measured with high accuracy using embedded FBG sensors. It was experimentally proved that the CTE of the FML was nearly equal to zero at 25 °C and varied from −0.3 to 1.0 $x10^{-6}$/°C in the temperature range of 20–120°C. FEA results proved the near-zero CTE of the FML around room temperature, although they slightly underestimated the CTE, probably because of the temperature dependence of the constants associated with FBG sensors. To more precisely evaluate the CTE of this FML, EFPI sensors with a relatively small diameter will be employed in future work.

The largest advantage of this FML is its high specific modulus compared with other competing materials and conventional FMLs, even though quasi-isotropy and zero-CTE are simultaneously maintained. While the addition of an aluminum alloy instead of SST could also achieve a quasi-isotropic zero-CTE, the stiffness of such an FML would be lower than that of the original QI-CFRP.

CHAPTER 5. CONCLUSIONS AND FUTURE WORK

5.1. General Conclusions

The internal strain of CFRP and CFRP-metal laminate /FML has been successfully monitored in real-time by using an embedded FBG sensor and thermocouple. The general conclusions throughout all the sections can be summarized as follows:

1. Seamless monitoring of internal strain and strain change during the processing of CFRP and FML has been demonstrated in this study by using a small embedded FBG sensor and thermocouple.
2. The internal strain during and after machining was successfully measured by using the same sensors. It is found that the internal strain and drilling-induced strain correlate not only the damage or delamination size but also the relative FBG sensor position.
3. The CTE of the FML can be modified and adjusted to be zero at room temperature by adjusting the thickness ratio of the SST to CFRP.
4. Development of this kind of FML affords a higher specific modulus comparing with other competing materials and conventional FML while maintaining the zero CTE and quasi-isotropic simultaneously.

5.2. Future Work

Several recommendations are suggested to further work as follows:

- An EFPI sensor with a relatively small sensor for a more precise evaluation of the CTE of FML will be considered.
- We will conduct a FE analysis for the thermal strain of QI and cross-ply laminate.
- Various sensor positions and orientations to achieve better damage detection sensitivity will be made.
- The electrical resistance method to investigate the holed damage and electrical resistance change will be applied.

REFERENCES

[1] M. A. Nowak, *An Introduction to polymer-matrix composites*, First Edit. 2015.

[2] P. K. Mallick, *Fiber-Reinforced Composites: Materials, Manufacturing and Design*. 2007.

[3] R. B. Heslehurst, *Defects and Damage in Composite Materials and Structures*. CRC Press, 2014.

[4] Autar K. Kaw, *Mechanics of Composite Materials*, Second Edi., vol. 29, no. Taylor & Francis, 2006.

[5] F. K. Michio Inagaki, "CHAPTER 7 - Carbon Composites," in *Materials Science and Engineering of Carbon: Fundamentals*, 2000, pp. 177–211.

[6] D. D. L. Chung, *Carbon Fiber Composites*. 1994.

[7] K. K. Chawla, *Composite Materials, Science and Engineering*, Third Edit. Springer, 2012.

[8] Michael F. Ashby, *Materials selection in mechanical design*, Third Edit. Elsevier, 2005.

[9] P. Irving and C. Soutis, *Polymer Composites in the Aerospace Industry*. 2015.

[10] C. Soutis, "Carbon fiber reinforced plastics in aircraft construction," *Mater. Sci. Eng. A*, vol. 412, no. 1–2, pp. 171–176, 2005.

[11] R. Brooks, S. M. Shanmuga Ramanan, and S. Arun, *Composites in Automotive Applications: Design*, no. February 2016. Elsevier Ltd., 2017.

[12] T. Ishikawa, K. Amaoka, Y. Masubuchi, and T. Yamamoto, "Overview of automotive structural composites technology developments in Japan," *Compos. Sci. Technol.*, vol. 155, pp. 221–246, 2018.

[13] A. Jacob, "Carbon fibre and cars – 2013 in review," *Reinf. Plast.*, vol. 58, no. 1, pp. 18–19, 2014.

[14] P. J. Schubel, R. J. Crossley, E. K. G. Boateng, and J. R. Hutchinson, "Review of structural health and cure monitoring techniques for large wind turbine blades," *Renew. Energy*, vol. 51, pp. 113–123, 2013.

[15] M. N. Tamin, *Advanced Structured Materials*, vol. 5. 2010.

[16] H. Möhring, "Composites in Production Machines," *Procedia CIRP*, vol. 66, pp. 2–9, 2017.

[17] M. Ramakrishnan, G. Rajan, Y. Semenova, and G. Farrell, “Overview of fiber optic sensor technologies for strain/temperature sensing applications in composite materials,” *Sensors (Switzerland)*, vol. 16, no. 1, pp. 1–27, 2016.

[18] L. Kroll, P. Blau, M. Wabner, J. Eulitz, and M. Kla, “CIRP Journal of Manufacturing Science and Technology Lightweight components for energy-efficient machine tools,” vol. 4, pp. 148–160, 2011.

[19] D. Liu, Y. Tang, and W. L. Cong, “A review of mechanical drilling for composite laminates,” *Compos. Struct.*, vol. 94, no. 4, pp. 1265–1279, 2012.

[20] M. R. Wisnom, M. Gigliotti, N. Ersoy, M. Campbell, and K. D. Potter, “Mechanisms generating residual stresses and distortion during manufacture of polymer-matrix composite structures,” *Compos. Part A Appl. Sci. Manuf.*, vol. 37, no. 4, pp. 522–529, 2006.

[21] O. Sicot, X. L. Gong, A. Cherouat, and J. Lu, “Influence of residual stresses on the mechanical behavior of composite laminate materials,” *Adv. Compos. Mater.*, vol. 14, no. 4, pp. 319–342, 2005.

[22] A. Johnston, R. Vaziri, and A. Poursartip, “A plane strain model for process-induced deformation of laminated composite structures,” *J. Compos. Mater.*, vol. 35, no. 16, pp. 1435–1469, 2001.

[23] J. M. Svanberg and J. A. Holmberg, “An experimental investigation on mechanisms for manufacturing induced shape distortions in homogeneous and balanced laminates,” *Compos. - Part A Appl. Sci. Manuf.*, vol. 32, pp. 827–838, 2001.

[24] V. Antonucci *et al.*, “Process-Induced Residual Stresses in Polymer-Based Composites,” *Polym. News*, vol. 30, pp. 238–247, 2005.

[25] K. S. Kim, “Residual Stress Development during Processing of Graphite / Epoxy Composites,” *Compos. Sci. Technol.*, vol. 36, pp. 121–132, 1989.

[26] S. R. White and H. T. Hahn, “Cure Cycle Optomization for the Reduction of Precessing-Induced Residual Straesses in Composite Materials,” *J. Compos. Mater.*, vol. 27, pp. 1352–1378, 1993.

[27] M. Zarrelli, I. K. Partridge, and A. D. Amore, “Warpage induced in bi-material specimens : Coefficient of thermal expansion , chemical shrinkage and viscoelastic modulus evolution during cure,” *Compos. Part A Appl. Sci. Manuf.*,

vol. 37, pp. 565–570, 2006.

[28] G. Fernlund *et al.*, “Experimental and numerical study of the effect of cure cycle, tool surface, geometry, and lay-up on the dimensional fidelity of autoclave-processed composite parts,” *Compos. - Part A Appl. Sci. Manuf.*, vol. 33, no. 3, pp. 341–351, 2002.

[29] W. Chen, “Some experimental investigations in the drilling of carbon fiber-reinforced plastics (CFRP) composite laminates,” *Int. J. Mach. Tools Manufactruing*, vol. 37, no. 8, pp. 1097–1108, 1997.

[30] R. Piquet, B. Ferret, F. Lachaud, and P. Swider, “Experimental analysis of drilling damage in thin carbon/epoxy plate using special drills,” *Compos. Part A Appl. Sci. Manuf.*, vol. 31, no. 10, pp. 1107–1115, 2000.

[31] E. D. Eneyew and M. Ramulu, “Experimental study of surface quality and damage when drilling unidirectional CFRP composites,” *J. Mater. Res. Technol.*, vol. 3, no. 4, pp. 354–362, 2014.

[32] Y. Turki, M. Habak, R. Velasco, Z. Aboura, K. Khellil, and P. Vantomme, “Experimental investigation of drilling damage and stitching effects on the mechanical behavior of carbon/epoxy composites,” *Int. J. Mach. Tools Manuf.*, 2014.

[33] J. Turner, R. J. Scaife, and H. M. ElDessouky, “Advanced Manufacturing: Polymer & Composites Science Effect of machining coolant on integrity of CFRP composites Effect of machining coolant on integrity of CFRP composites,” *Polym. Compos. Sci*, vol. 1, p. 5460, 2015.

[34] L. Durão, J. Tavares, V. de Albuquerque, J. Marques, and O. Andrade, “Drilling Damage in Composite Material,” *Materials (Basel).*, vol. 7, no. 5, 2014.

[35] L. Sorrentino, S. Turchetta, and C. Bellini, “A new method to reduce delaminations during drilling of FRP laminates by feed rate control,” *Compos. Struct.*, vol. 186, pp. 154–164, 2018.

[36] T. sunny, J. Babu, and J. Philip, “Experimental Studies on Effect of Process Parameters on Delamination in Drilling GFRP Composites Using Taguchi Method,” *Procedia Mater. Sci.*, vol. 6, no. Icmpc, pp. 1131–1142, 2014.

[37] L. M. P. Durão, D. J. S. Gonçalves, J. M. R. S. Tavares, V. H. C. De Albuquerque, and A. T. Marques, “Comparative analysis of drills for composite

laminates," *J. Compos. Mater.*, vol. 46, no. 14, pp. 1649–1659, 2012.

[38] C. C. Tsao, "Drilling processes for composites," *Mach. Technol. Compos. Mater.*, pp. 17–64, 2012.

[39] T. MIYAKE, K. MUKAE, and M. FUTAMURA, "Evaluation of machining damage around drilled holes in a CFRP by fiber residual stresses measured using micro-Raman spectroscopy," *Mech. Eng. J.*, vol. 3, no. 6, pp. 16-00301-16–00301, 2016.

[40] R. Zitoune, N. Cadorin, F. Collombet, and M. Šíma, "Temperature and wear analysis in function of the cutting tool coating when drilling of composite structure: In situ measurement by optical fiber," *Wear*, vol. 376–377, pp. 1849–1858, 2017.

[41] T. Okabe and S. Yashiro, "Damage detection in holed composite laminates using an embedded FBG sensor," *Compos. Part A Appl. Sci. Manuf.*, vol. 43, no. 3, pp. 388–397, 2012.

[42] A. Ajovalasit, "Advances in Strain Gauge Measurement on Composite Materials," *Strain*, vol. 47, pp. 313–325, 2011.

[43] S. Minakuchi, S. Niwa, K. Takagaki, and N. Takeda, "Composite cure simulation scheme fully integrating internal strain measurement," *Compos. Part A Appl. Sci. Manuf.*, vol. 84, pp. 53–63, 2016.

[44] M. S. Loukil, J. Varna, and Z. Ayadi, "Damage characterization in glass fiber/epoxy laminates using electronic speckle pattern interferometry," *Exp. Tech.*, vol. 39, no. 2, pp. 38–45, 2015.

[45] M. Kanerva *et al.*, "Direct measurement of residual strains in CFRP-tungsten hybrids using embedded strain gauges," *Mater. Des.*, vol. 127, pp. 352–363, 2017.

[46] L. Ke, C. Li, J. He, S. Dong, C. Chen, and Y. Jiao, "Effects of elevated temperatures on mechanical behavior of epoxy adhesives and CFRP-steel hybrid joints," *Compos. Struct.*, vol. 235, 2020.

[47] R. Prussak, D. Stefaniak, C. Hühne, and M. Sinapius, "Evaluation of residual stress development in FRP-metal hybrids using fiber Bragg grating sensors," *Prod. Eng.*, vol. 12, no. 2, pp. 259–267, 2018.

[48] C. H. D. Ong, K. L. I. Ai, Y. U. X. I. J. Iang, D. W. A. Rola, and D. O. Z. Hang,

"Evaluation of thermal expansion coefficient of carbon fiber reinforced composites using electronic speckle interferometry," *Opt. Express*, vol. 26, no. 1, pp. 531–543, 2018.

[49] S. Yoneyama, P. G. Ifju, and S. E. Rohde, "Identifying through-thickness material properties of carbon-fiber-reinforced plastics using the virtual fields method combined with moiré interferometry," *Adv. Compos. Mater.*, vol. 27, no. 1, pp. 1–17, 2018.

[50] L. F. Wu, J. G. Zhu, and H. M. Xie, "Investigation of Residual Stress in 2D Plane Weave Aramid Fibre Composite Plates Using Moiré Interferometry and Hole-Drilling Technique," *Strain*, vol. 51, pp. 429–443, 2015.

[51] Q. Wang, T. Li, X. Yang, Q. Huang, B. Wang, and M. Ren, "Multiscale numerical and experimental investigation into the evolution of process-induced residual strain/stress in 3D woven composite," *Compos. Part A Appl. Sci. Manuf.*, vol. 135, no. December 2019, p. 105913, 2020.

[52] G. Sun, X. Liu, G. Zheng, Z. Gong, and Q. Li, "On fracture characteristics of adhesive joints with dissimilar materials – An experimental study using digital image correlation (DIC) technique," *Compos. Struct.*, vol. 201, no. Dic, pp. 1056–1075, 2018.

[53] A. Kaur *et al.*, "Strain monitoring of bismaleimide composites using embedded microcavity sensor," *Opt. Eng.*, vol. 55, no. 3, p. 037102, 2016.

[54] S. Tanpichai, W. W. Sampson, and S. J. Eichhorn, "Stress-transfer in microfibrillated cellulose reinforced poly(lactic acid) composites using Raman spectroscopy," *Compos. Part A Appl. Sci. Manuf.*, vol. 43, no. 7, pp. 1145–1152, 2012.

[55] G. Luyckx, E. Voet, N. Lammens, and J. Degrieck, "Strain measurements of composite laminates with embedded fibre bragg gratings: Criticism and opportunities for research," *Sensors*, vol. 11, no. 1, pp. 384–408, 2011.

[56] K. T. Hsiao, "Embedded single carbon fibre to sense the thermomechanical behavior of an epoxy during the cure process," *Compos. Part A Appl. Sci. Manuf.*, vol. 46, no. 1, pp. 117–121, 2013.

[57] S. Minakuchi, "In situ characterization of direction-dependent cure-induced shrinkage in thermoset composite laminates with fiber-optic sensors embedded in

through-thickness and in-plane directions," *J. Compos. Mater.*, vol. 49, no. 9, pp. 1021–1034, 2015.

[58] R. De Oliveira *et al.*, "Experimental investigation of the effect of the mould thermal expansion on the development of internal stresses during carbon fibre composite processing," *Compos. Part A Appl. Sci. Manuf.*, vol. 39, no. 7, pp. 1083–1090, 2008.

[59] S. Takeda, Y. Okabe, and N. Takeda, "Delamination detection in CFRP laminates with embedded small-diameter fiber Bragg grating sensors," *Compos. - Part A Appl. Sci. Manuf.*, vol. 33, no. 7, pp. 971–980, 2002.

[60] M. E. Kazemi, L. Shanmugam, L. Yang, and J. Yang, "A review on the hybrid titanium composite laminates (HTCLs) with focuses on surface treatments, fabrications, and mechanical properties," *Compos. Part A Appl. Sci. Manuf.*, vol. 128, no. October 2019, p. 105679, 2020.

[61] N. G. Gonzalez-Canche, E. A. Flores-Johnson, and J. G. Carrillo, "Mechanical characterization of fiber metal laminate based on aramid fiber reinforced polypropylene," *Compos. Struct.*, vol. 172, pp. 259–266, 2017.

[62] C. Liu *et al.*, "Interlaminar failure behavior of GLARE laminates under short-beam three-point-bending load," *Compos. Part B Eng.*, vol. 97, pp. 361–367, 2016.

[63] M. Sasso, E. Mancini, G. S. Dhaliwal, G. M. Newaz, and D. Amodio, "Investigation of the mechanical behavior of CARALL FML at high strain rate," *Compos. Struct.*, vol. 222, no. April, p. 110922, 2019.

[64] J. Sun, A. Daliri, G. Lu, D. Ruan, and Y. Lv, "Tensile failure of fibre-metal-laminates made of titanium and carbon-fibre/epoxy laminates," *Mater. Des.*, vol. 183, p. 108139, 2019.

[65] Y. Yang, M. A. Silva, and R. J. C. Silva, "Material degradation of cfrp-to-steel joints subjected to salt fog," *Compos. Part B Eng.*, vol. 173, no. April, p. 106884, 2019.

[66] M. Heshmati, R. Haghani, and M. Al-emrani, "Durability of bonded FRP-to-steel joints : Effects of moisture , de-icing salt solution , temperature and FRP type," *Compos. Part B*, vol. 119, pp. 153–167, 2017.

[67] R. Di Sante, "Fibre Optic Sensors for Structural Health Monitoring of Aircraft

Composite Structures: Recent Advances and Applications," *Sensors*, vol. 15, no. 8, pp. 18666–18713, 2015.

[68] C. E. Campanella, A. Cuccovillo, C. Campanella, A. Yurt, and V. M. N. Passaro, "Fibre Bragg Grating based strain sensors: Review of technology and applications," *Sensors (Switzerland)*, vol. 18, no. 9, 2018.

[69] S. Lu, M. Jiang, Q. Sui, Y. Sai, and L. Jia, "Damage identification system of CFRP using fiber bragg grating sensors," *Compos. Struct.*, vol. 125, pp. 400–406, 2015.

[70] "CARBON FIBER T700S," 2018. [Online]. Available: www.toraycma.com.

[71] A. Faraz, D. Biermann, and K. Weinert, "Cutting edge rounding: An innovative tool wear criterion in drilling CFRP composite laminates," *Int. J. Mach. Tools Manuf.*, vol. 49, no. 15, pp. 1185–1196, 2009.

[72] K. Ogi, K. Mizukami, H. Matsutani, and N. Sato, "Monitoring of Cure and Thermal Shrinkage in Interlayer-Toughened Cfrp Laminates," *Proc. 18th Eur. Conf. Compos. Mater.*, no. June, pp. 24–28, 2018.

[73] TORAYCA, "TORAY data Sheet." [Online]. Available: http://www.toraycfa.com/pdfs/T700SDataSheet.pdf.

[74] J. A. Guemes and J. M. Menéndez, "Response of Bragg grating fiber-optic sensors when embedded in composite laminates," *Compos. Sci. Technol.*, vol. 62, no. 7–8, pp. 959–966, 2002.

[75] T. C. Chen, Y. J. Chen, M. H. Hung, and J. P. Hung, "Design analysis of machine tool structure with artificial granite material," *Adv. Mech. Eng.*, vol. 8, no. 7, pp. 1–14, 2016.

[76] Y. TANABE, E. YASUDA, K. YAMAGUCHI, M. INAGAKI, and Y. YAMADA, "Studies on 'Mesophase'-Pitch-Based Carbon Fibers: Part II Mechanical Properties and Thermal Expansion," *Tanso*, vol. 1991, no. 147, pp. 66–73, 1991.

[77] F. G. Emmerich, "Young's modulus, thermal conductivity, electrical resistivity and coefficient of thermal expansion of mesophase pitch-based carbon fibers," *Carbon N. Y.*, vol. 79, no. 1, pp. 274–293, 2014.

[78] K. Ogi, H. Inoue, and Y. Takao, "An electromechanical model for the temperature dependence of resistance and piezoresistance behavior in a CFRP

unidirectional laminate," *Compos. Sci. Technol.*, vol. 68, no. 2, pp. 433–443, 2008.

ACKNOWLEDGMENTS

In the name of Allah, Most Gracious and Most Merciful. I would like to express my sincere thanks and gratitude to my supervisor, Prof Dr. Keiji Ogi, for his guidance, support, advice and encouragement given throughout my doctoral journey at Ehime University.

An appreciation is due to Associate Professor Dr. Mitsuyoshi Tsutsumi, Professor Dr. Koichi Mizukami, and the rest member of Mechanic of Materials Laboratory for their help and support during this research work.

I would also like to thank Government of Indonesia as well as the State Polytechnic of Ujung Pandang for providing financial support. My sincere gratitude is also extended to member of Matsuyama Islamic Cultural Center (MICC), and Persatuan Pelajar Indonesia Jepang (PPIJ) for their encouragement, and companionship throughout my stay in Japan.

I should like to express my deepest appreciation to my family for their endless support and encouragement given over such a long period of time especially my parent who has tried their best in providing me with the best education. A special appreciation to my beloved wife, Rosmiati Nur, for all the care, support, encouragement and understanding throughout these long and hard years and to my four children, Naelah Niswah, Ghaziya Hafiza, and Ibnu Jauzy - all of whom has made life in this foreign country bearable. Finally, to everyone I knew, whose names are too many to be listed, thank you very much for everything.

Baso Nasrullah

Matsuyama, Japan, December 2020.